Automatic Measurement of Human Subcutaneous Fat with Ultrasound

by

Jessie Ying Chi Ng

B.A.Sc., The University of British Columbia, 2002

A THESIS SUBMITTED IN PARTIAL FULFILMENT OF
THE REQUIREMENTS FOR THE DEGREE OF

Master of Applied Science

in

The Faculty of Graduate Studies

(Electrical and Computer Engineering)

The University of British Columbia

September 2006

Abstract

Measuring human subcutaneous fat is useful for assessing health risks due to obesity and for monitoring athletes' health status, body shapes and weight for various sports competitions such as gymnastics and wrestling. Our aim is to investigate the use of ultrasound imaging in automatically measuring human subcutaneous fat thickness.

We proposed to use the spectrum properties extracted from the raw radio frequency (RF) signals of ultrasound for the purpose of fat boundary detection. Our fat detection framework consists of four main steps. The first step is capturing RF data from 11 beam steering angles and at four focal positions. Secondly, two spectrum properties (spectrum variance and integrated backscatter coefficient) are calculated from the local spectrum of RF data using the short time Fourier transform and moment analysis. The values of the spectrum properties are encoded as gray-scale parametric images. Thirdly, spatial compounding is used to reduce speckle noise in the parametric images and improve the visualization of the subcutaneous fat layer. Finally, we apply Rosin's thresholding and Random Sample Consensus boundary detection on the parametric images to extract the fat boundary.

The detection framework was tested on 36 samples obtained at the suprailiac, thigh and triceps of nine human participants *in vivo*. When compared to manual boundary detection on ultrasound images, the best result was obtained from segmenting the spatial compounded spectrum variance values averaged over multiple focuses. A reasonable result could also be obtained by using a single focus. Further, our automatic detection results were compared with the results using skinfold caliper measurements. We found that the correlation is high between our automatic detection and skinfold caliper measurement, and is similar to the previous studies which are not automatic. Our work has shown that the spatial compounded spectrum properties of RF data can be used to segment the subcutaneous fat layer. Based on our results, it is feasible to detect fat at the suprailiac, thigh and triceps sites using the spectrum variance. The values of spectrum variance change more rapidly in the fat tissue than the non-fat tissue.

Contents

Abstract ii

Contents iii

List of Tables vii

List of Figures x

Glossary xvi

Notation xx

Acknowledgements xxii

1 Background and Introduction 1

1.1 Current Techniques of Human Body Fat Measurement 2

1.1.1 Body Density Weighing 2

1.1.1.1 Underwater Weighing 2

1.1.1.2 Air-displacement Plethysmography 3

1.1.2 Bioelectrical Impedance Analysis 3

1.1.3 Skinfold Caliper 4

1.1.4 Imaging Techniques 4

1.1.4.1 Dual Energy X-ray Absorptiometry 5

1.1.4.2 Computed Tomography 5

1.1.4.3 Magnetic Resonance Imaging 5

1.1.4.4 Ultrasound 6

1.2 Motivation 8

1.3 Pulse-Echo Ultrasound Imaging 11
    1.3.1 Apparatus 11
    1.3.2 Interaction of Ultrasound with Soft Tissues 15
    1.3.3 Backscattered Radiofrequency Spectra 17
    1.3.4 Current Development of Ultrasound Segmentation 19
1.4 Properties of Human Subcutaneous Fat 20
    1.4.1 Biological characteristics 20
    1.4.2 Ultrasound characteristics 20
    1.4.3 Difficulties in Segmentation of Fat in Ultrasound Images 22
1.5 Thesis Objectives and Organization 23

2 Method in Developing Image Processing and Boundary Detection 25
2.1 Processing of Radiofrequency Signal 25
    2.1.1 Calculation of Spectrum Properties 26
    2.1.2 Noise Reduction using Spatial Compounding 28
        2.1.2.1 Implementation 29
        2.1.2.2 Experiments 32
            2.1.2.2.1 Phantom Experiments 32
                2.1.2.2.1.1 Method 32
                2.1.2.2.1.2 Results and Discussions 33
            2.1.2.2.2 Human Experiments 35
                2.1.2.2.2.1 Method 35
                2.1.2.2.2.2 Results and Discussions 36
2.2 Thresholding on Spectrum Properties 40
    2.2.1 Unimodal Thresholding 41
    2.2.2 Thresholding results 42
2.3 Fat Boundary Detection 47
    2.3.1 Extraction of Boundary Candidates 47
    2.3.2 Fitting Boundary Candidates using Random Sample Consensus (RANSAC) . 49
        2.3.2.1 Total Least Squares Fitting 50

2.3.2.2 Theory and Implementation 50
2.3.3 Calculation of Spectral Content using Multiple Focuses 55
2.3.3.1 Stitching Focused Spectrum Properties (MF1) 55
2.3.3.2 Averaging Spectrum Properties from Multiple Focuses (MF2) . . . 56
2.3.3.3 Results 56
2.4 Summary 57

3 Experimental Methodology 59
3.1 Overview of the Human Subcutaneous Fat Detection Framework 59
3.1.1 Data capture 61
3.1.2 Calculation of Spectrum Properties 62
3.1.3 Pre-processing of Spectrum Properties Map 63
3.1.4 Segmentation 63
3.2 Procedures in User Study 65
3.2.1 Measurement of Skinfold Fat Thickness 65
3.2.2 Collection of Ultrasound Data 67
3.2.3 Reference Fat Boundary from Manual Segmentation 68
3.3 Evaluation Method 68
3.3.1 Average Thickness Error Metrics 69
3.3.2 Root Mean Square Error Metric 70
3.3.3 Difference against Mean 70
3.4 Summary 70

4 Evaluation of Results 72
4.1 Qualitative Results: Segmentation Using Spectrum Variance σ_s^2 72
4.2 Evaluation of Segmentation 75
4.2.1 Results: Spectrum Variance σ_s^2 vs Integrated Backscattering Coefficient IBS 76
4.2.1.1 Correlation 76
4.2.1.2 d_{ERR} 79
4.2.1.3 d_{RMS} 80
4.2.2 Results: Multiple-focuses vs Single Focuses 81

4.2.2.1 d_{ERR} 81
4.2.2.2 d_{RMS} 83
4.2.3 Discussions 85
4.3 Comparison of Auto-detected Fat Thickness with Skinfold Caliper Measurements . . 93
4.3.1 Evaluation on Skinfold Caliper Technique 93
4.3.2 Result of Correlation 94
4.3.3 Result of Difference Against Mean 98
4.3.4 Discussions 99
4.4 Summary 100

5 Conclusions and Future Directions 102
5.1 Summary and Conclusion 102
5.2 Future directions 105

Bibliography 108

Appendices 117

A Calculation of the Spectrum Central Frequency and Variance 117

B Normalization of a Spectrum Property Image 119

C Solution to Rosin's Thresholding Method 120

D UBC Research Ethics Board Certificate of Approval 122

List of Tables

4.1 Average d_{ERR} of 36 samples in 9 subjects (4 samples per participant) at the suprailiac, triceps and thigh sites respectively. The paired t-test is used to compare the mean difference between σ_s^2 and IBS. *t(df=35)*: t-value of the paired t-test with a degree of freedom (df) of 35. *CI*: 95% confidence interval (CI) of the statistical mean difference between σ_s^2 and IBS. If the CI does not include 0, there is a significant difference between groups. *p-value*: if a p-value < 0.05, it indicates there is significant difference between the the d_{ERR} of σ_s^2 and IBS. 79

4.2 Average d_{RMS} of 36 samples in 9 subjects (4 samples per participant) at the suprailiac, triceps and thigh sites respectively. The paired t-test is used to compare the mean difference between σ_s^2 and IBS. *t(df=35)*: t-value of the paired t-test with a degree of freedom (df) of 35. *CI*: 95% confidence interval (CI) of the statistical mean difference between σ_s^2 and IBS. If the CI does not include 0, there is a significant difference between groups. *p-value*: if a p-value < 0.05, it indicates there is significant difference between the the d_{RMS} of σ_s^2 and IBS. 80

4.3 Average d_{ERR} of 36 samples in 9 subjects (4 samples per participant) at the suprailiac, triceps and thigh sites respectively. The one-way ANOVA test is used to compare the mean difference among results obtained from the SF, MF1 and MF2. *F(2,105)*: F-value of the one-way ANOVA test with a between-groups degree of freedom of 2 and a within-group degree of freedom of 105. *p-value*: if a p-value < 0.05, it indicates there is a significant difference among the groups. 82

4.4 Tukey's HSD multiple comparisons for the difference in d_{ERR} within a group. SF: single focus at 25mm, MF1: stitching multiple focuses and MF2 averaging multiple focuses. *mean difference*: the estimated statistical mean difference from the Tukey's HSD test. *CI*: 95% confidence interval of the statistical mean difference between groups A and B. 82

4.5 Average d_{RMS} of 36 samples in 9 subjects (4 samples per participant) at the suprailiac, triceps and thigh sites respectively. The one-way ANOVA test is used to compare the mean difference among results obtained from the SF, MF1 and MF2. *F(2,105)*: F-value of the one-way ANOVA test with a between-groups degree of freedom of 2 and a within-group degree of freedom of 105. *p-value*: if a p-value < 0.05, it indicates there is a significant difference among the groups. 84

4.6 Tukey's HSD multiple comparisons for the difference in d_{RMS} within a group. SF: single focus at 25mm, MF1: stitching multiple focuses and MF2 averaging multiple focuses. *mean difference*: the estimated statistical mean difference from the Tukey's HSD test. *CI*: 95% confidence interval of the statistical mean difference between groups A and B. 85

4.7 Summary on reference average thickness of subcutaneous fat collected from 9 participants with 4 samples for each person at each body site. The reference thickness is obtained by manual segmentation on ultrasound data. 86

4.8 Discrepancies in skin-fold caliper measurement taken at the same spot of a body site. 94

4.9 The correlation coefficient r of average thickness between the manual ultrasound segmentation vs $\frac{1}{2}$ skinfold caliper measurements for 18 samples in nine participants (two samples per participant). 95

4.10 The correlation coefficient r of average thickness between the automatic ultrasound segmentation vs $\frac{1}{2}$ skinfold caliper measurements for 18 samples in nine participants (two samples per participant). 95

4.11 Mean difference and standard deviation values between the ultrasound measurements and the $\frac{1}{2}$ skinfold thicknesses. $\overline{D}$ is the mean difference and s is the standard deviation. 99

4.12 A comparison of correlations between ultrasound measurements and skinfold measurements at the suprailiac, thigh and triceps sites in this and past studies. The ultrasound measurements are obtained by automatic segmentation in this study, and by manual segmentation in the above past studies. 100

List of Figures

1.1 Human Subcutaneous Fat in an ultrasound B-mode image. 7

1.2 A group of adjacent elements activated simultaneously to generates an ultrasound pulse and receives reflected echoes. A scan line consists of a single reflected RF signal that is normally amplified and rectified. A B-mode image consists of a collection of scan lines which are taken independently and combined to form an image of pixels. The scan lines are shown parallel here, but may also spread radially in a fan for curvilinear transducers. 12

1.3 The mechanism of focusing using phased timing. 13

1.4 The ultrasound beam steering generated by phased timing. 14

1.5 B-mode images showing subcutaneous fat at different body sites. The thickness of the fat layer is indicated with arrows. 21

2.1 The concept of spatial compounding for reducing speckle in B-mode images. After averaging images taken from different angles, speckle patterns are reduced and the object appears more homogeneous. 29

2.2 Application of spatial compounding on a spectrum property. 30

2.3 Mapping the coordinates from the raw data space to the real space by geometry. A_1 is a spectrum property value at its raw data coordinates (x_1, y_1) in the parametric image obtained from the steering angle θ. A_2 is the corresponding spectrum property value of A_1 at the real spatial coordinates (x_2, y_2). 31

2.4 The slope $\frac{df_c}{dy}$ of the linear regression line is proportional to the attenuation rate of a specific phantom layer. The red line is f_c and the green dot line is the linear regression line of f_c. 33

2.5 Reduction of the standard deviation in estimating the slope m of an f_c scan line using spatial compounding with different step sizes of steering angle θ and different numbers of angles. The data points are fitted by the function $\frac{1}{x}$. 34

2.6 Improvement in the standard deviation of estimating the slope m of the f_c scan line using neighbour averaging with varying number of neighbour scan lines. 35

2.7 Improvement in spectrum properties at a human suprailiac site after using spatial compounding. (a) B-mode image. (b)Spectrum Properties(f_c, σ_s^2 and IBS). The left most column shows the spectrum properties without spatial compounding. The second and third columns show the compound spectrum properties using 5 and 11 angles of step size 2° respectively. 38

2.8 Improvement in spectrum properties at a human triceps after using spatial compounding. (a) B-mode image. (b)Spectrum Properties(f_c, σ_s^2 and IBS). The left most column shows the spectrum properties without spatial compounding. The second and third columns show the compound spectrum properties using 5 and 11 angles of step size 2° respectively. 39

2.9 Improvement in spectrum properties at a human thigh after using spatial compounding. (a) B-mode image. (b)Spectrum Properties(f_c, σ_s^2 and IBS). The left most column shows the spectrum properties without spatial compounding. The second and third columns show the compound spectrum properties using 5 and 11 angles of step size 2° respectively. 40

2.10 Detection of threshold using Rosin's thresholding method on (a) unimodal histogram and (b) bimodal histogram. 42

2.11 Results of thresholding on spectrum properties captured at the human suprailiac site. (a) B-mode image. (b) Spectrum properties' images(1^{st} row), their histograms (2^{nd} row) and binary maps (3^{rd} row). The vertical line in the histogram indicates the calculated threshold. 44

2.12 Results of thresholding on spectrum properties captured at the human triceps site. (a) B-mode image. (b) Spectrum properties' images(1^{st} row), their histograms (2^{nd} row) and binary maps (3^{rd} row). The vertical line in the histogram indicates the calculated threshold. 45

2.13 Results of thresholding on spectrum properties captured at the human thigh site. (a) B-mode image. (b) 2^{nd} to 4^{th} row: a spectrum property's image, histogram and binary map respectively. The vertical line in the histogram indicates the calculated threshold. 46

2.14 An example illustrates the extraction of boundary candidates in (a) a binary map of σ_s^2 using Equation 2.8 and (b) a binary map of IBS using Equation 2.9. A white pixel represents the value of one and a black pixel represents a pixel of zero. Blue solid crosses denote the boundary candidates obtained in the vertical direction and green dotted crosses denote the boundary candidates obtained in the horizontal direction. 48

2.15 Results of extraction and detection of boundary candidates from the binary map $BM_{\sigma_s^2}$ obtained from a human suprailiac site: (a) potential boundary candidates (red crosses) and (b) fat boundary candidates found by RANSAC (red crosses). . . . 52

2.16 Results of extraction and detection of boundary candidates from the binary map BM_{IBS} obtained from a human suprailiac site: (a) potential boundary candidates (red crosses) and (b) fat boundary candidates found by RANSAC (red crosses). . . . 53

2.17 Results of extraction and detection of boundary candidates from the binary map $BM_{\sigma_s^2}$ obtained from a human triceps: (a) potential boundary candidates (red crosses) and (b) fat boundary candidates found by RANSAC (red crosses). 53

2.18 Results of extraction and detection of boundary candidates from the binary map BM_{IBS} obtained from a human triceps: (a) potential boundary candidates (red crosses) and (b) fat boundary candidates found by RANSAC (red crosses). 54

2.19 Results of extraction and detection of boundary candidates from the binary map $BM_{\sigma_s^2}$ obtained from a human thigh: (a) potential boundary candidates (red crosses) and (b) fat boundary candidates found by RANSAC (red crosses). 54

2.20 Results of extraction and detection of boundary candidates from the binary map BM_{IBS} obtained from a human thigh: (a) potential boundary candidates (red crosses) and (b) fat boundary candidates found by RANSAC (red crosses). 55

2.21 Stitching of a spectrum property map obtained from multiple focuses: (a) stitching of spectrum properties values (b) the weight function that combines two overlapping regions. 56

2.22 The comparisons between (a)σ_s^2 and (b)IBS obtained from: (1^{st}-4^{th} column) single focuses (SF) where **F** indicates the focus position, (5^{th} column) stitching spectrum properties from multiple focuses (MF1) and (6^{th} column) averaging spectrum properties from multiple focuses (MF2). 57

3.1 The framework of human subcutaneous fat detection. 60

3.2 The sequence of capturing RF data. 62

3.3 An example illustrates the segementation process on the parametric images of σ_s and IBS. 64

3.4 Body sites selected for skinfold caliper and ultrasound measurements. The direction of the arrows indicates the grasp of the skinfold caliper. 66

3.5 A Lange skinfold caliper. 67

3.6 A figure showing the mean difference $\overline{D}$ and the standard deviation of differences(s) between two methods. Example data are provided for illustration. 71

4.1 Examples (1^{st} row: suprailiac, 2^{nd} row: triceps and 3^{rd} row: thigh) demonstrate the segmentation results of σ_s^2 at a single focus obtained from different structures and thicknesses of subcutaneous fat tissue. The cyan boundary is the manual segmentation and the red boundary is the automatic segmentation. 74

4.2 Two examples demonstrate the segmentation results of σ_s^2 on participants with fat thickness $\leq$5mm. Ultrasound data is obtained using a single focus positioned at 25mm. In sub-figures (a) and (b), the left image is the binary image of σ_s^2 and the right image is the B-mode image. The cyan boundary is the manual segmentation and the red boundary is the automatic segmentation. 75

4.3 Correlation between manual and automatic measurements using σ_s^2 at the (a) suprailiac (b) triceps and (c) thigh sites. The red dashed line represents the one-to-one relationship, the blue line is the linear regression line of the 36 samples (blue crosses). 77

4.4 Correlation between manual and automatic measurements using IBS at the(a) suprailiac (b) triceps and (c) thigh sites. The red dashed line represents the one-to-one relationship, the blue line is the linear regression line of the 36 samples (blue crosses). 78

4.5 Show the results of IBS and σ_s^2 at the (a) suprailiac, (b) thigh and (c) triceps sites. IBS is not reliable in locating the fat boundary at the thigh and triceps because of the presence of other soft tissues with strong reflection. In subfigures (a),(b) and (c), from left to right: binary map from IBS, segmentation result from IBS, binary map from σ_s^2 and segmentation result from σ_s^2. The cyan boundary is the manual segmentation and the red boundary is the automatic segmentation. 87

4.6 An example showing the improvement of using MF2 over SF and MF1. In subfigures (a) SF,(b) MF1 and (c) MF2, from left to right: binary map of σ_s^2 and, segmentation result of σ_s^2. The cyan boundary is the manual segmentation and the red boundary is the automatic segmentation. 89

4.7 An example showing the improvement of using MF2 over SF and MF1. In subfigures (a) SF,(b) MF1 and (c) MF2, from left to right: binary map of σ_s^2 and, segmentation result of σ_s^2. The cyan boundary is the manual segmentation and the red boundary is the automatic segmentation. 90

4.8 An example showing the improvement of using MF2 over SF and MF1. In subfigures (a) SF,(b) MF1 and (c) MF2, from left to right: binary map of σ_s^2 and segmentation result of σ_s^2 at a triceps. The cyan boundary is the manual segmentation and the red boundary is the automatic segmentation. 91

4.9 The relationship of the average thickness between the ultrasound and the skinfold measurements at the suprailiac site: (a) manual ultrasound detection vs $\frac{1}{2}$ skinfold (b) automatic ultrasound detection vs $\frac{1}{2}$ skinfold. 96

4.10 The relationship of the average thickness between the ultrasound and the skinfold measurements at the triceps : (a) manual ultrasound detection vs $\frac{1}{2}$ skinfold (b) automatic ultrasound detection vs $\frac{1}{2}$ skinfold. 97

4.11 The relationship of the average thickness between the ultrasound and the skinfold measurements at the thigh: (a) manual ultrasound detection vs $\frac{1}{2}$ skinfold (b) automatic ultrasound detection vs $\frac{1}{2}$. 98

5.1 Moving the transducer parallel to the skin to generate cross sectional images in a volume. 106

C.1 Finding the threshold by Rosin's thresholding method. 120

Glossary

In vitro In an artificial environment outside the living organism.

In vivo Within a living organism.

A-mode The amplitude mode of ultrasound imaging.

Adipocyte A fat cell from human tissue.

Adipose tissue Also known as fat tissue. Is a layer of loose connective tissue specialized in storing lipids.

Agar A gelatinous material that controls the stiffness of a phantom.

Air-displacement plethysmography A device that measures the percentage of body fat by immersing a subject in a closed air-filled chamber.

ANOVA Analysis of variance.

Attenuation Decrease in amplitude and intensity over a distance travelled by a wave.

B-mode The brightness mode of ultrasound imaging.

Beam focusing The concentration of the ultrasound beam into a small beam area.

Beam steering The change of direction of the ultrasound beam.

BIA Bioelectrical impedance analysis. A equipment that measures fat in terms of tissue conductivity.

Bimodal histograms A histogram with two distinct modes.

Binary image An image consisting of only zeros and ones.

Cellulose A complex carbohydrate that controls the scattering of a phantom.

Collagen A long, fibrous protein structure that makes up the connective tissue.

Connective Tissue A type of soft tissue that contains collagen. It connects and supports organs and tissues of the body.

CT Computed tomography.

DEXA Dual Energy X-ray Absorptiometry. A method that uses two low doses of X-ray beams with different energy levels to detect bone and soft tissues.

DFT Discrete Fourier transform.

Echogenicity The relatively strength of echoes. A higher echogenicity (i.e. hyperechoic) means a tissue structure having relatively strong echoes; a lower echogenicity (i.e. hypoechoic) means a tissue structure having relatively weak echoes.

Elastography The measurement of the elastic properties of tissue with ultrasound.

Energy absorption Energy is absorbed and converted to heat when the sound wave propagates through tissue.

Fascia A sheet of fibrous connective tissue covers and separates muscles, organs, and other soft tissues. It can be used to refer to the strong acoustic interface between subcutaneous fat and the muscle layer.

IBS Integrated backscatter coefficient. It indicates the total reflected power and strength of the backscattering.

Interface A surface that separates two kinds of soft tissues.

Lagrange multiplier A method for optimizing a function that has several variables subject to one or more constraints.

MF1 The method of stitching values of a spectrum property obtained at multiple focal positions.

MF2 The method of averaging values of a spectrum property obtained at multiple focal positions.

MRI Magnetic resonance imaging.

Obese A person is obese if an excessive storage of body fat (women with more than 35% of body fat and men with more than 25% of body fat is accumulated in the body.)

Parametric image A two-dimensional image of a spectrum property whose values are encoded into gray-intensity scale.

Phantom An artificial object that has some acoustic properties of soft tissues.

Pulse-Echo Ultrasound Imaging A clinical ultrasound imaging technique that uses the same transducer for both the pulse generator and echo detector.

RANSAC Random Sample Consensus.

Raw data coordinates The coordinates calculated with respect to the transducer.

Reverberation Multiple ultrasound reflections between a structure and the probe.

RF signal Radio-frequency signal is the raw signal of ultrasound.

Sagittal The sagittal plane of the human body is an imaginary plane that symmetrically divides the body into right and left sections.

Scan line A single line of ultrasound data that is parallel to the axial direction.

Scattering The redirection of sound in several directions.

Segmentation The partitioning of an image into two or more regions.

SF Single focus at 25mm.

Skinfold caliper A caliper that measures skinfold thicknesses by pinching a fold of skin and the underlying subcutaneous fat.

Spatial compounding The averaging of multiple overlapping data for reducing speckle noise.

Speckle Acoustic noise in ultrasound imaging due to the destructive and constructive interference of ultrasound pulses with randomly distributed scatters.

Spectrum properties The properties of the power spectrum of the raw radio-frequency ultrasound data.

STFT Short time Fourier transform.

Subcutaneous fat The fat layer that is immediately underneath the skin.

Suprailiac The area on the side of human waist and on the iliac crest.

TGC Time gain compensation.

Thigh The area between the pelvis and buttocks, and the knee at the lower limb.

Transducer A device, which consists of an array of piezoelectric elements, generates ultrasound pulses by converting electrical energy to acoustical energy.

Triceps A large three-headed skeletal muscle runs along the back of the upper arm of human.

Underwater weighing A method that measures the percentage of body fat by immersing a subject in a water tank.

Unimodal histograms A histogram with only one distinct mode.

Visceral fat The fat layer that is located around internal organs.

Notation

$BM_{IBS}(x,y))$	A binary image that contains the potential boundary candidates obtained from IBS.
$BM_{\sigma_s^2}(x,y)$	A binary image that contains the potential boundary candidates obtained from σ_s^2.
CI	The confidence Interval.
$IBS(x,y,F)$	A value of IBS at the coordinates (x,y) of the spatial compounded parametric image obtained at the focal position of F.
$IBS(x,y,\theta,F)$	A value of IBS at the coordinates (x,y) of the parametric image obtained at the steering angle θ and focal position of F.
N	The number of angles used in the spatial compounding.
$S(w)$	The power spectrum.
W	The bandwidth of the spectrum.
$\frac{df_c}{dy}$	The rate of change of central frequency along the depth.
$I\hat{B}S(x,y)$	The spatially compounded parametric image of IBS after combining values from different focal positions.
$\hat{\sigma_s^2}(x,y)$	The spatially compounded parametric image of σ_s^2 after combining values from different focal positions.
λ	The wavelength of an ultrasound pulse
$\overline{D}$	The mean difference between two methods.
ϕ	The step size of angles used in the spatial compounding.
σ_s^2	Variance of the spectrum.
$\sigma_s^2(x,y,F)$	A value of σ_s^2 at the coordinates (x,y) of the spatial compounded parametric image of obtained at the focal position at F.

$\sigma_s^2(x, y, \theta, F)$	A value of σ_s^2 at the coordinates (x,y) of the parametric image obtained at the steering angle θ and focal position of F.
$b_{BM_{IBS}}(x, y)$	A binary image that contains the fat boundary points obtained from IBS.
$b_{BM_{\sigma_s^2}}(x, y)$	A binary image that contains the fat boundary points obtained from σ_s^2.
c	The speed of sound.
d_{ERR}	The average thickness error of a detected boundary.
d_{RMS}	The root mean square error of a detected boundary.
f_o	The central frequency of the transducer.
f_c	The central frequency of the power spectrum.
m_j	The jth moment of a power spectrum.
s	The standard deviation of difference between two methods.
$x(t)$	A window of RF signal.
$IBS(x, y)$	The parametric image of IBS for segmentation.
$\sigma_s^2(x, y)$	The parametric image of σ_s^2 for segmentation.
k	A parameter of the RANSAC algorithm. It is the number of iterations required for the algorithm.
n	A parameter of the RANSAC algorithm. It is the smallest number of points required to fit the model.
t	A parameter of the RANSAC algorithm. It is the threshold (in pixel) required to determine if the data fit well.
IBS	Integrated backscatter coefficient.

Acknowledgements

First of all, I would like to thank my supervisors, Dr. Peter Lawrence and Dr. Robert Rohling for their guidance, direction, advices and support for my thesis project. Their expertise in ultrasound imaging and signal processing, and constructive feedbacks were necessary for the success of this project. Not only I have gained more research experience, but also learned how to deal with difficult situations.

Many thanks to all the participants of the experiment. I really appreciate their contribution, time and patience in completing the user study. This project would not be accomplished without their volunteer. I would also like to thank Barry Legh, the senior instructor from the Human Kinetics Department of UBC, for teaching me the techniques of using the skinfold caliper and to lend me the Lange skinfold caliper for the experiment.

In addition, I would like to thank all the coworkers in the Robotics and Control Lab for sharing knowledge and maintaining an excellent research environment. The assistance in using the research package to capture RF data from the software engineers in Ultrasonix are also gratefully appreciated.

Many thanks to my wonderful friends – especially to Angie, Vincci, Sheffield, Joyce, Sophia, Vivian, Simon, Horace and Aaron. Thank you for their listening, sharing, encouragement and all the fun activities to balance out my life. I greatly value their friendships and appreciate their belief in me. Also, thank Joyce and Raymond for providing comments for the thesis.

Finally, I have been fortunate to have Jo in my life. I appreciate his understanding, patience, love and his faith in me. He has also provided me with technical opinions. Thank you for accompanying me to go through all the ups and downs and supporting me every step along the way.

I am indebted to my family for encouraging me to pursue this study. Their continuous support, encouragement, patience and love are important for me to stay focus in my research.

Chapter 1

Background and Introduction

Early interest in measuring human body fat distribution can be dated back to 1921 when Matiegka [1] developed body fat predictive equations from subcutaneous fat skinfold thickness, body length, width and circumferences. Body fat analysis has been useful in assessing obesity to prevent health risk, monitoring athletes' health status for giving appropriate nutritional counselings and monitoring body shapes and weight for sports competition such as gymnastics and wrestling. Skinfold caliper measurement, body density weighing and bioelectrical impedance analysis have been popular in assessing body fat. Recent advances in measuring body fat include the introduction of clinical imaging techniques such as computed tomography, magnetic resonance imaging and ultrasound. These techniques produce images of human anatomy and provide a more accurate technique for researchers. Among these imaging techniques, we are especially interested in ultrasound imaging because of its portability, safety and relatively low cost.

Diagnostic ultrasound is a non-invasive, portable imaging device used mainly for clinical diagnosis concerning organs and soft tissue. Recently, there has been a growing interest in assessing body composition using ultrasound – in particular measuring thickness of subcutaneous fat. For example, researchers proposed to use ultrasound in order to overcome the drawbacks of compressibility and elasticity in skinfold caliper measurements [2]. Other proposals include using it for measuring the thickness of subcutaneous fat of obese persons [3] and on elderly people or at sites that are not convenient for skinfold caliper measurement [4]. Perin *et al.* [5] also evaluated the occurrence of natural variations in thigh and abdominal subcutaneous fat thickness related to the phases of the menstrual cycle by using ultrasound measurements. In animals, ultrasound was used to predict intramuscular fat percentage at regions of interest by texture analysis in live swine [6]. Meanwhile, Abe *et al.* [7] attempted to calculate the subcutaneous fat volume by multiplying the fat thickness obtained from B-mode ultrasound by the skin surface area. In wrestling, Saito *et al.* [8] measured the subcutaneous fat thickness of wrestlers at specific body sites and developed equations to predict percentage of body fat. All of these methods have involved the manual analysis of the ultrasound data to extract quantitative measurements.

This thesis proposes to develop an automatic method to detect the subcutaneous fat thickness using ultrasound *in vivo* . In this introductory chapter, we will first survey the current techniques of human body fat measurement and describe our motivation. After that, we will present the principles of ultrasound based on the pulse-echo technique. The properties of subcutaneous fat thickness and the difficulties in ultrasound detection are then discussed. Lastly, the thesis objectives and organization are presented.

1.1 Current Techniques of Human Body Fat Measurement

Current techniques that measure human body fat can be divided into the following categories: body density weighing, bioelectrical impedance analysis (BIA), skinfold caliper, and imaging techniques such as dual energy X-ray absorptiometry, computed tomography, magnetic resonance imaging and ultrasound imaging. Although they have the same goal of measuring body fat, their assumptions are different. For example, the body density weighing method estimates the percentage of body fat based on the body density whereas the BIA measures the fat tissues in terms of tissue conductivity. The skinfold caliper measures skinfold thicknesses at specific body sites and the percentage of fat is calculated based on these measurements. Compared with the above methods, the imaging techniques are more direct in measuring body fat as they can image fat directly as soft tissues. The current techniques of measuring body fat are summarized in this section.

1.1.1 Body Density Weighing

Underwater weighing and air-displacement plethysmography are two common methods that estimate the percentage of body fat based on body density [9]. The body density can be computed from the body volume and mass.

1.1.1.1 Underwater Weighing

The underwater weighing technique requires the subject to be immersed in a tank of water while fully exhaling. The calculation of the body density is based on Archimedes's principle. This principle states that the weight loss under water is directly proportional to the volume of water displaced. The fat tissues are less dense than the bones and muscles; therefore, a person with a higher percentage of fat makes the body lighter in water [10]. This method is time consuming and its equipment requires a lot of space. The results can be affected by the amount of air existing in the subject's lungs, changes in hydration and proportion of bone minerals. Moreover, the subjects have to be fully immersed in water and this may cause discomfort.

1.1.1.2 Air-displacement Plethysmography

The air-displacement plethysmography requires a subject to immerse in a closed air-filled chamber. At a fixed temperature, the body volume of the subject can be directly measured by Boyle's law which states an inverse relationship between the pressure versus volume. This method does not require the subjects to immerse in water. Also, multiple readings can be recorded in a short period of time. Therefore, the air-displacement plethysmorgraphy has begun to replace the underwater weighing method [9]. Further, a good linear correlation of 0.94 is shown between between the underwater weighing and air-displacement plethysmography [11]. Nevertheless, the accuracy of this method can be affected by changes in breathing pattern and movement of the subject.

1.1.2 Bioelectrical Impedance Analysis

The bioelectrical impedance analysis equipment measures fat in terms of tissue conductivity. Lean tissue and water conduct electricity better than fat tissue; therefore, the measurement of the resistance to electrical current can be used to estimate the percentage of body fat. For the traditional bioelectrical impedance analyzer (e.g. Tanita BIA scales), spot electrodes are placed on a person's bare feet. The resistance of a small electrical signal is measured as it passes through the body. By modeling a body as a cylindrical conductor with its length proportional to the subject's height, the impedance index can be calculated as the ratio of height square to body impedance [9]. This method is easy to operate, inexpensive, portable and fast (less than 1 minute). However, it tends to overestimate the body fat in obese people, and cannot distinguish between body fat and fluid[12].

1.1.3 Skinfold Caliper

The skinfold caliper measures skinfold thicknesses by pinching a fold of skin and the underlying subcutaneous fat. The average of multiple readings is needed at each body site to enhance accuracy. The common practice is to obtain skinfold thicknesses at three or four body sites and estimate the percentage of body fat using predictive equations [13].

The predictive equations calculate the percentage of body fat by substituting the values of fat thicknesses measured at several sites into a formula. Skinfold test formulas exist in many forms and are derived by human skinfold experiments. These formulas make use of the fat thicknesses measured at several sites for reducing measurement errors to calculate body fat percentage. For example, the equations developed by Jackson and Pollock [14, 15] used fat thicknesses measurements from the triceps, suprailiac and thigh sites for females, and the chest, abdominal and thigh sites for males. Yuhasz [16] used the fat thickness measured at the triceps, subscapular, supraspinal, abdominal, thigh and calf sites for all male and female subjects. The constants in the equations can be different between males and females.

This method is the most widely used tool for evaluating body fat as it is fast, inexpensive and convenient [17]. However, there are drawbacks of this method. The precision of the measurements can be affected by the compressibility, thickness and water content of the subcutaneous fat layer, and also the elasticity of skin. Therefore, it is not possible to make precise measurements in obese people, the elderly, athletes in training, and those experiencing rapid weight gain or loss [2, 13]. The quality of the calipers is also a factor: skinfold calipers should be accurately calibrated and should have a constant specified pressure applied. Also, the precision of the method heavily depends on the skill of a technician. Furthermore, the skinfold caliper is not suitable for all body locations. For instance, Nordander *et al.* [4] attempted to measure skinfold thickness directly over the trapezius but was not successful. The failure was due to the difficulty of grasping the skinfold.

1.1.4 Imaging Techniques

Dual Energy X-ray Absorptiometry (DEXA), Computed tomography (CT), magnetic resonance imaging (MRI) and ultrasound are commonly used imaging techniques for clinical diagnostic purposes and they have also been introduced to quantify human body fat.

1.1.4.1 Dual Energy X-ray Absorptiometry

The Dual Energy X-ray Absorptiometry uses two low doses of X-ray beams with different energy levels to detect bone and soft tissues. By assuming constant attenuation of the pure fat and lean tissues within the soft tissues, the portion of fat and lean can be interpolated from each soft tissue pixel [18]. Tothill *et al.* [19] show a 15% difference in body composition was noticed between the equipment produced from different manufacturers. The accuracy of DEXA is dependent on the technology, method of calibration and interpolation of fat tissue. DEXA is costly and not portable. It also exposes subjects to ionizing radiation hazards. A trained technician is required to operate the equipment. In addition, DEXA provides projection images and can only present the percentage of body fat that represents a substantial region.

1.1.4.2 Computed Tomography

CT is a radiological technique that generates cross section images of human anatomy using X-ray beams. By measuring the intensity of attenuated X-ray beams, the fat tissue, lean tissue and bones can be recognized. The fat tissue can be recognized as attenuation values between -190 to 30 Hounsfield units (HU). Although slightly different intervals of attenuation values can be observed between investigators, they only have minor influence on the results [20]. Since the 1980s, several studies have measured the areas of abdominal subcutaneous and visceral fat using CT [21] and calculated the fat tissue volume [22, 23] . The volume of fat could be calculated by multiplying a cross-sectional area of fat tissue by the distance between each slice [22]. CT is used as a gold standard of body fat measurements because of its excellent accuracy and precision [17, 25]; however, its immobility, high cost and exposure to a high dose of radiation make it inappropriate for frequent use.

1.1.4.3 Magnetic Resonance Imaging

MRI is an imaging technique that uses both a strong magnetic field and a radio frequency electro magnetic pulse. The nuclei of hydrogen atoms in human soft tissues interact with the magnetic field that is generated from the machine. Then, the pulsed radio frequency is applied to interact with the hydrogen protons. After that, the radio frequency pulse is turned off and the protons release the absorbed energy at a certain rate. The rate of energy release, which is the relaxation time, is related to the properties of the soft tissues. The adipose tissue (i.e. fat tissue) has a typical, short longitudinal relaxation time compared to other tissue [26]. High contrast between the fat tissue and adjacent muscles can be generated by a T1 weighted inversion recovery pulse sequence [27].

Foster el al. [27] first applied MRI to research in body composition in 1984. MRI was used to characterize the distribution of human subcutaneous fat tissues in 1988 [28]. The fat and lean tissues were observed at the mid-abdomen level and also for the whole body [29]. As in the case of CT, the volume of fat can be calculated by multiplying the cross-sectional area by the thickness of each image slice. Despres [20] summarized that MRI has a higher expected error for the measurements of visceral fat than the measurements of subcutaneous fat. The coefficient of variation is in the range from 1.1% to 10.1% for the repeated measurements of subcutaneous fat and is in the range from 5.3% to 10.6% from the repeated measurements of visceral fat. He also concluded that CT and MRI are the methods of choice for precise measurement of the subcutaneous and visceral fat.

In terms of segmentation, Positano *et al.* [30] investigated the unsupervised segmentation of both abdominal subcutaneous and visceral fat tissue by fuzzy clustering approach using MRI images. High linear correlations were found in the segmentation of both subcutaneous fat ($r = 0.9917$) and visceral fat ($r = 0.9601$) when the results are compared with manual segmentation. Their method of segmentation overestimated the volume of subcutaneous fat with a mean percentage difference of 6.4%, but underestimated the volume of visceral fat by a mean percentage different of 7.9%.

1.1.4.4 Ultrasound

Ultrasound is sound at frequencies that are above the range of human hearing: from 20kHz to several hundred MHz. A higher frequency of ultrasound gives a better resolution, but, in turn, has a lower penetration power. Medical ultrasound usually uses frequencies from 1MHz to 10MHz; however, high frequency ultrasound ranging from 20MHz to 45MHz has also been used in characterizing relatively shallow skin structures. Tissue boundaries can be distinguished because ultrasound pulses are reflected at interfaces between tissues with different acoustic properties. The amplitude mode (A-mode) and the brightness mode(B-mode) are two common modes of displaying the reflected ultrasound echoes of soft tissue. Both of the modes involve the use of a focused ultrasound beam that interrogates tissue along a line in space. In A-mode, reflected echoes are represented as

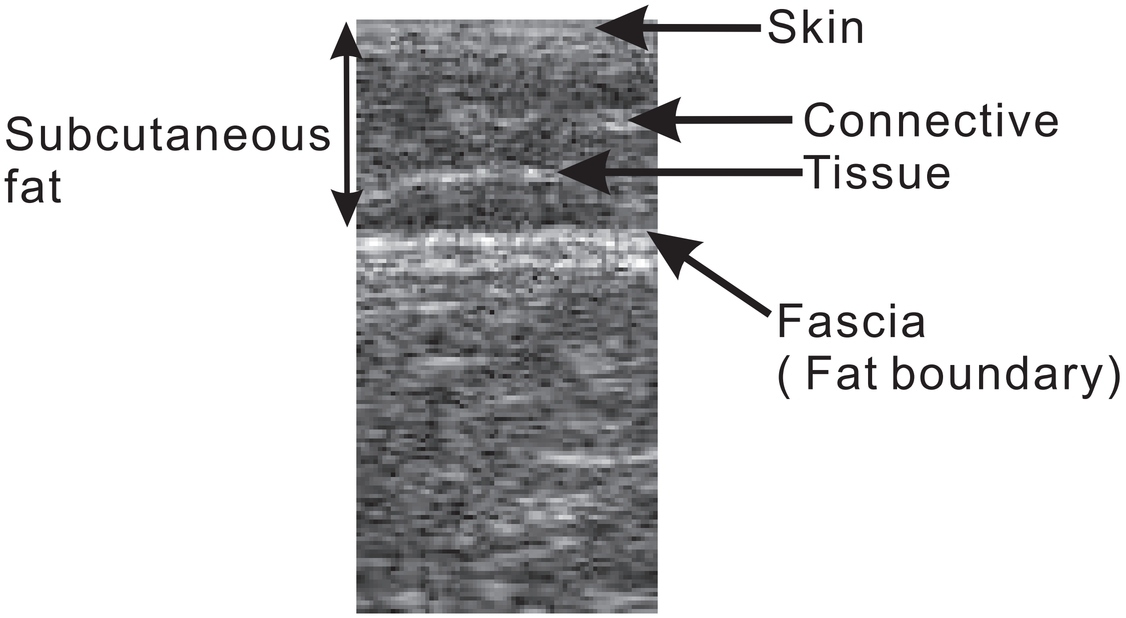

Figure 1.1: Human Subcutaneous Fat in an ultrasound B-mode image.

amplitude versus depth in one-dimension. In B-mode, multiple equally spaced beams are used and reflected echoes are represented as two-dimensional brightnesses images whose axes correspond to the lateral and axial direction of the scanning plane. In this way, each column of a B-mode image can be considered as a form of A-mode data. Tissues with stronger reflection are represented by brighter intensities in both A-mode and B-mode images.

The first mention of measuring subcutaneous fat thickness with ultrasound was in 1966 [31]. It was not until 1984 that Volz and Ostrove [32] used a portable A-mode ultrasound to quantitatively determine subcutaneous fat thickness in college woman. A-mode ultrasound measures the fat thickness by estimating the time required by an ultrasound pulse to be reflected from the fascia (i.e. the strong acoustic interface between subcutaneous fat and the muscle layer). They found a lack of agreement between ultrasound and half skinfold measurements: agreement ranged from 87% at supraprailiac to 141% in thigh. The large range of error was believed to be caused by multiple echoes reflected by the connective tissue layers dispersed within the fat tissues. Therefore, A-mode ultrasound alone is not sufficiently reliable to measure fat thickness. The later introduction of B-mode ulrasound machines, which generate cross-sectional slices instead of just lines, makes it easier to interpret the depth of subcutaneous fat as two-dimensional ultrasound can depict the structural information about the subcutaneous fat layer. Various studies have been carried out to demonstrate the reliability and reproducibility of B-mode ultrasound for quantifying subcutaneous fat. For instance, Kuczmerski *et al.* [3] measured subcutaneous fat thickness on obese adults to overcome the limitations of the skinfold calipers in 1987. They proved that ultrasound is superior to the caliper technique in the prediction of the body density of obese persons. Bellisari *et al.* [33] recommended ultrasound as a measurement tool for subcutaneous fat. They evaluated the intra and inter-observer error and found that technical error was less than 0.2mm except in the female triceps where the inter-observer error was found to be 0.62mm. The reliability between observers was above 90% except in the paraspinal site (82%). Flygare *et al.* [34] proved that ultrasound can reproduce measurements of subcutaneous fat in infants when performed by the same operator. In 1996, Abe *et al.* [7] attempted to calculate subcutaneous fat volume by multiplying the fat thickness obtained from B-mode ultrasound with the skin surface area. They found that the volume of fat measured by ultrasound was significantly correlated ($r = 0.79$-0.95) with MRI measurements at the forearm, upper arm, trunk, thigh and lower leg. Other researchers using manual ultrasound methods have found that there are also high correlations between ultrasound and skinfold methods [32, 35, 36, 37, 2].

CT and MRI are able to measure visceral fat by subtracting subcutaneous fat from the total fat tissue[20]. However, ultrasound is not a good choice for quantifying visceral fat due to its low resolution and poor penetration. Nevertheless, Tornaghi *et al.* [25] proposed one valid method to indirectly assess the amount of visceral fat with ultrasound by measuring the intra-abdominal depth that correlates to the amount of visceral fat area.

1.2 Motivation

Subcutaneous fat thickness is accepted as a body fat indicator because about 40 to 60% of total body fat is in the subcutaneous regions [38] and it is appropriate to use the distribution of subcutaneous fat as an indicator. Measuring subcutaneous fat is important in relation to human health problems, athletic performance and general public interest.

Assessing human health risk – Body fat percentage can be used to assess obesity and human health risk. A person is obese if an excessive storage of body fat (women with more than 35% of body fat and men with more than 25% of body fat [39]) is accumulated in the body. It is generally agreed by health professionals that an obese person has a higher chance of developing health problems such as hypertension, coronary artery diseases, stroke, gallbladder diseases, osteoarthritis, type 2 diabetes, sleep apnea, respiratory problems, and cancers. Obese individuals may also suffer from social stigmatization and discrimination [40].

Evaluating performance of athletes – For professional athletes, monitoring their body weight and percentage of body fat can help to improve and maintain their sports performance. Body weight cannot be the sole indicator relating to the performance of athletes: for the same weight of bodies, more strength and endurance can be generated from bodies composed of more muscle than fat. Therefore, an optimal percentage of body fat can help the athlete to achieve the desired performance in speed, agility, strength and endurance. The optimal percentage of body fat depends on the nature of the sport, the sex of the athlete, and is determined on an individual basis. For example, gymnasts and figure skaters maintain little body fat for appearance and agility while achieving optimal strength. Power sports such as football, skiing, volleyball and hockey require more fat (5 to 19% in males and 10 to 20% in females [41, 42]) to achieve a higher strength-to-weight ratio for generating power. Sports like wrestling, weight lifting and body building set limitations in terms of body weight. Saito *et al.* [8] state that it is important to develop a method for measuring the body fat percentage of sumo wrestlers so that their weight can be monitored to prevent obesity-related diseases and also to maintain their competitive athletic performance and qualification for a specific weight category. Athletes may suffer from eating disorders and poor energy level when the level of body fat is too low and this can be an indication of over-training. There is also a trend in female atheletes to suffer from disruptions of menstrual cycles [43], amenorrhea and osteoporosis [42].

General public interest in modern culture – Our modern culture and fashion industry tend to emphasize personal body shape, appearance and slimness. Under peer pressure, people may consider being fat or carrying excessive fat at a particular body site to be unattractive. Obese individuals may also be afraid of discrimination. Due to these social and psychological issues, people are eager to monitor their body fat distribution, not only to minimize health problems, but also for the sake of appearance.

In general clinical practice, medical practitioners commonly use BMI as an indicator of obesity because it is easy to obtain. However, this method is not reliable [44]. On the other hand, it is inappropriate to assess athletes based solely on body weight because this does not reflect the percentage of body fat. Development of a precise method to measure subcutaneous fat will allow people to monitor their body fat percentage. Based on the measurements, health care practitioners can provide diet and nutritional counseling, recommendations on aerobic and exercise activities that will prevent and control obesity, get the body in shape and set personal fitness goals.

As discussed in section 1.1, there are several methods to estimate body fat percentage. Compared with techniques like body density weighing, BIA or skinfold caliper measurement, ultrasound imaging is superior because it can provide real images of fat. Moreover, ultrasound imaging is more portable and cheaper than DEXA, CT and MRI. Also, it does not require a radiation dose. The above factors make it ideal for measuring subcutaneous fat thickness for general use. Moreover, ultrasound imaging can be used to observe the macroscopic structure of the fat layer [2]. Studies also show that ultrasound is reliable and its results are repeatable for inter-observer data. [33, 45].

The above reasons have motivated us to investigate the possibility of the automatic detection of human subcutaneous fat. Although ultrasound has been introduced to measure subcutaneous fat for a few decades, we are not aware of any published work related to the automatic detection of subcutaneous fat *in vivo*. Indeed, Glasbey *et al.* [46] investigated the automatic interpretation of subcutaneous fat in sheep using B-mode imaging. However, their automatic method only interpreted fat boundaries at two locations: the last rib and the third lumbar vertebra where the anatomy is relatively simple and presumed the skin boundary was known. Automatic detection can overcome the tedious task of manual detection, reduce the discrepancy among judgments of different operators, and standardize the measurement technique. We believe that automatic detection of fat thickness using ultrasound may potentially help to bring the technology into general application by making it more user-friendly.

1.3 Pulse-Echo Ultrasound Imaging

Ultrasound machines, which are mainly used for medical applications, are based on the pulse-echo technique. In other words, the same transducer acts as both the pulse generator and echo detector. Ultrasound is generated in pulses and these pulses are reflected from different body soft tissues as the pulse propagates through tissues. These echoes are separated in time and the time is in proportion to the depth of the tissue interfaces. The depth and location of soft tissues can be calculated by the arrival time of a reflected echo using the generalized speed of sound of soft tissues. Moreover, the strength of the reflected echo indicates the difference in acoustic properties at the interfaces. This section describes how an ultrasound machine works, how ultrasound interacts with soft tissue, the influence on the radiofrequency (RF) spectra and the current development of ultrasound image segmentation.

1.3.1 Apparatus

An ultrasound machine consists of three main components: a transducer, an image processing unit and the display unit. The transducer consists of an array of piezoelectric elements which generates ultrasound pulses and receives reflected echoes. A group of adjacent piezoelectric elements can be activated simultaneously generates an ultrasound pulse by converting electrical energy to acoustical energy. The same group also receives reflected echoes as electrical voltages. The reflected, unprocessed radio-frequency echoes are referred to as RF signals. A scan line of RF signal provides amplitude data of the reflected echoes in the axial direction and thus forms A-mode data. A lateral collection of RF scan lines provides the amplitude information in both the axial and lateral directions and thus forms a B-mode image (Figure 1.2). Furthermore, the time sequence of firing of elements within the group can be controlled for the application of beam focusing and steering. Overall, the transducer plays an important role in beam focusing, beam steering and controlling the penetration and resolution of an ultrasound pulse.

Focusing sound beams can improve resolution by reducing the beam width. The ultrasound transducer can control the position of the focal point in three ways: using curved piezoelectric elements, a lens or by phased timing. The first two methods use the geometric shape of the elements or lens to reduce the ultrasound beam width. The phased timing method is more common

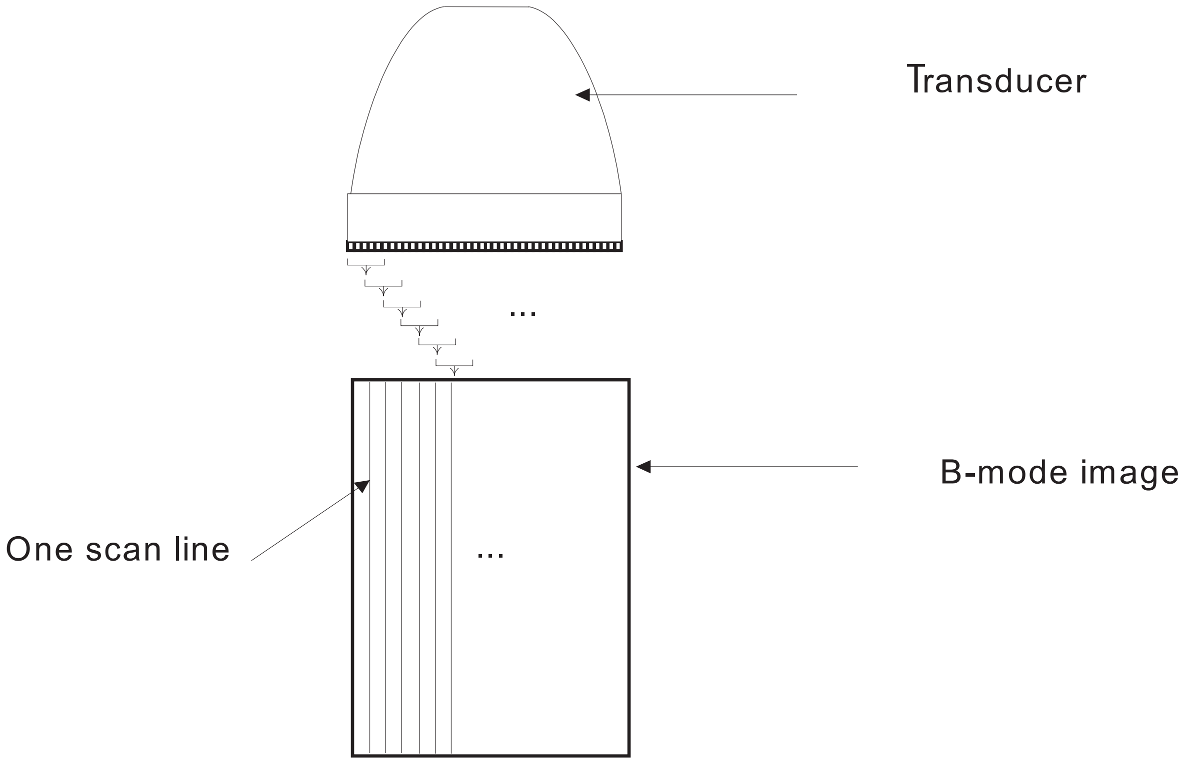

Figure 1.2: A group of adjacent elements activated simultaneously to generates an ultrasound pulse and receives reflected echoes. A scan line consists of a single reflected RF signal that is normally amplified and rectified. A B-mode image consists of a collection of scan lines which are taken independently and combined to form an image of pixels. The scan lines are shown parallel here, but may also spread radially in a fan for curvilinear transducers.

in clinical ultrasound machines and allows the focus to be adjusted electronically. Figure 1.3 shows that pulses can be fired by the element groups at separated time intervals to adjust the apparent curvature of the beam wavefront for controlling the location of the focus. A longer delay between elements in Figure 1.3(a) increases the curvature of the beam wavefront and the focus is moved closer to the transducer, whereas a shorter delay in Figure 1.3(b) decreases the curvature of the beam wavefront and the focus is moved farther from the transducer. This technique allows the use of multiple pulses at each scan line for positioning more than one focal point at different depths; however, the frame rate is decreased due to the need to fire multiple pulses[47].

Moreover, phase timing can also control the beam steering angle by introducing additional phase delays between the firing of individual elements. Figure 1.4 shows that the application of voltage pulses on the element groups with no delays generates a steering angle of zero degrees (no steering), whereas applying voltage pulses with increasing delay from left to right changes the

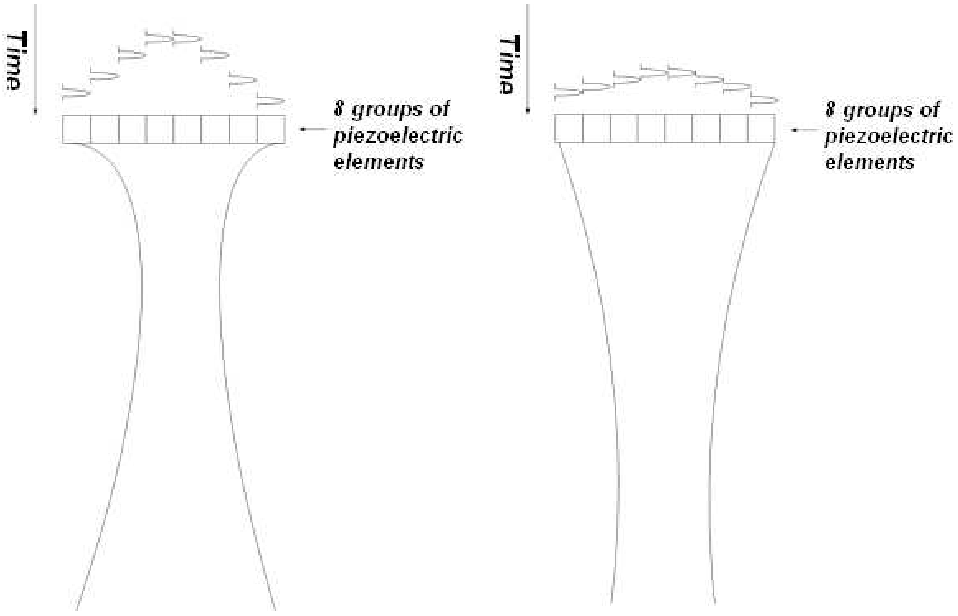

(a) (b)

Figure 1.3: The mechanism of focusing using phased timing.

steering direction to the left and applying voltage pulses with increasing delay from right to left changes the steering direction to the right. Beam steering allows the anatomy to be viewed from different angles. This approach is especially useful for techniques that aim to improve image quality by averaging multiple views of the anatomy and for techniques that generate panoramic images by stitching images together.

Ultrasound focusing can improve resolution at the focal point by reducing the beam width, but the overall system resolution of an ultrasound imaging system is determined mainly by the frequency of the ultrasound pulses. There is always a tradeoff between the system resolution and the penetration power of ultrasound pulses. The penetration and resolution of an ultrasound pulse is directly related to the frequency (f) and the wavelength (λ) of an ultrasound pulse. f and λ are related by the speed of ultrasound (c) via

$$c = f\lambda. \tag{1.1}$$

In most ultrasound machines, c is assumed to be $1540ms^{-1}$ because ultrasound travels at nearly the same speed for most biological tissues. The higher the frequency, the lower the penetration ability

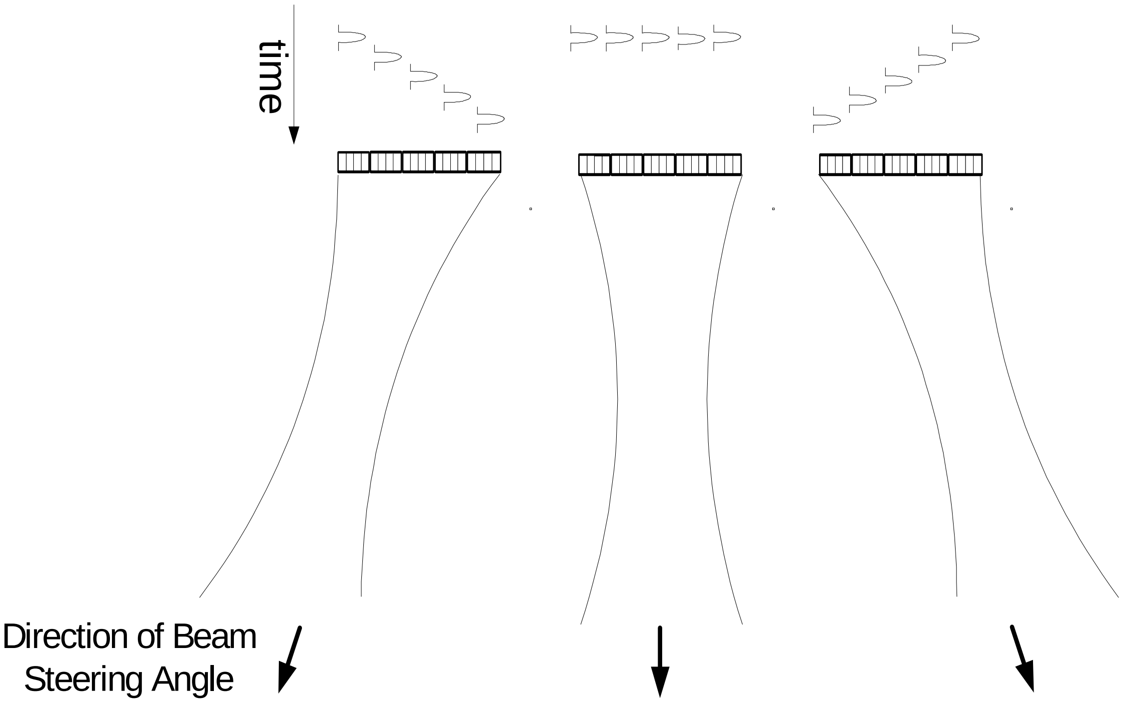

Figure 1.4: The ultrasound beam steering generated by phased timing.

of the ultrasound is. The smaller the wavelength and the shorter the ultrasound pulse, the better the resolution is. Therefore, an increase in frequency reduces the penetration power but improves the resolution; a decrease in frequency increases the penetration power but reduces the resolution. The change of frequency can be achieved by changing the natural frequency of the piezoelectric elements.

To display ultrasound echoes, the received echoes are first amplified by the time gain compensation (TGC). TGC normally increases with depth so that it compensates for the effect of tissue attenuation with depth. After TGC, envelope detection is applied to each scan line of RF data and a brightness image is obtained. The resulting two dimensional brightness image is referred to as an ultrasound B-mode image. In order to display the image, the B-mode image then undergoes the scan conversion process. In this process, the scanlines are mapped to real spatial coordinates according to the dimensions and geometry of the transducer. After that, the amplitude of the signals are calculated and logarithmically compressed to match the dynamic range of the monitor.

1.3.2 Interaction of Ultrasound with Soft Tissues

When an ultrasound pulse is fired from the transducer and propagates through soft tissue, attenuation of the ultrasound energy occurs. Absorption, reflection, refraction and scattering are the most important mechanisms in the attenuation of the ultrasound energy and will be discussed. To simplify the interaction process, we assume there are no diffraction effects from the transducer because it is not directly related to the tissue properties. Moreover, the characteristics of attenuation are determined solely by the acoustic properties of soft tissue.

Reflection occurs at a boundary between two tissues with different acoustic impedances (Z). The acoustic impedance of soft tissue is defined as

$$Z = \rho c \tag{1.2}$$

where ρ is the density in g/m^3 and c is the speed of sound in $m/sec.$ c is assumed to be fixed at 1540m/sec in the ultrasound machine. Given an incident wave perpendicular to a tissue boundary, the amount of wave energy transmitted across the surface is determined by the ratio of acoustic impedances of the two adjacent tissue. The ratio R of reflected intensity $I_{reflected}$ and the incident intensity $I_{incident}$ is

$$R = \frac{I_{reflected}}{I_{incident}} = (\frac{Z_2 - Z_1}{Z_2 + Z_1})^2 \tag{1.3}$$

Lower values of R means more energy is transmitted through the interface.

Refraction occurs at a tissue interface when there are different sound speeds of the two tissues and the wave incidence angle is not 90°. If an ultrasound wave travels from a soft tissue of speed v_1 to a soft tissue with a speed of v_2, the relationship between the angles of incidence $\theta_{incident}$ and refraction $\theta_{refracted}$ is given by Snell's law:

$$\frac{\theta_{incident}}{v_1} = \frac{\theta_{refracted}}{v_2}. \tag{1.4}$$

The variation in the speed of sound in soft tissues causes refraction and may resulted in incorrect positions of tissues in the B-mode images.

Scattering occurs when structures inside tissues are about the same size or smaller than the wavelength of ultrasound. Unlike specular reflection, scattering causes the sound beam to be reflected in several directions and this reduces the echo strength. The factors affecting the scattering properties include: the size and number of point scatterers per unit volume within a tissue, the shape and structures of scatters and the acoustic impedance differences at the scattering tissue interfaces. Energy lost due to scattering is small when it is compared to energy absorption[48, 49]. The backscattering of tissues is related to the presence of collagen structures, such as microvasculature and elastin fibers[49]. For example, collagen fibers produces stronger scattering than blood cells[50].

Scattering contributes to the local echogenicity of a tissue region; however, the destructive and constructive interference of ultrasound pulses with randomly distributed scatters can generate speckle that does not reflect the structure of the underlying tissues. Speckle patterns are random and they usually appear when the scatterers are smaller than the resolution of an ultrasound pulse. They reduce the contrast resolution and degrade the details of the image. They can be found in both RF data and B-mode images; the texture of the speckle patterns does not necessarily reflect the structure of the corresponding tissue.

Energy is absorbed and converted to heat when the sound wave propagates through tissue. The amount of energy absorbed is dependent on the relaxation phenomena of the translational and rotational vibration modes of the biological macromolecules [50]. For example, lung tissue consists of air sacs and has a very high attenuation, whereas degassed water has low attenuation.

Generally, the overall attenuation is due to both scattering and energy absorption. The overall energy lost is expressed by the attenuation coefficient (μ) which indicates the energy lost in decibels per centimeter of travel. It is generally assumed that the attenuation coefficient in human tissue is linearly proportional to ultrasound frequency except in blood (1.25dBcm^{-1}), bone(1.7dBcm^{-1}) or lungs(0.6dBcm^{-1}) [51, 52, 53]. Note that an increase in ultrasound frequency causes an increase in attenuation. Moreover, Goss *et al.* [52, 53] summarized the ultrasound properties of various mammalian tissues and showed that the acoustic property of the same type of tissue can vary due to many factors such as the temperature, location of the sample, homogeneity of tissue, experimental techniques and *in vitro* or *in vivo* experiments. For example, the attenuation of fat is 10-15% higher at the room temperature than at a temperature of 37^oC [52].

It can be seen that the interaction between ultrasound and tissue is complicated but trends and models exist. The interaction affects both amplitude and spectrum properties of the tissue due to the frequency dependence of the interaction. However, B-mode images, which are commonly used in traditional clinical analysis, are normally displayed after envelope detection so the spectrum content is lost. Spectrum properties can be an important description of soft tissues with different acoustic properties; therefore, spectrum properties of ultrasound RF signal will be discussed in the following section.

1.3.3 Backscattered Radiofrequency Spectra

The previous section describes how ultrasound waves propagate through soft tissues in terms of the tissue properties. This section describes the interaction based on the spectrum of RF data. A simplified model of the pulse-echo ultrasound interaction in the frequency domain at a particular location can be described as

$$R(f) = P(f)B(f)A(f) \tag{1.5}$$

where R(f) is the spectrum of the received echo and P(f) is the spectrum of a transmitted pulse. The interaction of the transmitted pulse and the soft tissues is characterized by the spectrum backscattering B(f) and spectrum of attenuation A(f) [54].

Assuming the transmitted pulse is Gaussian in shape, P(f) can be described as

$$P(f) = P_o e^{-\frac{(f-f_o)^2}{2\sigma^2}} \tag{1.6}$$

where P_o is amplitude constant, f_o is the transducer central frequency and σ is the bandwidth of the pulse spectrum. The backscattering spectrum can be modeled as

$$B(f) = B_o f^z \tag{1.7}$$

where z is the scatter power and ranges from 0 to 4, and most human tissue is within the range of $z = 1$ to 2 [49]. On the other hand, the attenuation spectrum can be modeled as

$$A(f) = A_o e^{-\alpha f} \tag{1.8}$$

if we assume attenuation in human tissue is a linear function of frequency and ultrasound attenuates exponentially [48]. α is the total accumulative round trip attenuation in tissue. The typical value of α in soft tissue is $0.5 dB(MHz cm)^{-1}$ [55] and this value varies among soft tissues. For example, striated muscle has a value of $1.30 dB(MHz cm)^{-1}$, fat tissue at $37°C$ has a value of $0.61 dB(MHz cm)^{-1}$ and blood has a value of $0.15 dB(MHz cm)^{-1}$ [52].

By combining Equations 1.6 to 1.8, the spectrum of the received echo R(f) becomes

$$R(f) = P_o B_o A_o e^{-\frac{(f-f_o)^2}{2\sigma^2}} e^{-\alpha f} f^z. \tag{1.9}$$

Therefore, R(f) can be expressed in proportion to f, f_o and z as:

$$R(f) \propto e^{\frac{-[f-(f_o-\alpha\sigma^2)]^2}{2\sigma^2}} f^z \tag{1.10}$$

.

According to the work of Treece *et al.* [54], f^z can be expressed as an exponential and the scaling factors that are not related to frequency f are dropped. As a result, R(f) can be simplified and expressed in terms of a received Gaussian pulse as:

$$R(f) \propto e^{-\frac{(f-f_c)^2}{2\overline{\sigma}^2}} \tag{1.11}$$

where

$$\overline{\sigma} = \sigma^2 \frac{f_o^2}{f_o^2 + z\sigma^2} \tag{1.12}$$

and

$$f_c = f_o - \alpha\overline{\sigma}^2 + \frac{z\overline{\sigma}^2}{f_o}. \tag{1.13}$$

$\overline{\sigma}$ and f_c are the bandwidth and central frequency of the received pulse R(f) respectively.

From equation 1.13, it is noticed that the central frequency f_c of the received pulse spectrum shifts down as the round trip attenuation α increases. α increases when the travelling depth of the pulse increases; therefore, f_c decreases as the depth increases. If z changes abruptly from one tissue to another tissue, there will be an abrupt change in the center frequency f_c and a reduction of the bandwidth $\overline{\sigma}$.

Moreover, Fink *et al.* [56] used the short time Fourier transform (STFT) analysis and showed that the downshifting rate of f_c is proportional to the attenuation α as

$$\frac{df_c}{dy} = c\alpha\overline{\sigma}^2(y) \tag{1.14}$$

where c is the speed of sound in soft tissue, $\overline{\sigma}^2(y)$ is the bandwidth of the received spectrum that changes with depth (y) and $\frac{df_c}{dy}$ is rate of change of f_c.

The above equations have shown that soft tissues with different acoustic properties would have different influences on the central frequency and bandwidth of the received echo spectrum.

1.3.4 Current Development of Ultrasound Segmentation

Most research in ultrasound segmentation is concentrated on B-mode images. For instance, Akgul *et al.* [57] used a deformable contour to detect the tongue boundary in B-mode images. An automatic fuzzy multi-resolution-based algorithm was developed for cardiac left ventricular epicardial and endocardial boundary detection [58]. Madahushi and Metaxax [59] automatically found lesion margins in ultrasound images by using both empirical domain knowledge used by radiologist and low level image features. Low level image features include texture, intensity and directional gradients. These are just a few examples of a large body of literature. However as mentioned, B-mode images are formed after envelope detection of RF signals, so spectral information that describes the properties of soft tissue is lost.

Not until recently have researchers started to investigate boundary detection using RF signals. In 1999, Hammoude [60] first attempted to detect edges based on abrupt changes in the central frequency due to the attenuation rate. However, his method failed to correctly identify the boundary due to erratic changes in ultrasound signal. Boukerroui at al [61] investigated a 3-dimensional adaptive clustering segmentation method for *in vivo* echocardiographic 3D data based on gray-scale intensity, two-dimensional texture features calculated envelope data and the local mean frequency of the spectrum. In 2003, Dydenko *et al.* extracted the power of the signal, spectral-based autoregressive parameters, and a velocity-based parameter to detect boundaries in echocardiographic images by an adaptive smoothing algorithm. They also obtained promising results from performing boundary detection in cardiac sequences *in vivo* using the variance of velocity [62]. Davignon *et al.* used the integrated backscatter and mean central frequency to improve their multi-resolution

Bayesian region-based algorithm that was based on envelope data. Their algorithm was tested on agar-gel phantom and proved that a multiparameteric approach could improve the segmentation result [63]. These examples show that it is feasible to use spectrum information of the RF signals for the purpose of segmentation.

1.4 Properties of Human Subcutaneous Fat

The properties of human subcutaneous fat are presented from the biological and the ultrasound viewpoints. The potential difficulties in detecting the fat layer in B-mode ultrasound images are discussed.

1.4.1 Biological characteristics

Fat, which is also known as adipose tissue, is a layer of loose connective tissue specialized in storing lipids. Fat cells are held together by thin fibrous membranes of connective tissue. Connective tissue in fat usually appears as thin and relatively sparse collagen fibers. Fat cells found in humans (mostly white adipose tissue) are also known as adipocytes and consist mainly of lipids (80% of a fat cell) and can range up to 120μ in diameter [64]. They are spherical in shape when isolated. However, fat cells are usually packed to form a meshwork and become polyhedrical in shape. The number of fat cells increases mainly during our infancy. An adult gains weight mainly because of an increased accumulation of lipids in fat cells and not an increase in the number of fat cells [64].

In the human body, fat can be divided into two types: subcutaneous fat and visceral fat. The subcutaneous fat layer is immediately underneath the skin and usually found in the thigh, waist, abdomen and buttocks. Visceral fat is usually located internally, around kidneys, at mesentery and retroperitoneal spaces etc [65]. However, in this thesis, we are mainly interested in the subcutaneous fat layer.

1.4.2 Ultrasound characteristics

As mentioned before, fat tissue consists mainly of lipids with sparse connective tissues. In ultrasound B-mode image (as shown in Figure 1.1), human subcutaneous fat is separated from the next soft tissue layer (usually the muscle) by a continuous white layer called fascia. This layer

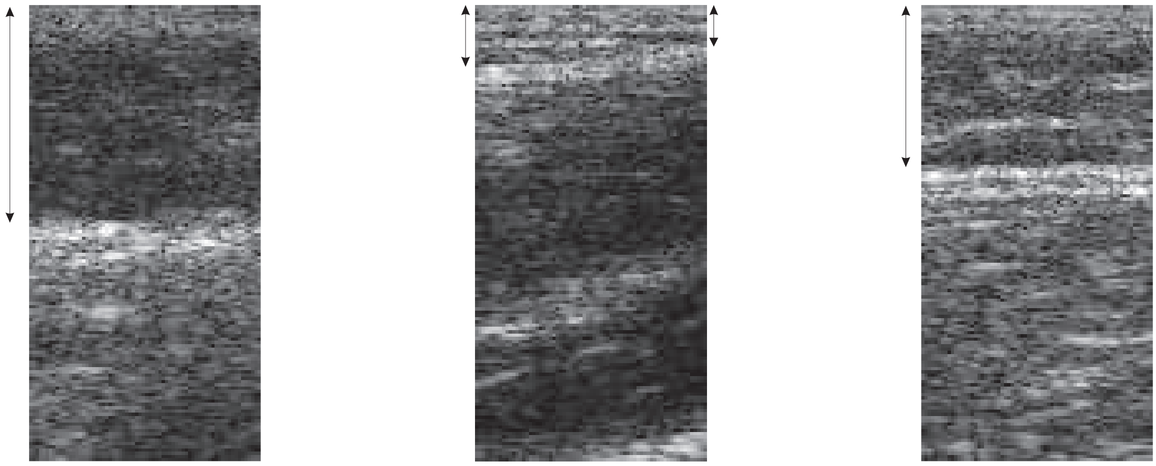

(a) suprailiac (b) triceps (c) thigh

Figure 1.5: B-mode images showing subcutaneous fat at different body sites. The thickness of the fat layer is indicated with arrows.

usually generates a strong reflection of the ultrasound pulse and is referred to as the fat boundary. Connective tissues are also dispersed within the fat tissue.

Figures 1.5(a) to 1.5(c) show the appearance of the subcutaneous fat layer in B-mode images. In this study, when we refer to the subcutaneous fat layer, it starts with, and includes, the dermis of the skin, and ends at the continuous white layer which is the fascia. When the layer of subcutaneous fat is homogeneous, it usually appears to be less echogenic than other tissue layers such as muscles (Figure 1.5(a)). In addition, fibrous membranes of connective tissue, whose length, thickness and density vary between people and body sites, can be found within the layer of fat. As a result, the layer of subcutaneous fat appears to be more echogenic in the presence of thicker connective tissue (Figures 1.5(b) and 1.5(c)). From our images, we noticed that subcutaneous fat at the suprailiac site (figure 1.5(a)) is usually more homogeneous (with less or thinner connective tissue) than at the triceps and thigh. At the triceps and thigh (Figure 1.5(b) and 1.5(c)), the layer of fat usually consists of longer, thicker and denser connective tissues.

Researchers have conducted studies to investigate the acoustic properties of human fat. Summaries from [52, 53] show that fat has a relatively low speed of sound ($\sim$1480ms^{-1}) compared with other human soft tissue, while connective tissue (~1613ms^{-1}) has a relatively high speed of sound. Therefore, fat tissue is highly heterogeneous and may cause ultrasonic wavefront distortion [66].

Moreover, previous research has also shown that different types of fat tissues have dissimilar acoustic properties. For example, Greenleaf and Bahin [67] investigated fat in the breast using transmissive ultrasound computerized tomography and found that an increase in the number of collagen in fat content would increase its speed of sound and its attenuation. Landini and Sarnelli [68] also found that the attenuation coefficient is lower for tissues with a large predominance of fat cells and this increases with more collagen fiber content.

The usual practice of a sonographer in determining the subcutaneous fat thickness is to draw a vertical line from the surface of skin to the fascia [13]. There are several factors affecting the visual interpretation of the fat boundary. For example, dense connective tissues may appear near the fascia and make the fat-muscle boundary less clear, and a long connective tissue layer may also be wrongly interpreted as the fascia. Moreover, it is harder to define the boundary between subcutaneous fat and muscle because of the smaller amounts of intermuscular fat tissues[13].

Although the fascia and fibrous connective tissues are well imaged because of their specular characteristics, the amplitude of the received pulse can be affected by the angle of incidence of the ultrasound beam. In our images, the transducer was kept vertical to the skin so that the angle of incidence was near 90°.

1.4.3 Difficulties in Segmentation of Fat in Ultrasound Images

From the observations in the previous section, we noticed that the variations in echogenicity, size and density of connective tissue among different people and body sites make it difficult to extract the fat layer from B-mode images alone. Several authors have also reported that heterogeneity of subcutaneous adipose tissue was observed in ultrasound and X-rays images [31, 32]. Additional strong interfaces could appear near skin and intermediate membranes dispersed through the fat tissues. Other researchers also show that the thickness and texture of fat affects the overall appearance of B-mode images. Haberkorn *et al.* [69] investigated the influence of the subcutaneous fat layer on the diagnosis of B-mode images. They mentioned that the size of fat clusters might change the ultrasound wave length, and showed that an increase in thickness of fat caused darker and lower contrast images. Pomaroli *et al.* [70] performed a histologic analysis and showed that fatty tissues with more connective tissues appeared to be more echogenic in B-mode than fatty tissues with fewer connective tissues. Moreover, Hinkelman *et al.* [66] also mentioned that thick layers of fat may cause poor B-mode image quality at the abdominal wall because they distort ultrasound beams due to their scattering and absorption effects.

1.5 Thesis Objectives and Organization

Conventional B-mode ultrasound images describe tissue structure only in terms of echogenicity and texture. Based on our observed difficulties, fat tissue does not have a consistent description of both texture and brightness; therefore, image segmentation of subcutaneous fat is difficult when applied to B-mode images. Conversely, RF signals retain the frequency, phase and amplitude information. Spectrum properties of the RF signal give additional information related to the acoustic properties of fat; thus, we will investigate the feasibility of measuring the subcutaneous fat by detecting the changes of the spectrum from one layer to another. Moreover, the existence of speckle also affects the texture of ultrasound images. Ultrasound speckle adds noise to the RF raw data, reduces the contrast resolution and weakens the detectability of soft tissue layers. Therefore, the existence of speckle also imposes further challenges on the segmentation problem.

This thesis explores the use of the spectrum properties of RF signals to detect the boundary of the subcutaneous fat layer and presents an image processing and boundary detection framework to automatically detect the fat boundary *in vivo*. An experiment with nine human subjects is also presented to validate the accuracy of the method by comparing our automatic measurements with manual measurements. Furthermore, the correlation between ultrasound measurements and skinfold measurements is also investigated. The thesis is organized into four chapters as follows:

Chapter 2 describes our method of image processing and boundary detection using the RF signals. The calculation of spectrum properties is presented and spatial compounding is introduced to reduce the noisy spectrum measurements. The values of the spectrum properties are encoded as gray-scale parametric images for segmentation. A new segmentation technique on selected spectrum properties using thresholding and boundary detection is also discussed. At the end, capturing RF data from multiple focuses is proposed to overcome the drawbacks of using a single focus.

Chapter 3 shows the overview of the entire human subcutaneous fat detection framework.

The steps of the detection framework include RF data capture, calculation of spectrum properties, preprocessing of spectrum properties map and segmentation. Moreover, our method is tested at the suprailiac, triceps and thigh sites of nine volunteers and is compared to the skinfold caliper method. The procedures of the user study in collecting skinfold caliper measurements and ultrasound data are discussed.

Chapter 4 evaluates the results of our fat boundary detection method. First, our results are compared with the manual detection on B-mode images in terms of average thickness error and RMS error. We also investigate whether data obtained from multiple focuses will improve the robustness of our detection algorithm. Furthermore, relationships between skinfold caliper and ultrasound measurements are presented in terms of their linear correlation and mean differences.

Chapter 5 summarizes our work and presents the future work. It also describes the remaining issues of our detection method using ultrasound.

Chapter 2

Method in Developing Image Processing and Boundary Detection

In the previous chapter, we have shown that the acoustic properties of soft tissues can be related to the spectrum of the received radiofrequency (RF) signal. This chapter proposes the use of unprocessed RF signals to develop an image processing and boundary detection algorithm to extract the human subcutaneous fat layer. We discover that the characteristics of human subcutaneous fat tissues can be described by the local spectrum properties of RF signals. The spectrum properties are encoded into gray-intensity images called parametric images. Then, we develop an image processing and boundary detection method based on our observations on the parametric images. Moreover, we discover that the method of spatial compounding increases the signal to noise ratio and improves the detection of subcutaneous fat from their parametric images of the spectrum properties. With the spectrum properties established through spatial compounding, a thresholding and boundary detection method is proposed to segment the subcutaneous fat layer and locate the fascia - the fat boundary. Finally, we also consider using spectrum properties obtained from multiple focuses to improve the segmentation result.

2.1 Processing of Radiofrequency Signal

RF signals are stochastic (i.e. next state of the signal is partly but not fully determined by the previous state of the signal) and their spectrum characteristics vary with time; therefore, their spectrum properties are estimated by local spectrum calculations. In each RF signal, local spectra are calculated by short time Fourier transform (STFT). The total energy, mean central frequency and spectrum variance are calculated for each local spectrum and their relationship with the subcutaneous fat layer is investigated.

The reasons for using these three spectrum properties are as follows:

- The total energy reflects the strength of echoes. Since echoes reflected from the fascia are relatively strong, the total energy can indicate the location of the fascia.
- The mean central frequency shifts downward with depth when the pulse propagates. Its rate of change is proportional to the attenuation coefficient of the soft tissue and can potentially serve as a descriptor of soft tissues with different acoustic properties.
- The spectrum variance provides the deviation of spectrum values from f_c. It gives the uncertainty measurement for the estimation of the mean central frequency. It can potentially describe the shape and bandwidth of the power spectrum which vary among different soft tissues.

2.1.1 Calculation of Spectrum Properties

STFT is performed on each RF scan line. A window, which consists of 32 samples, is shifted down in depth with a 50% overlapping of the previous window. Then, a Hamming window and discrete Fourier transform (DFT) are applied to the window. M-point DFT is performed by Matlab's **fft** function. The spectrum is obtained by:

$$S(w) = |X(w) * X(w)| \tag{2.1}$$

$$w \in \{0, f_o, 2f_o, ...(M-1)f_o\}$$

where f_o is the sampling frequency of RF signals, $X(w)$ is the DFT applied to a windowed RF signal x(t) and $S(w)$ is the power spectrum with a length of M/2. As mentioned in Section 1.3.3, the spectrum is assumed to have a Gaussian distribution.

The three spectrum properties (total energy, mean central frequency and spectrum variance) of $S(w)$ are calculated within a bandwidth W but not the whole spectrum. The purpose is to eliminate unwanted frequencies that are considered to be non-significant data. We use W from 0.5MHz to 11MHz for data obtained from a 6.6MHz transducer. Since the transmission frequency of the transducer is 6.6MHz and its bandwidth is small, it is reasonable to restrict the signal to this range. A rule of thumb for the axial resolution of a 6.6MHz transducer is 0.35mm[1]. The window size of 32 samples, which corresponds to 0.62mm, is around twice the axial resolution of the transducer.

The first spectrum property discussed is the total energy of the spectrum, also referred to as the integrated backscatter coefficient (IBS)[71, 63]. The IBS coefficient indicates the total reflected power and strength of the backscattering; a larger value corresponds to more energy reflected from the tissues. The IBS is calculated by:

$$IBS = \sum_{w=W_{min}}^{W_{max}} S(w) \tag{2.2}$$

where w is from W_{min} to W_{max} MHz, $S(w)$ is the power spectrum with a length of $M/2$.

The mean central frequency (f_c) describes the spectrum central frequency which is the average of the frequencies present in a window. Section 1.3.3 show that the rate of change of f_c is directly proportional to the attenuation and its value fluctuates when the ultrasound pulse propagates through tissue and is reflected by tissues with different acoustic properties. f_c can be calculated using the moment analysis. Moment analysis has been used by several authors [56, 63] to calculate local spectrum properties of RF signals. Fink *et al.* [56] proved that the moment analysis can be used calculate the central frequency and variance of the power spectrum. In moment analysis, the jth moment m_j is calculated as the following:

$$m_j = \sum_{w=W_{min}}^{W_{max}} w^j S(w) \tag{2.3}$$

where $S(w)$ is the amplitude of the spectrum and w^j is the jth power of w. By using Equation (2.3), f_c is expressed by the zeroth moment(m_0) and first moment (m_1) of the spectrum [56] as

$$f_c = \frac{m_1}{m_0} \tag{2.4}$$

The last spectrum property is the spectrum variance(σ_s^2). It tells the deviation of spectrum values from f_c within a bandwidth W; a larger value corresponds to a higher uncertainty for the

---

[1] The axial resolution (for a three cycle pulse) = (temporal pulse length x 3) x $c/2$ = (c x 3)/(f_o x 2)

estimation of f_c. To our knowledge, this spectrum property is rarely used in investigating tissue properties in ultrasound. Bylund at al [73] discovered that the estimated spectrum variance was low at the reverberation artifact locations[74]. According to Fink *et al.* [56] σ_s^2 can be calculated using the first and second moment(m_2) of the spectrum and f_c given by:

$$\sigma_s^2 = \frac{m_2}{m_0} - f_c^2. \tag{2.5}$$

The calculation of σ_s^2, as proved by Fink *et al.* [56], is shown in Appendix A.

2.1.2 Noise Reduction using Spatial Compounding

Statistical fluctuations exist in backscattered RF signals due to speckle noise and heterogeneity in tissues and result in noisy spectrum properties. Spatial compounding has been used to reduce speckle and improve boundary continuity in B-mode images [75, 76, 77]. Recently, compound imaging is also applied to reduce the variance of displacement estimations in elastography [78], to improve temperature estimations due to the thermo-acoustic lens effect in high intensity focused ultrasound [79] and to reduce variance of attenuation measurements and enable coarse attenuation imaging [80]. In our work, compound imaging is used to improve the estimations of IBS, f_c and σ_s^2.

The concept of spatial compounding is shown in Figure 2.1 for B-mode images. The object (gray circle) appears inhomogeneous in the presence of speckle and the speckle pattern changes under different viewing angles. The two beam-steered B-mode images at left and right (not taken from the 0° direction), are transformed and interpolated from the raw data coordinates to Cartesian spatial coordinates. The raw data coordinates are with respect to the transducer and the spatial coordinates are in the real space. In the end, the resulting images in their spatial coordinates are averaged to form a single compounded image. Since speckle patterns are random, their shape and distribution changes with beam angle, so averaging images from different views can reduce speckle and the object appears more homogeneous. Our idea of applying spatial compounding to the spectrum properties is similar to the above discussion except spatial compounding is applied to obtain the spectrum properties values (IBS, f_c and σ_s^2) instead of the B-mode pixel values. The details of implementation will be discussed next.

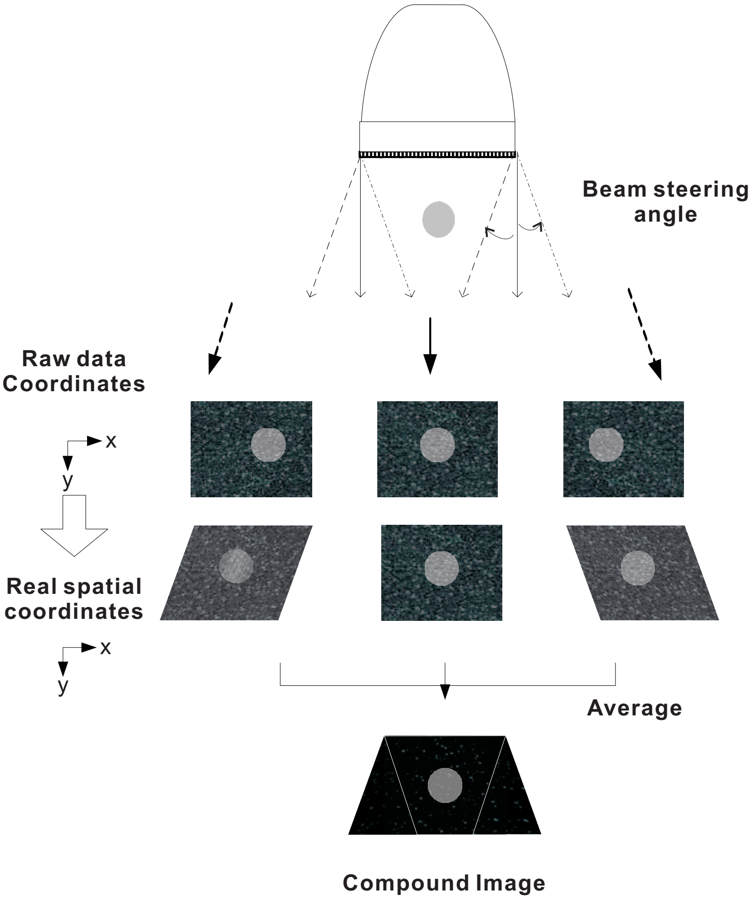

Figure 2.1: The concept of spatial compounding for reducing speckle in B-mode images. After averaging images taken from different angles, speckle patterns are reduced and the object appears more homogeneous.

2.1.2.1 Implementation

Spatial compounding is applied to each spectrum property as shown in Figure 2.2. RF data are first obtained from N different steering angles by beam steering of the transducer. For each steering angle θ, a spectrum property (IBS or f_c or σ_s^2) is calculated from each RF scan line as described in section 2.1.1. As a result, N two-dimensional spectrum properties , whose width is the number of RF scan lines and height is the number of STFT windows, are computed for each spectrum property. The values of f_c, σ_s^2 and IBS may be presented as two-dimensional images. We will refer to these two-dimensional images of the spectrum properties as "parametric images" throughout the thesis.

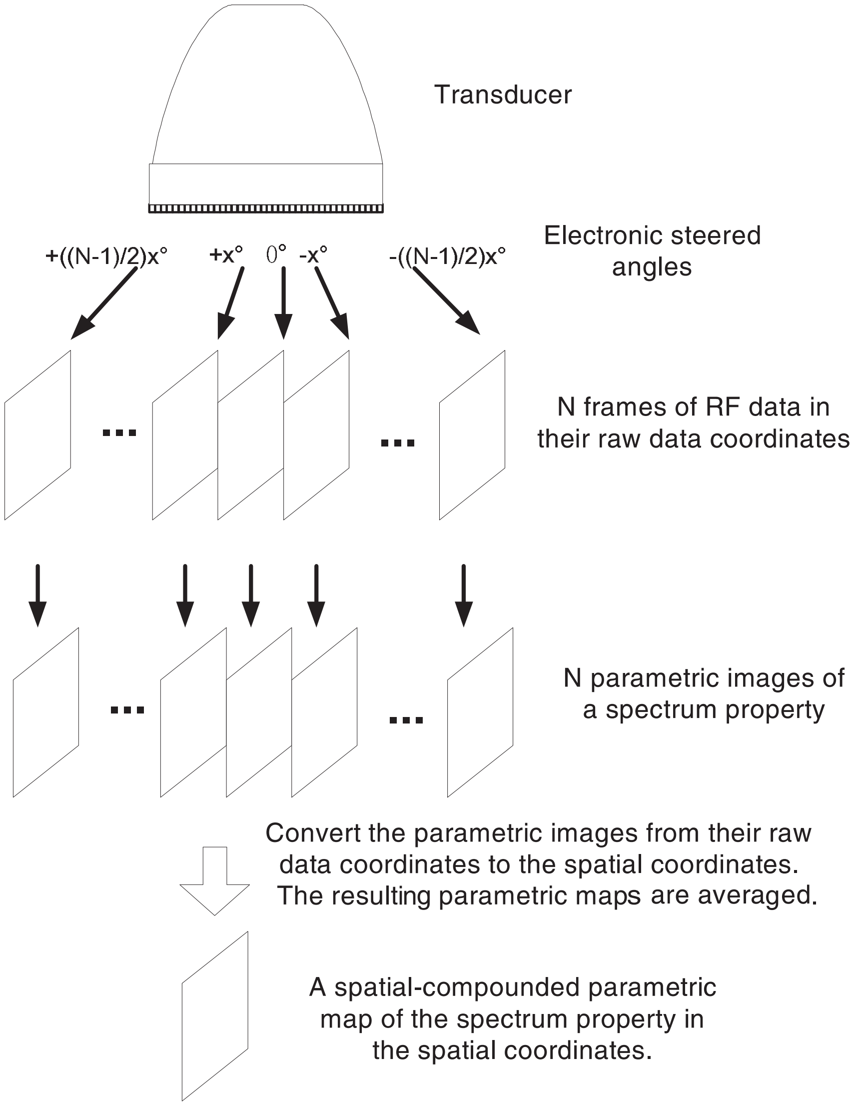

Figure 2.2: Application of spatial compounding on a spectrum property.

The next step is to convert a parametric image from its raw data coordinates to the real spatial coordinates using the geometry of the steering (Figure 2.3).

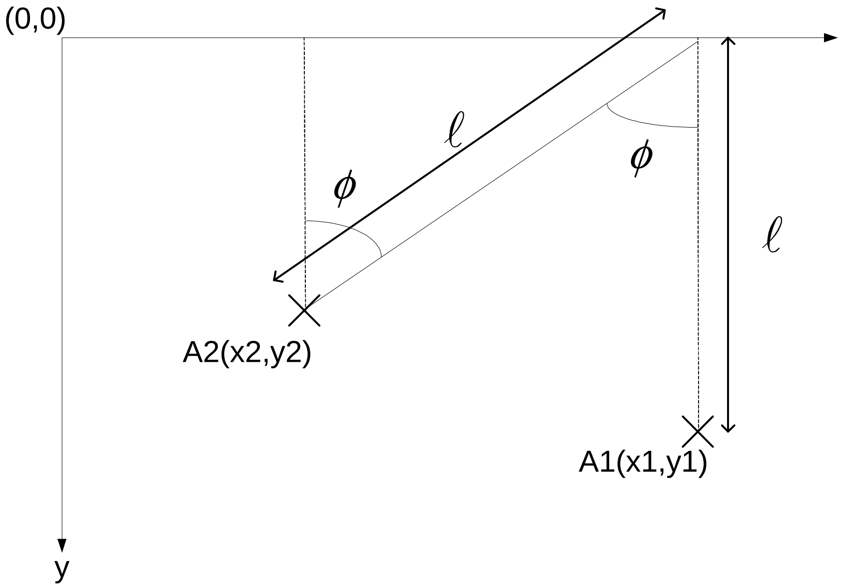

Figure 2.3: Mapping the coordinates from the raw data space to the real space by geometry. A_1 is a spectrum property value at its raw data coordinates (x_1, y_1) in the parametric image obtained from the steering angle θ. A_2 is the corresponding spectrum property value of A_1 at the real spatial coordinates (x_2, y_2).

Let A_1 be a spectrum property value at the raw data coordinates (x_1, y_1) in the parametric image obtained from the steering angle θ and A_2 be the corresponding spectrum property value of A_1 at the real spatial coordinates (x_2, y_2). Using geometry (Figure 2.3), (x_2, y_2) can be calculated as:

$$\phi = -\theta$$

$$\ell = y_1$$

$$\frac{x_1 - x_2}{\ell} = sin\phi$$

$$x_2 = x_1 - \ell sin\phi \tag{2.6}$$

$$\frac{y_2}{\ell} = cos\phi$$

$$y_2 = \ell cos\phi \tag{2.7}$$

Thereafter, a two-dimensional bilinear interpolation is applied to find the interpolated spectrum property value $A_2(x_2, y_2)$ in the real spatial coordinates space. The Matlab function **interp2** is used for the the bilinear interpolation based on the known original raw data coordinates, real spatial coordinates and values of the parametric image in the raw data coordinates space.

2.1.2.2 Experiments

A custom-made phantom is used to find the best range and step size of steering angles for spatial compounding by calculating the uncertainty in estimating the rate of change of f_c. Moreover, the spatial compounding method is compared to neighbour averaging to show that the reduction of speckle noise in spectrum properties is more effective when averaging from different viewing angles instead of simply from neighbouring data. The best range and step size of steering angles obtained from the phantom experiment are then used for observing the qualitative improvements on the parametric images of IBS, f_c and σ_s^2 in real human tissue.

2.1.2.2.1 Phantom Experiments Given a phantom that is homogeneous and composed of only one type of tissue with a constant attenuation rate, the rate ($\frac{df_c}{dy}$) of down-shifting f_c along the depth (y) direction is then linearly proportional to its attenuation rate. Since the value of f_c vs y is erratic, we can characterize the change of f_c for each RF scan line by linear regression as shown in Figure 2.4. ($\frac{df_c}{dy}$) is then the slope of the linear regression line. The standard deviation of slope values among all scan lines indicates the uncertainty in estimating $\frac{df_c}{dy}$ of a homogeneous layer. If the standard deviation is small, there is less statistical fluctuation of the spectrum value. We used a homogeneous phantom to investigate the improvement in the standard deviation by using spatial compounding and contrast the advantage of using spatial compounding over averaging with neighbouring values.

2.1.2.2.1.1 Method A homogeneous phantom was constructed by agar and cellulose - agar controls the stiffness of the phantom while cellulose controls the scattering. The phantom consists of 1% cellulose, 3% agar and 96% water. The transducer was mounted on a stand and stabilized with a clip during the experiment. We collected 127 scan lines of RF data from the phantom. RF data are used to compute f_c by the method described in the Section 2.1.1 and are spatially compounded in accordance with the Section 2.1.2.1.

The above procedure was tested with step size angles of 0.5°, 1°, 2.0° and 3.0°. In the region of interest, the linear regression fitting was applied at each scan line to compute the slope $\frac{df_c}{dy}$. The standard deviation of $\frac{df_c}{dy}$ between scan lines was calculated.

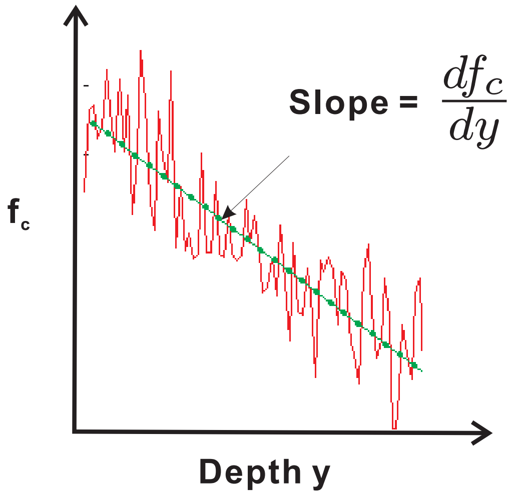

Figure 2.4: The slope $\frac{df_c}{dy}$ of the linear regression line is proportional to the attenuation rate of a specific phantom layer. The red line is f_c and the green dot line is the linear regression line of f_c.

In the alternative method of neighbour averaging, values of f_c are averaged with values from neighbour scan lines. A set of f_c values along a scan line is averaged with values from n scanlines (from both left and right neighbouring lines).The slope $\frac{df_c}{dy}$ can again be computed for each scan line of f_c. The standard deviation of $\frac{df_c}{dy}$ between scan lines is also calculated.

2.1.2.2.1.2 Results and Discussions Figure 2.5 shows the normalized standard deviation of the regression line slope $\frac{df_c}{dy}$ versus the number of angles N used for a given angle step size ϕ. The standard deviation is normalized to that obtained without spatial compounding or neighbor averaging. Figure 2.5 shows that spatial compounding helps to reduce the uncertainty in measurements. For a particular angle step size ϕ, the standard deviation decreases when the number of angles N used in spatial compounding increases. This indicates that greater numbers of frames increases the signal to noise ratio. In addition, more improvement is noticed when using a step size of 2.0° and 3.0° than 0.5°. It is because a larger separation of angle produces greater independence of the RF lines, so more speckle is reduced by averaging.

Spatial compounding shows a more convincing improvement in reducing noise in spectrum properties than neighbour averaging. Figure 2.6 shows the normalized standard deviation of regression line's slope versus the number of neigbouring scan lines used for averaging spectrum parameter values. The standard deviation is normalized by the value without neighbour averaging. The result shows that neighbour averaging does not produce a significant decrease in the standard deviation as the number of neighbouring lines increases and it does not improve the standard deviation to less than 0.9. Therefore, neighbour averaging does not improve the signal to noise ratio as much as spatial compounding because the data come from neighbouring lines are more correlated than data from different angles.

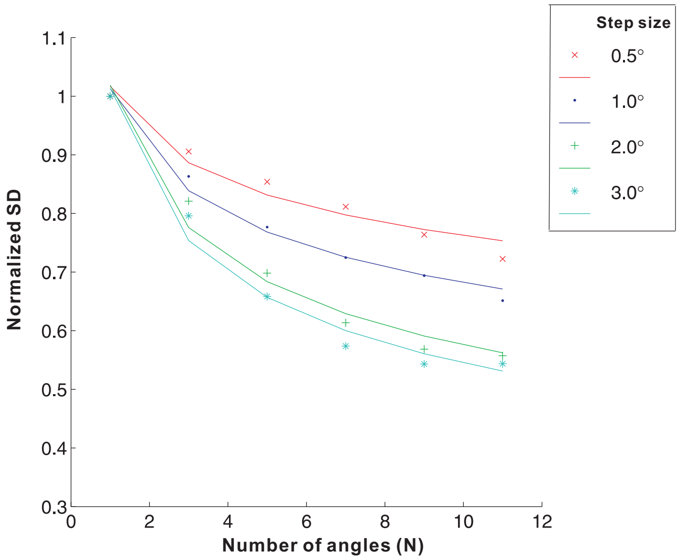

Figure 2.5: Reduction of the standard deviation in estimating the slope m of an f_c scan line using spatial compounding with different step sizes of steering angle θ and different numbers of angles. The data points are fitted by the function $\frac{1}{x}$.

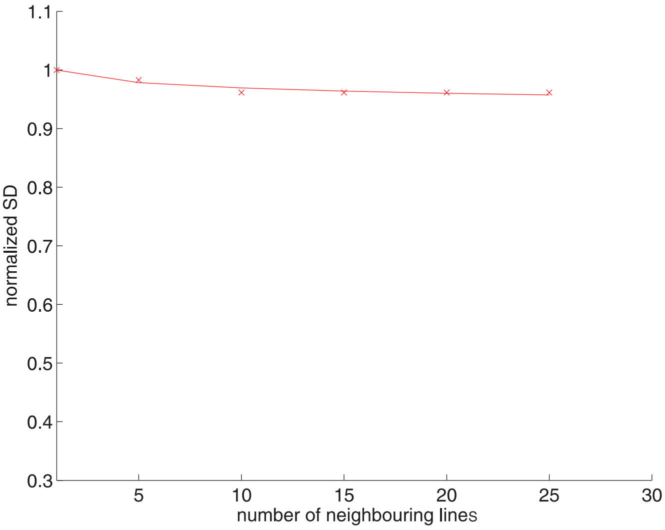

Figure 2.6: Improvement in the standard deviation of estimating the slope m of the f_c scan line using neighbour averaging with varying number of neighbour scan lines.

Nevertheless, there are tradeoffs of using spatial compounding. The increase of the range of angles improves the overall compounding effect, but the area covered by full compounding reduces as depth increases. We want to perform segmentation on a parametric image with every pixel compounded with the same number of angles; therefore, we want to choose a step size angle ϕ and a number of angles N that covers a fair amount of area and has a substantial noise reduction effect. According to our experiments, a combination of $N = 11$ and $\phi = 2°$ is best. For $\phi = 2°$, the compounding effect is similar to that of $N = 9$ and $\phi = 3°$. The former combination requires an angle range of ($\pm 10°$) and latter combination requires a larger range of angles ($\pm 12°$). In addition, if the steering angle is too large, the probability of echoes returned from tissue to the transducer becomes lower. Based on the above reasons, we used $N = 11$ and $\phi = 2°$ ($0°$,$\pm 2°$,$\pm 4°$,$\pm 6°$,$\pm 8°$ and $\pm 10°$) for our experiments with human *in vivo*.

2.1.2.2.2 Human Experiments

2.1.2.2.2.1 Method From the experiments with the phantom, it was shown that spatial compounding could improve the signal to noise ratio of spectrum calculation and the steering angle combination of $0°$,$\pm 2°$,$\pm 4°$,$\pm 6°$,$\pm 8°$ and $\pm 10°$ was chosen. A similar set of calculations was performed on the suprailiac, thigh and triceps sites of a human subject *in vivo*. Parametric images shown in the following sections are cropped to show the area with the same number of compound frames N.

2.1.2.2.2.2 Results and Discussions Figures 2.7 to 2.9 show the normalized spectrum properties with and without spatial compounding. Obvious quality improvements are shown in the f_c, σ_s^2 and IBS parametric images as the number of compounding frames increases. The parametric images of f_c and σ_s^2 obtained from one angle (0°) are erratic. Lack of uniformity is especially observed at the triceps (Figure 2.8) and the thigh (Figure 2.9). At the above two sites, the subcutaneous fat is less homogeneous than at the suprailiac site (Figure 2.7). The estimation of the power spectrum is affected by speckle noise, but the spatial compounding reduces speckle noise in parametric images of f_c, σ_s^2 and IBS by averaging their values obtained from different angles. Values are smoother and less erratic after spatial compounding; the characteristics of fat is differentiated from other tissues after spatial compounding.

The parametric images of both f_c and σ_s^2 show that their values decrease when depth increases, and their values are relatively higher in the fat tissue than other tissues. The discontinuity of their values is also observed at the fat boundary. It is also observed that the structure of subcutaneous fat affects the appearance of f_c and σ_s^2. For example, the B-mode image of Figure 2.8 shows that the subcutaneous fat is less homogeneous in the triceps when compared to that of the suprailiac site(Figure 2.7). Dense fibrous membranes of connective tissue are also observed in the middle of the fat layer at the triceps. At regions near the connective tissue, there are sudden changes of values in f_c and σ_s^2. The fibrous membranes are the source of inhomogeneity in the fat tissue and the cause of abrupt changes in the spectrum.

IBS shows that strong interfaces happen at the fascia (the fat boundary) and fibrous membranes of connective tissue in the fat tissue. In addition, stronger interfaces also appear at the bone or tendon at the triceps and thigh. Parametric images of IBS show that these strong interfaces are more complete after spatial compounding. Since strong interfaces are mostly smooth and specular surfaces, viewing them at different angles increases the chance of achieving an incidence angle of 90° when reflection is maximum. As a result, their boundaries appear more continuous and complete in compound IBS parametric images.

In general, f_c, σ_s^2 and IBS do show characteristics of subcutaneous fat. As observed, the subcutaneous fat layers have relatively higher values of σ_s^2 and f_c than other tissues. However, higher contrast between the subcutaneous fat layer and non-fat tissue is noticed in the parametric images of σ_s^2 than in the parametric images of f_c; therefore σ_s^2 is more suitable and easier for segmentation. In addition, IBS shows valuable information about strong reflected interfaces that tells the locations of the fascia (i.e. the location of the fat boundary) and the thick fibrous connective tissue in the subcutaneous fat.

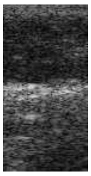

(a)

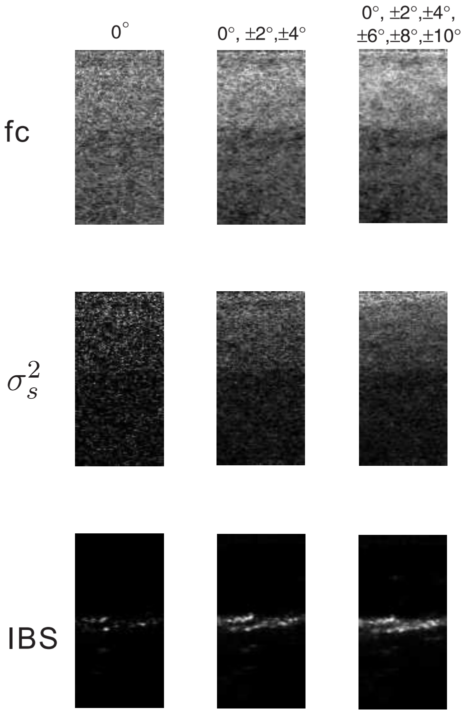

(b)

Figure 2.7: Improvement in spectrum properties at a human suprailiac site after using spatial compounding. (a) B-mode image. (b)Spectrum Properties(f_c, σ_s^2 and IBS). The left most column shows the spectrum properties without spatial compounding. The second and third columns show the compound spectrum properties using 5 and 11 angles of step size 2° respectively.

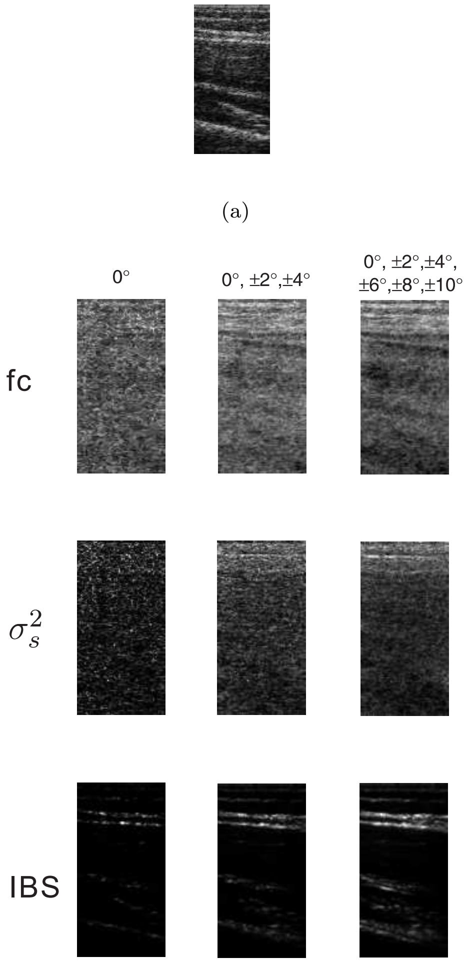

(a)

(b)

Figure 2.8: Improvement in spectrum properties at a human triceps after using spatial compounding. (a) B-mode image. (b)Spectrum Properties(f_c, σ_s^2 and IBS). The left most column shows the spectrum properties without spatial compounding. The second and third columns show the compound spectrum properties using 5 and 11 angles of step size 2° respectively.

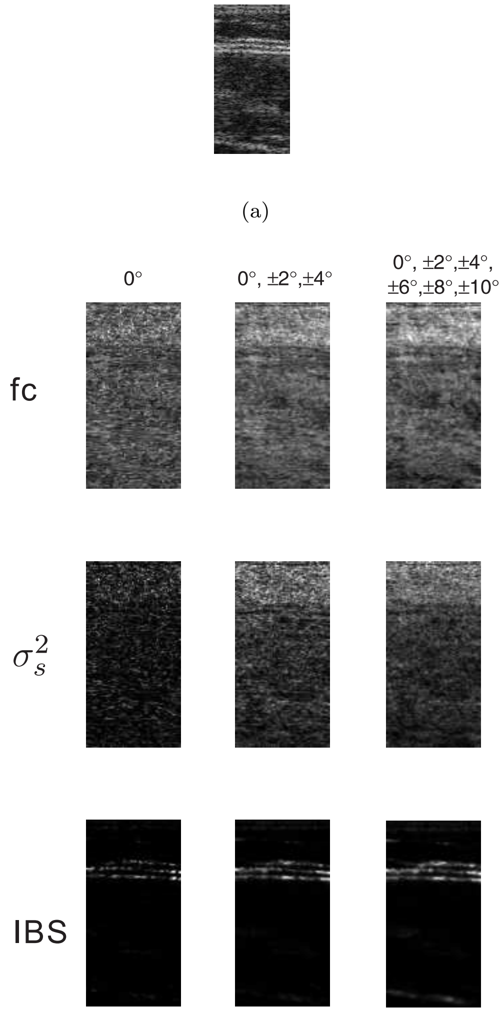

(a)

(b)

Figure 2.9: Improvement in spectrum properties at a human thigh after using spatial compounding. (a) B-mode image. (b)Spectrum Properties(f_c, σ_s^2 and IBS). The left most column shows the spectrum properties without spatial compounding. The second and third columns show the compound spectrum properties using 5 and 11 angles of step size 2° respectively.

2.2 Thresholding on Spectrum Properties

Based on the visual observation of compounded spectrum properties, thresholding is proposed to separate the subcutaneous fat layer and the non-fat layer. In a typical bilevel thresholding case, there should be two distinct modes in the parametric image histogram (i.e. a bimodal histograms); however, there can be cases when only one obvious peak or a very small second peak is found in the parametric image histogram. Classic thresholding algorithms like Otsu's method [81] assumes the histogram is bimodal and obtains the threshold by minimizing the within-group variance. For unimodal histograms, Rosin [82] developed a unimodal thresholding technique based on finding a corner in the histogram. His method can calculate a threshold in unimodal histograms and is not affected by the distribution of histogram. Good results have been shown in various thresholding tasks [82] and remote sensing image thresholding [83] using his thresholding method. In our thresholding task, we noticed that the intensity histogram of spectral parameters may be unimodal. Based on our assumptions of segmentation and observations, Rosin's thresholding method is used and will be discussed in this section.

2.2.1 Unimodal Thresholding

To use Rosin's thresholding method, assumptions are made on the parametric images of the spectrum properties:

1. The subcutaneous fat (with skin) is always the first top layer of tissue; therefore, it has a relatively higher value of f_c and σ_s than the values of the following layer if no noise is present.
2. In the parametric images of IBS, strongly reflective tissues such as the fascia and fibrous membranes of connective tissue in fat layers always has higher intensity values than poorly reflective tissues.
3. A main peak is always found in the intensity histogram and it is always much higher than the secondary peak (if any).

Rosin's thresholding is simple but assumes "here is one dominant population in the image that produces one main peak located at the lower end of the histogram relative to the secondary population."[82]. To locate the threshold in Figure 2.10, a straight line AB is drawn from the main peak A to point B which is the first empty bin of the histogram following the last filled bin. The threshold is located by finding the maximum perpendicular distance from straight line AB as shown in Figure 2.10(a). In addition, we also consider bimodal cases (Figure 2.10(b)) where histogram intensity values may be larger than line AB. Since the threshold is most likely located at a concavity, histogram values that are greater than AB are not considered. We use geometry to solve the threshold and the calculation is shown in Appendix C. Since the histogram appears noisy, it is smoothed by a 5-point Gaussian filter before finding the threshold by Rosin's method.

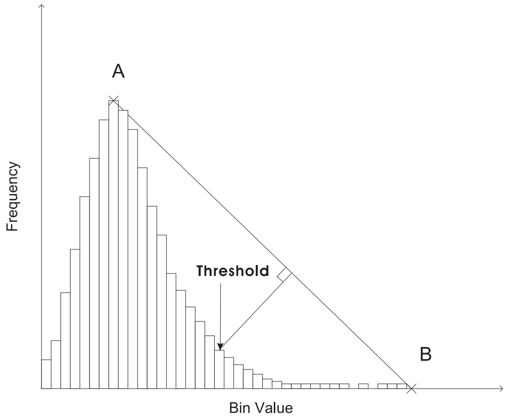

(a)

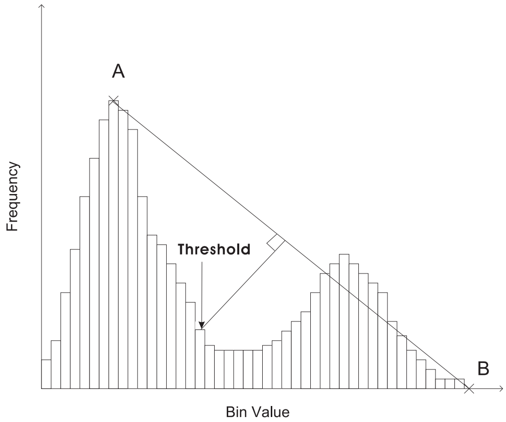

(b)

Figure 2.10: Detection of threshold using Rosin's thresholding method on (a) unimodal histogram and (b) bimodal histogram.

2.2.2 Thresholding results

Figures 2.11 to 2.13 show the thresholding results of f_c, σ_s^2 and IBS. The values of parametric images are normalized between 0 to 1. Higher gray intensity values of the histogram indicate brighter pixels in the parametric images.

Rosin's thresholding is not accurate in detecting the fat boundary in the histogram of f_c because of the poor contrast in the value of f_c. Although the boundary can be detected in f_c when the histogram of f_c is bimodal (Figure 2.11), the thresholding method fails to detect the fat boundary in Figure 2.13. In the histogram of f_c in Figure 2.13, the main peak is wide and not obvious. As observed in the B-mode image, the value of f_c appears to be disrupted by the connective tissue within the fat tissue and the resulting parametric image of f_c has a poor contrast. Based on our observations on the fat tissues with different structures, the parametric image of σ_s^2 has a better contrast than that of f_c and is more suitable for the thresholding technique.

The histogram of σ_s^2 shows that the gray intensity pixel values of the fat tissue change more rapidly than that of the non-fat tissue. In the histogram of σ_s^2, the left side of the vertical threshold line are pixels that belong to the non-fat tissue and the right side of the vertical threshold line are pixels that belong to the fat tissue. The pixels in the fat region (which are brighter in the gray intensity) have a wider range of gray intensity values than that of the non-fat region (which are darker in the gray intensity). The pixels from the non-fat region make up a main peak in the histogram and the pixels from the fat region make up a tail in the histogram. The main peak corresponds to a slow change in pixel values and the long tail corresponds to a fast change in pixel values. The above condition satisfies the assumptions of the Rosin's thresholding method and the Rosin's thresholding method is able to detect the change from the fat tissue to the non-fat tissue from σ_s^2.

We suggest that a relatively rapid change in the pixel values of σ_s^2 at the subcutaneous fat layer than its other tissue layers is observed because the fat tissue constitutes two very different components: the fat cells and connective tissue. We discussed the structure of the subcutaneous fat in Chapter 1 and showed that the fat cells in the subcutaneous fat layer are held by connective tissue. The large-scale variation in speed of sound between fat and connective tissue ($\sim$1480ms^{-1} vs $\sim$1631ms^{-1}) imposes more fluctuations in the power spectrum and can distort the ultrasound wavefront. As suggested by Hinkelman at el. [66], the subcutaneous fat has greater energy level and waveform distortion than muscle when they investigated the effect of abdominal wall morphology on ultrasonic pulse distortion. Therefore, we imply that the high variation in the tissue structure of subcutaneous fat causes more fluctuations in the received spectrum, and this results in a greater change in the spectrum variance.

Moreover, the thresholding method is able to locate strongly reflective interfaces from the IBS (right most column of figures 2.11 to 2.13). Not only is the fascia located in the binary map of IBS, structures with strong echoes are also located in the middle of the binary map of triceps and thigh (Figure 2.12 and 2.13). The effects of thresholding will be discussed further in Chapter 4 in the concept of the full system.

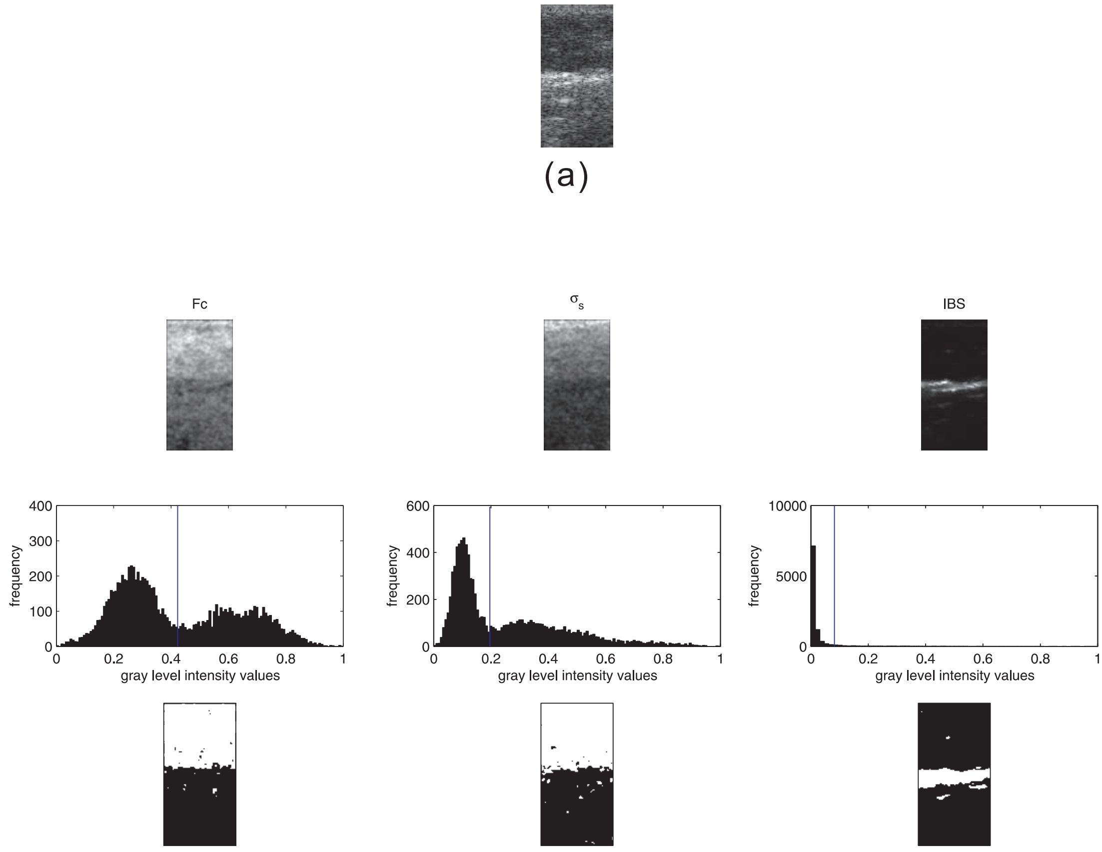

(a)

(b)

Figure 2.11: Results of thresholding on spectrum properties captured at the human suprailiac site. (a) B-mode image. (b) Spectrum properties' images(1^{st} row), their histograms (2^{nd} row) and binary maps (3^{rd} row). The vertical line in the histogram indicates the calculated threshold.

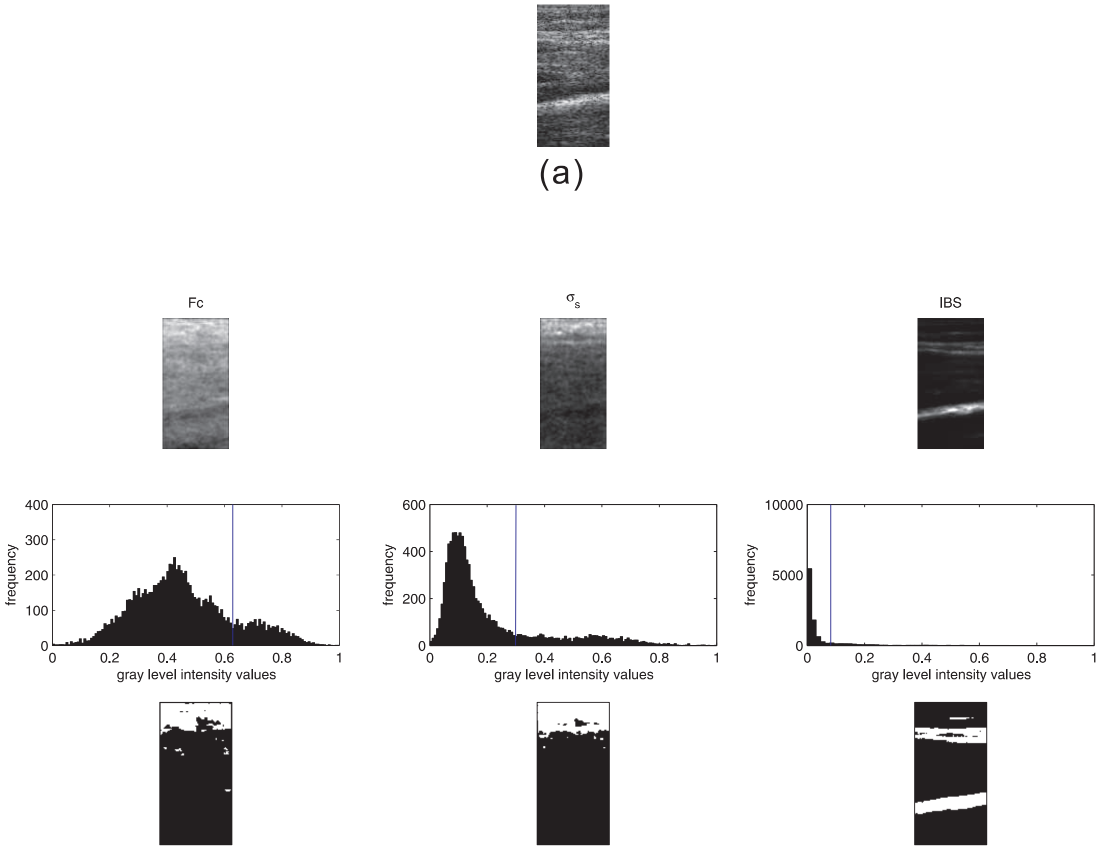

(a)

(b)

Figure 2.12: Results of thresholding on spectrum properties captured at the human triceps site. (a) B-mode image. (b) Spectrum properties' images(1^{st} row), their histograms (2^{nd} row) and binary maps (3^{rd} row). The vertical line in the histogram indicates the calculated threshold.

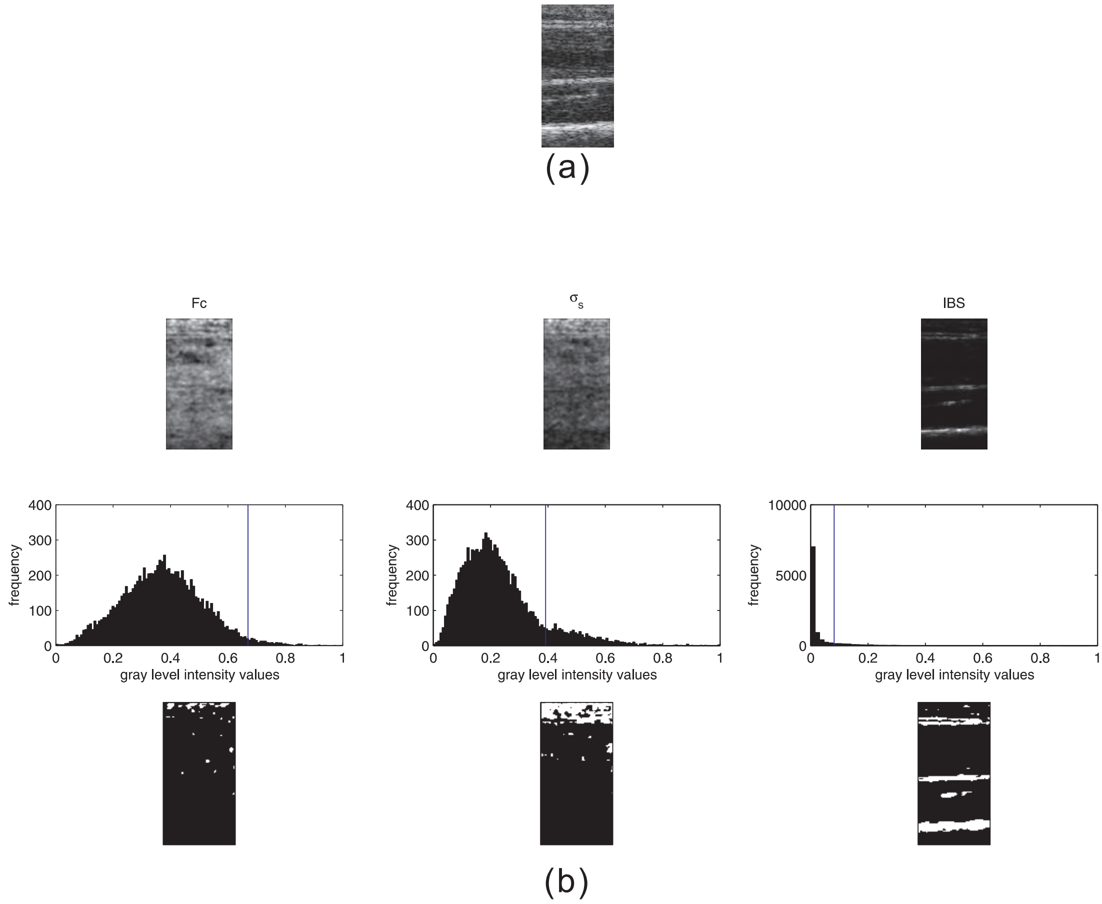

Figure 2.13: Results of thresholding on spectrum properties captured at the human thigh site. (a) B-mode image. (b) 2^{nd} to 4^{th} row: a spectrum property's image, histogram and binary map respectively. The vertical line in the histogram indicates the calculated threshold.

2.3 Fat Boundary Detection

Boundary detection is applied to the binary image obtained from thresholding. Since the binary image consists of holes and discontinuous edges due to inhomogeneity of the subcutaneous fat and fibrous connective tissues, a line fitting method called Random Sample Consensus (RANSAC) [84] is proposed to reject outliers and link the fat boundary candidates. First, boundary candidates are obtained from the binary image by differentiation. Then, RANSAC is used to fit the boundary candidates by assuming the fat boundary is a straight line. The assumption is based on the fact that while the fat boundary is naturally a curve, it approximates a straight line in the narrow field of a sagittal ultrasound image.

2.3.1 Extraction of Boundary Candidates

The binary map (BM) consists of only ones and zeros; therefore, boundary candidates can be located at the transition from zero to one, or from one to zero. In both vertical and horizontal directions, a transition happens when there is a difference in the binary values between the current and the next pixel and differentiation can be used to extract boundary candidates.

In the binary map of σ_s^2 ($BM_{\sigma_s^2}$), the possible fat region consists of ones, and the non-fat region consists of zeros; therefore, we assume fat boundary candidates happen when a transition from one to zero in the vertical direction and we do not consider edge pixels with zero to one transition in the vertical direction. Equation 2.8 is used to compute the likelihood of a pixel being a boundary candidate in a $BM_{\sigma_s^2}$ and is separated into three cases. Let $BM_{\sigma_s^2}(i,j)$ be a pixel in the binary map at the horizontal and vertical coordinates (i,j) and $(x,y)_{boundaryCandidate}$ be the coordinates of any boundary candidate. A boundary candidate exists at the coordinates $(x,y)_{boundaryCandidate}$ under the following conditions:

$$(x,y)_{boundaryCandidate} = \begin{cases} (i, j-0.5) & \text{if } BM_{\sigma_s^2}(i,j) - BM_{\sigma_s^2}(i,j-1) = -1 \\ (i+0.5, j) & \text{if } BM_{\sigma_s^2}(i+1,j) - BM_{\sigma_s^2}(i,j) = 1 \\ (i+0.5, j) & \text{if } BM_{\sigma_s^2}(i+1,j) - BM_{\sigma_s^2}(i,j) = -1 \end{cases} \tag{2.8}$$

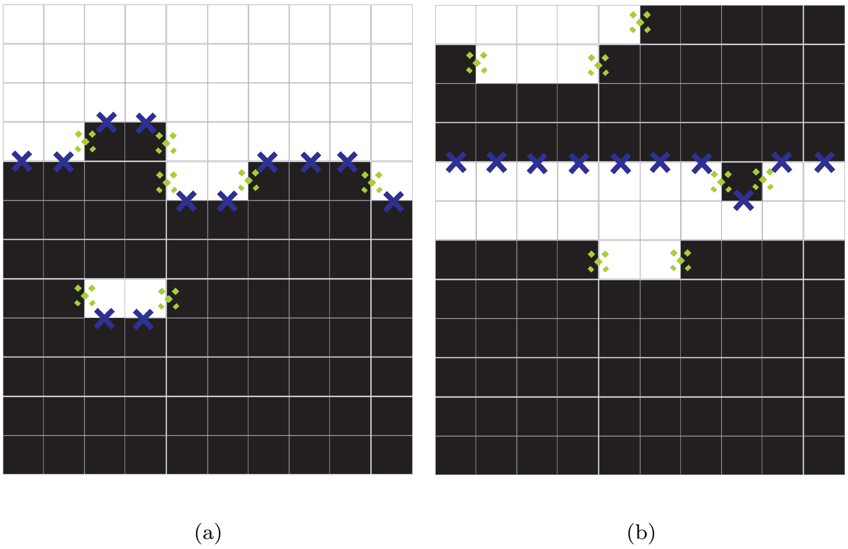

Figure 2.14: An example illustrates the extraction of boundary candidates in (a) a binary map of σ_s^2 using Equation 2.8 and (b) a binary map of IBS using Equation 2.9. A white pixel represents the value of one and a black pixel represents a pixel of zero. Blue solid crosses denote the boundary candidates obtained in the vertical direction and green dotted crosses denote the boundary candidates obtained in the horizontal direction.

Referring to the first case of Equation 2.8, a transition of a pixel valued one to a pixel valued zero in the vertical direction denotes an existence of a boundary candidate in between the two vertically adjacent pixels. In the second and third cases, a transition of a pixel valued one to a pixel valued zero or a transition of a pixel valued zero to a pixel valued one in the horizontal direction denotes an existence of a boundary candidate in between the two horizontally adjacent pixels. Since a boundary candidate is defined at the transition between two pixels, its coordinates (x,y) is recorded at the mid point between pixels. Figure 2.14(a) illustrates the usage of Equation 2.8.

In the binary maps of IBS (BM_{IBS}), strongly reflective interfaces appear as lines with certain thicknesses. Since the thickness of fascia is human dependent and the usual practice to find the fat thickness is from the skin to the surface of fascia [13], we assume fat boundary candidates are found at transition from zero to ones in the vertical direction and do not consider edge pixels with one to zero transition in the vertical direction. Equation 2.9 is used to compute the likelihood of a pixel being a boundary candidate in a BM_{IBS} and is separated into three cases. Let $BM_{IBS}(i,j)$ be a pixel in the binary map at the horizontal and vertical coordinates (i,j) and $(x,y)_{boundaryCandidate}$

be the coordinates of any boundary candidate. A boundary candidate exists at the coordinates $(x, y)_{boundaryCandidate}$ under the following conditions:

$$(x, y)_{boundaryCandidate} = \begin{cases} (i, j - 0.5) & \text{if } BM_{IBS}(i, j) - BM_{IBS}(i, j - 1) = 1 \\ (i + 0.5, j) & \text{if } BM_{IBS}(i + 1, j) - BM_{IBS}(i, j) = 1 \\ (i + 0.5, j) & \text{if } BM_{IBS}(i + 1, j) - BM_{IBS}(i, j) = -1 \end{cases} \tag{2.9}$$

Referring to the first case of Equation 2.9, a transition of a pixel valued zero to a pixel valued one in the vertical direction denotes an existence of a boundary candidate in between the two vertically adjacent pixels. In the second and third cases, a transition of a pixel valued one to a pixel valued zero or a transition of a pixel valued zero to a pixel valued one in the horizontal direction denotes an existence of a boundary candidate in between the two horizontally adjacent pixels. Since a boundary candidate is defined at the transition between two pixels, its coordinates (x, y) is recorded at the mid point between pixels. Figure 2.14(b) illustrates the usage of Equation 2.9.

2.3.2 Fitting Boundary Candidates using Random Sample Consensus (RANSAC)

Boundary candidates consist of edge points from not only the real fat boundary, but also from the fibrous membranes of connective tissues and noise. A line fitting algorithm is needed to cluster points that lie on the same structure. The Hough transform is the most general line fitting algorithm, but it suffers from quantization errors and difficulties with noise [85]. Considering our boundary candidates, it is noticed that the number of unwanted candidates highly depends on the body location, and the homogeneity and thickness of subcutaneous fat (e.g. more unwanted candidates are found in fat with thicker fibrous connective tissue and when the fat thickness is small.) It is difficult to pick a suitable grid size of the accumulator array for all different cases. Also, Forsyth and Ponce [85] have demonstrated this algorithm is very sensitive to noise. To fit a boundary in the presence of many outliers, the RANSAC algorithm is proposed due to its robustness to outliers.

2.3.2.1 Total Least Squares Fitting

Since the measurement error depends on the coordinate frame, total least squares fitting is used instead of using the classic least squares fitting. Although the least squares fitting is simple, it measures only the vertical distance error. Alternatively, the total least square fitting measures the perpendicular error which is more robust to pixel errors. The problem of total least square fitting is to minimize the sum of the perpendicular distances between points and lines, i.e.

$$\sum (ax_i + by_i + c)^2$$

and its minimization problem can be solved with the Lagrange multiplier and the final solution [85] is:

$$c = -a\overline{x} - b\overline{y} \tag{2.10}$$

$$A \begin{pmatrix} a \\ b \end{pmatrix} = \mu \begin{pmatrix} a \\ b \end{pmatrix} \tag{2.11}$$

$$\text{where A} = \begin{pmatrix} \overline{x^2} - \overline{x}\overline{x} & \overline{xy} - \overline{x}\overline{y} \\ \overline{xy} - \overline{x}\overline{y} & \overline{y^2} - \overline{y}\overline{y} \end{pmatrix}$$

Equation 2.11 is a 2D eigenvalue problem. Matlab function *eig* is used to find the two eigenvalues d and their eigenvectors $\overrightarrow{v}(v1, v2)$ of matrix A and gives

$$\begin{pmatrix} a \\ b \end{pmatrix} = d \begin{pmatrix} v_1 \\ v_2 \end{pmatrix}$$

Finally, a, b and c can be solved by choosing the eigenvalue d which gives the smallest $\sum (ax_i + by_i + c)^2$.

2.3.2.2 Theory and Implementation

RANSAC randomly picks and fits n data points, and checks how many data points can fit to a model. The process is iterative and continues until a high probability of finding the correct model is attained [84]. Given our model (i.e. the fat boundary) is a line structure, our problem is to fit the edge candidates to a line whose equation is $ax + by + c = 0$. The algorithm is outlined in the following:

```
Loop until $k$ iterations have occurred

  1. Select $n$ boundary candidates at random.

  2. Fit the set of $n$ data points and find a line model using total least squares fitting.

  3. If determinant of matrix A (from Equation 2.11) is not zero:
       To find boundary candidates that are close to the line model:
       For each boundary candidate
           Test the perpendicular distance ($dist$) to the line model,
           If $dist \leq t$,
              Keep boundary candidate
           End If
       End For
     End If

  4. If (number of candidates) > (current maximum number of good candidates)
       Save the current sets of boundary candidates.
       Update $k$ by using equation (2.12).
     EndIf

End Loop
```

In the algorithm, three parameters are needed to be determined and they are:

- n is the smallest number of points required to fit the model.
- t is the threshold (in pixel) required to determine if the data fit well.
- k is the number of iterations required for the algorithm.

Parameter n is dependent on the fitting model. In our case, n is set to 2 because only two points are required to fit a straight line. Occasionally, two randomly picked candidates may fail to fit the line model (e.g. if two candidates are too close to each other.) To ensure the fitting model is valid, the determinant of matrix A is calculated and checked if it is zero. If the determinant value is zero, the two candidates cannot generate a valid line model.

Parameter t determines whether a boundary candidate is sufficiently close to the fitting model and represents the maximum perpendicular distance from a good candidate to the fitting line. This parameter can be decided by varying the pixel values (in our case, we tried between 0.5 and 2.5 pixels) in our data sets and visually determining the best fit. By trial and error in our experiments, t is set to 1 pixel.

Parameter k can be found by considering the probability of k consecutive failures and the probability of good fit of a random data (P_{fit}) (P_{fail}) [85]:

$$\begin{aligned} P_{fail} &= (1 - {P_{fit}}^{n})^{k} \\ k &= \frac{log(P_{fail})}{log(1 - {P_{fit}}^{n})} \end{aligned} \tag{2.12}$$

We assume the probability of a successful fitting is 99% and therefore P_{fail} is set to 0.01. k is updated whenever a better set of boundary candidates is found.

Figures 2.15, 2.17 and 2.19 show the results of boundary detection on σ_s^2 and Figures 2.16, 2.18 and 2.20 show the results of boundary detection on IBS. In the figures, sub-figure(a) shows the boundary candidates extracted by the differentiation method as described in section 2.3.1 and sub-figure(b) shows the boundary detected by RANSAC. The RANSAC algorithm successfully omits the false boundary candidates caused by holes within the fat tissue area (i.e. binary value equals 1) and pixels from noise.

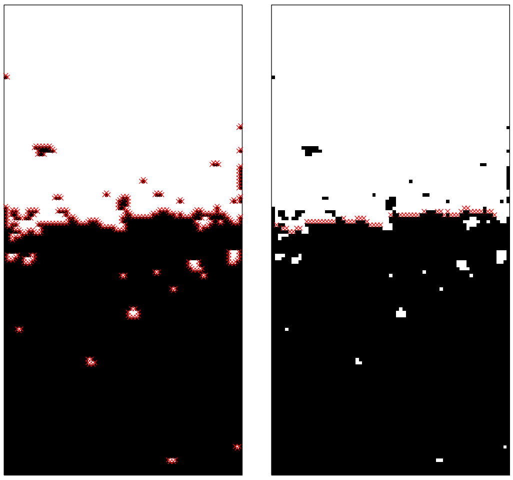

(a) (b)

Figure 2.15: Results of extraction and detection of boundary candidates from the binary map $BM_{\sigma_s^2}$ obtained from a human suprailiac site: (a) potential boundary candidates (red crosses) and (b) fat boundary candidates found by RANSAC (red crosses).

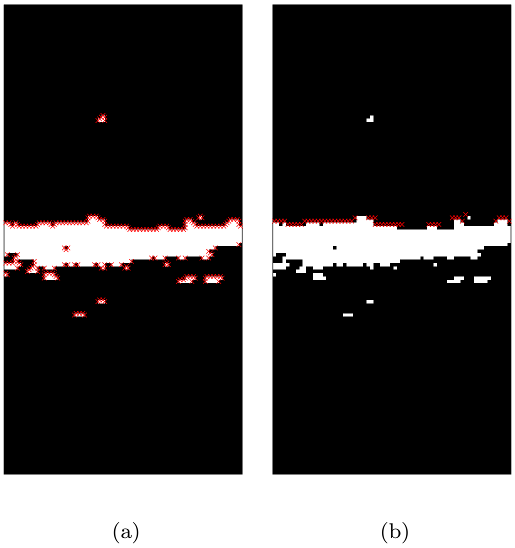
(a) (b)

Figure 2.16: Results of extraction and detection of boundary candidates from the binary map BM_{IBS} obtained from a human suprailiac site: (a) potential boundary candidates (red crosses) and (b) fat boundary candidates found by RANSAC (red crosses).

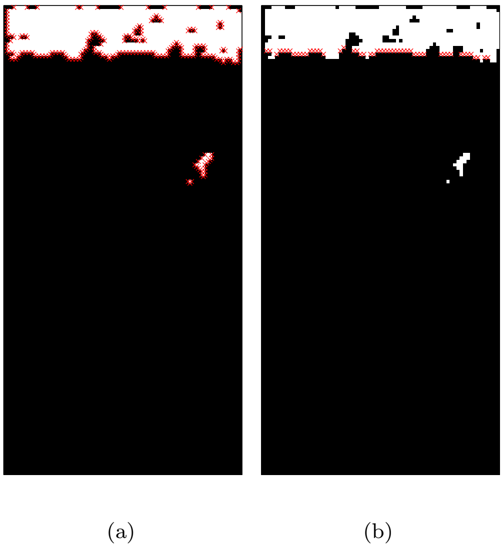
(a) (b)

Figure 2.17: Results of extraction and detection of boundary candidates from the binary map $BM_{\sigma_s^2}$ obtained from a human triceps: (a) potential boundary candidates (red crosses) and (b) fat boundary candidates found by RANSAC (red crosses).

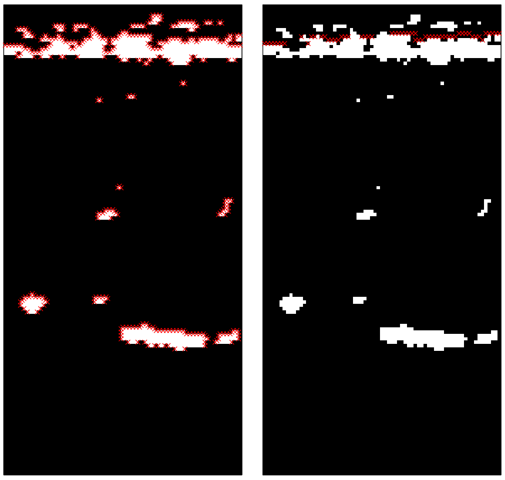

(a) (b)

Figure 2.18: Results of extraction and detection of boundary candidates from the binary map BM_{IBS} obtained from a human triceps: (a) potential boundary candidates (red crosses) and (b) fat boundary candidates found by RANSAC (red crosses).

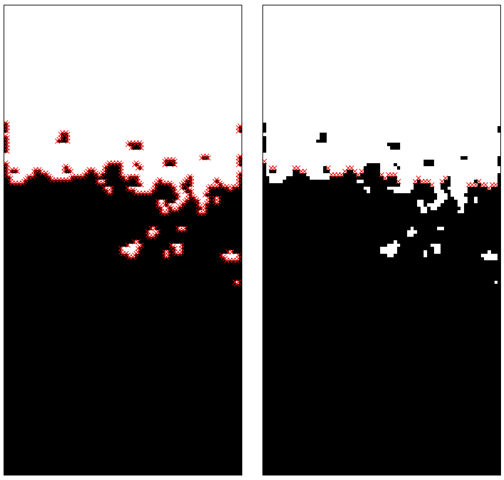

(a) (b)

Figure 2.19: Results of extraction and detection of boundary candidates from the binary map $BM_{\sigma_s^2}$ obtained from a human thigh: (a) potential boundary candidates (red crosses) and (b) fat boundary candidates found by RANSAC (red crosses).

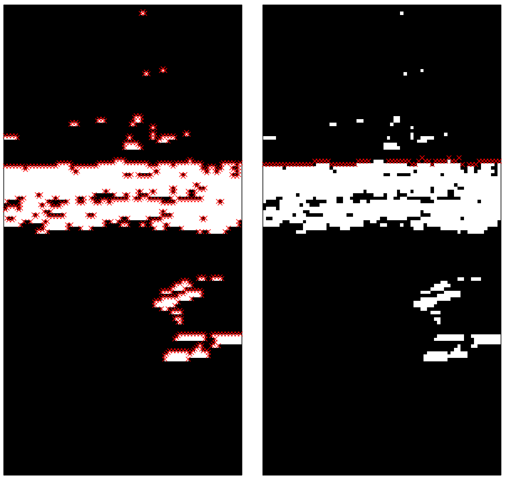

(a) (b)

Figure 2.20: Results of extraction and detection of boundary candidates from the binary map BM_{IBS} obtained from a human thigh: (a) potential boundary candidates (red crosses) and (b) fat boundary candidates found by RANSAC (red crosses).

2.3.3 Calculation of Spectral Content using Multiple Focuses

There is only one focus available in the RF data capture mode of our ultrasound machine. However, fat thicknesses can be different among people and the focus at a fixed position may not be appropriate for all thicknesses. For the above reason, the use of multiple focal points is considered. RF data is separately captured for different focuses and converted to spectrum properties by spatial compounding. Two approaches are investigated to combine spectrum properties obtained by multiple focuses: stitching and averaging.

2.3.3.1 Stitching Focused Spectrum Properties (MF1)

The approach of stitching combines a spectrum property obtained from several focuses as shown in Figure 2.21(a). This is an idea of combining the focused spectrum property values from pairs of focuses. The region of focus F_x is overlapped with the next focus F_{x+1}. To guarantee a smooth transition, the two regions are combined by a ramp-like weight function as shown in Figure 2.21(b). In the overlapping region, the sum of the weights from region F_x and F_{x+1} at a certain depth is 100%, and the weight of region F_x decreases when the depth increases and the weight of region F_{x+1} increases when the depth increases. Focuses F_x at 10mm, 20mm, 30mm and 40mm are used in our experiments.

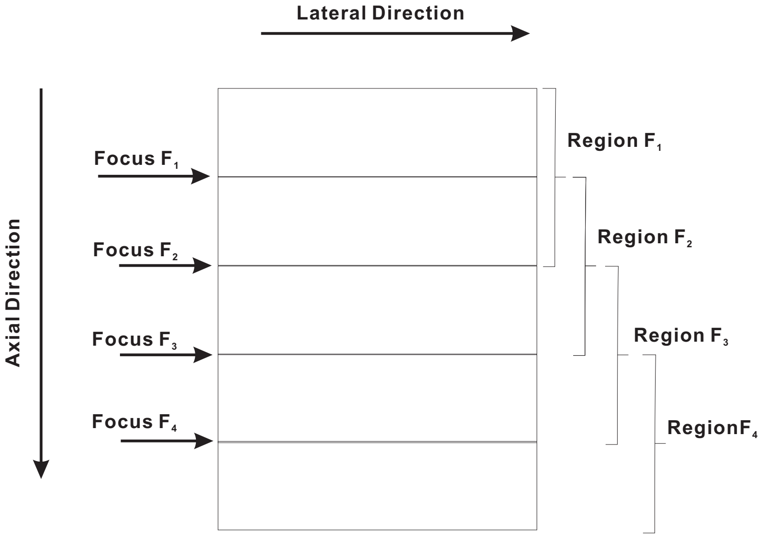

(a)

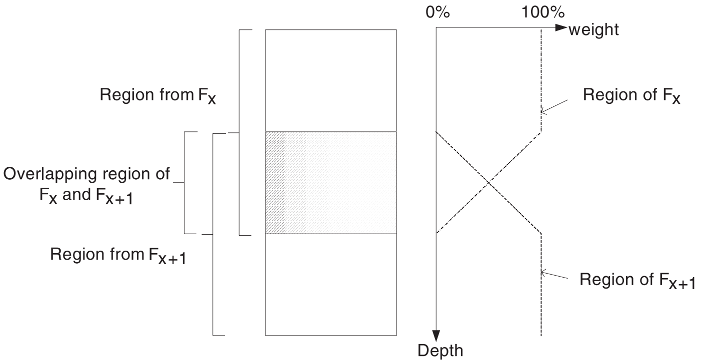

(b)

Figure 2.21: Stitching of a spectrum property map obtained from multiple focuses: (a) stitching of spectrum properties values (b) the weight function that combines two overlapping regions.

2.3.3.2 Averaging Spectrum Properties from Multiple Focuses (MF2)

This approach simply averages all the whole parametric images obtained from multiple focuses. The idea is to smooth parametric images and reduce the effect of a particular focus.

2.3.3.3 Results

Figure 2.22 shows the resulting compound parametric images of σ_s^2 and IBS obtained at different single focuses and the result of stitching (MF1) and averaging (MF2) multiple focuses. It is shown that the results of using the averaging method (MF2) gives a smoother σ_s^2 and IBS and leads to a binary map with fewer holes.

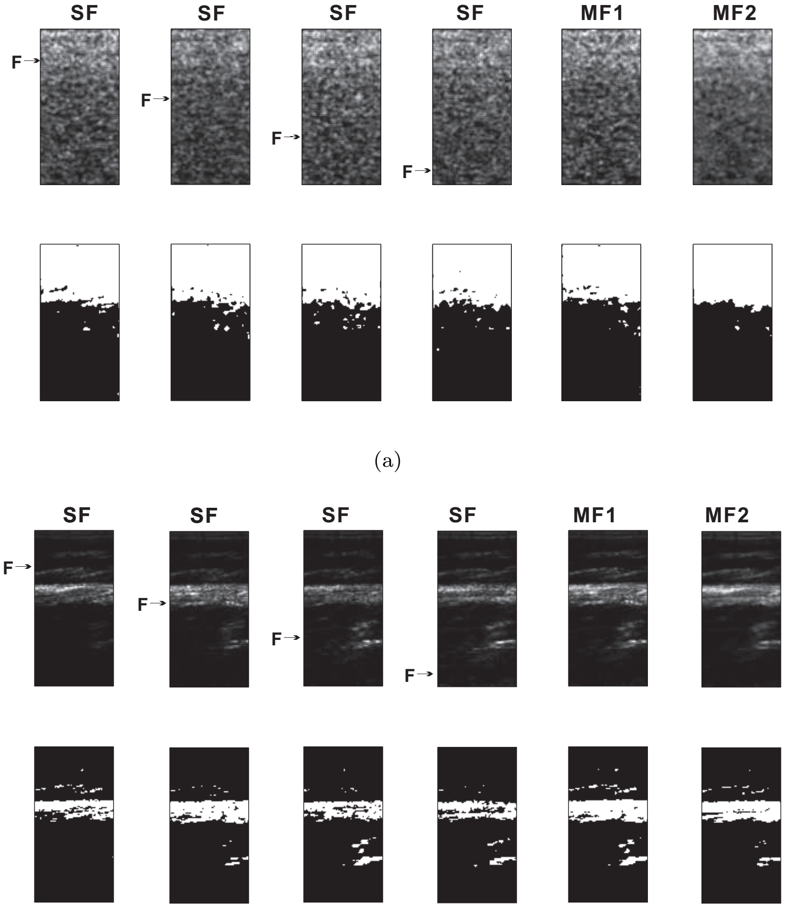

(a)

(b)

Figure 2.22: The comparisons between (a)σ_s^2 and (b)IBS obtained from: (1^{st}-4^{th} column) single focuses (SF) where **F** indicates the focus position, (5^{th} column) stitching spectrum properties from multiple focuses (MF1) and (6^{th} column) averaging spectrum properties from multiple focuses (MF2).

2.4 Summary

We investigated the characteristics of human subcutaneous fat in terms of the properties of power spectrum and encoded the values of spectrum properties into gray-scale parametric images. Then, we presented the method of image processing and fat boundary detection on these parametric image. We found that the spectrum properties σ_s^2 and IBS could be used to characterize subcutaneous fat. The parametric image of σ_s^2 represents a coarse area of the subcutaneous fat tissue and the parametric image of IBS represents potential locations of the fascia.

The characteristics of fat observed in the parametric images of σ_s^2 and IBS are more distinct after the application of spatial compounding that reduces spectrum noise due to speckle. The parametric image of σ_s^2 shows the area of subcutaneous fat and the parametric image of IBS shows the potential area of the fascia and other strong tissue reflectors. The histogram of the parametric image of σ_s^2 shows that fat pixels change more rapidly than non-fat pixel and a long tail in the histogram results. We suggested that the relative rapid change in the gray-intensity values of fat pixels is due to the high variation in the tissue structure of subcutaneous fat. This causes high fluctuations in the received spectrum, and this results a more rapid change in the spectrum variance.

Histograms of σ_s^2 can be bimodal or unimodal; the Rosin's unimodal thresholding method is used to detect the global threshold which separated the fat and non-fat pixels in the parametric images of σ_s^2. The same thresholding method was applied to the parametric images of IBS. Then, boundary candidates were extracted from the binary map and the fat boundary was detected by RANSAC. Total least squares was used as a fitting algorithm and we were able to use a the same fitting threshold (i.e. 1 pixel) to detect the fat boundary at the human suprailiac, triceps and thigh sites. Finally, we proposed two methods: the stitching and averaging spectrum properties obtained from multiple focuses to overcome the drawbacks of a single focus.

Chapter 3

Experimental Methodology

This chapter presents an overall framework of our human subcutaneous fat detection method using the spectrum properties of RF data, which we discussed in Chapter 2. To test our algorithm, our subcutaneous fat detection framework was applied to human participants at the suprailiac, triceps and thigh sites. These sites were chosen because they have a good range of fat thickness and they have been popularly used for the assessment of body fat in both females and males [13]. Different properties of fat are also seen in these regions: fat at the suprailiac site is more homogeneous, whereas fat in the thigh and triceps is less homogeneous and varies in the density of fibrous connective tissue. Furthermore, these body sites have large regions of flat areas that allow the linear transducer to make a complete contact with the skin surface without compression. The ultrasound measurements will also be compared to the skinfold caliper measurements. The procedures for using ultrasound and skinfold caliper to measure subcutaneous fat are described at the end of this chapter.

3.1 Overview of the Human Subcutaneous Fat Detection Framework

The overview of the human subcutaneous fat detection framework is shown in Figure 3.1. The detection process is divided into four main steps: data capture, calculation of spectrum parameters, preprocessing of spectrum properties maps and segmentation.

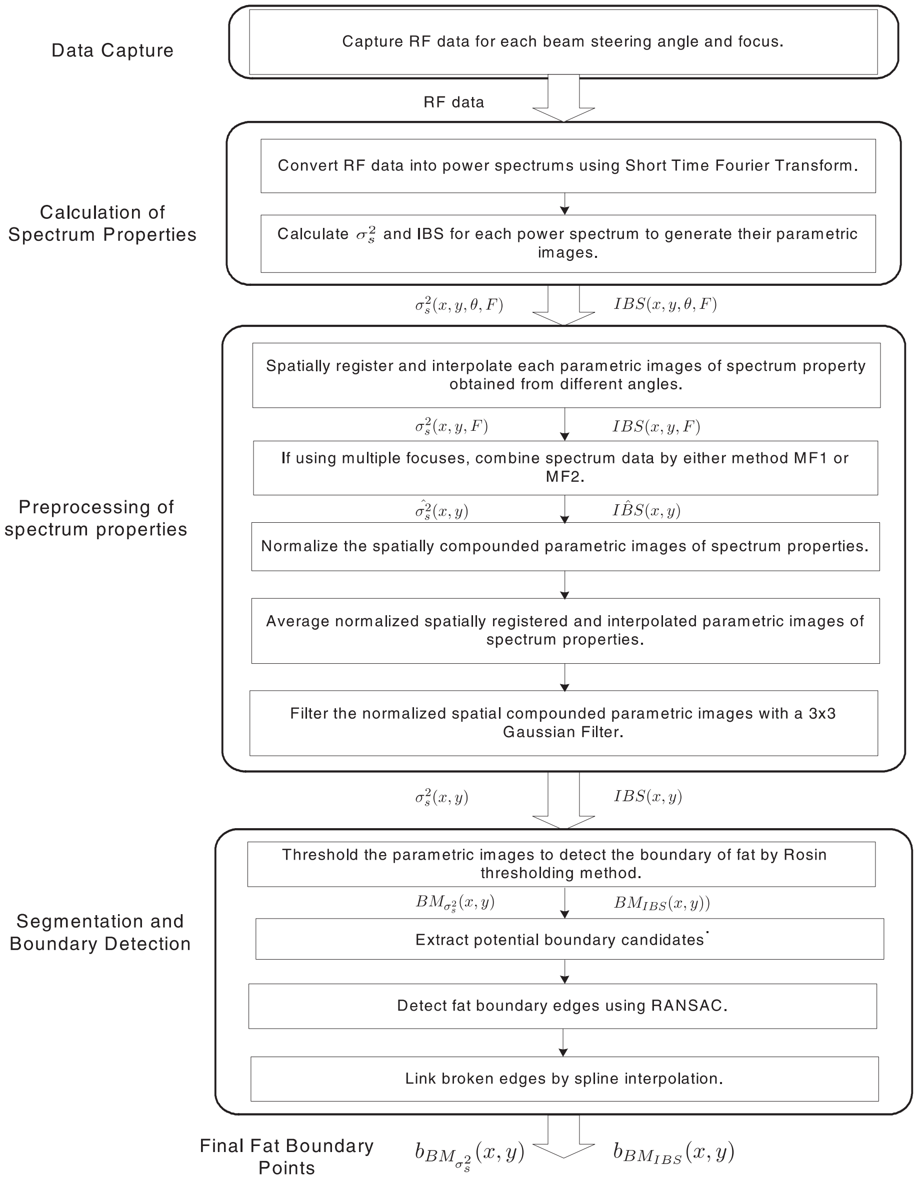

Figure 3.1: The framework of human subcutaneous fat detection.

3.1.1 Data capture

RF data was captured by using an Ultrasonix ES500 (Ultrasonix Medical Corporation, Burnaby, BC) with a L9-4 linear transducer. The L9-4 linear transducer operates in a frequency range between 4 and 9MHz. In our experiment, the central transducer frequency was set to 6.6MHz. The research package of the ES500 allowed us to build software for direct access to the RF data and control of ultrasound parameters like transducer frequency, field of view and time gain compensation (TGC).

RF data capture software was written in Visual C++ and Microsoft Foundation Classes (MFC). A frame of RF data was captured for each steering angle and each focus. The software also allowed users to control the number and step size of compounding angle and number of focuses. Changing the focus position was faster than the steering angle, so the fastest sequence of data collection is shown in Figure 3.2. TGC was set to the “Muscleskeleton”preset on the ES500.

The data scanning depth was 50mm and the scanning width was 38.2mm. Each frame of RF data consisted of 127 RF scan lines and each scan line consisted of 2560 data points. 11 compounding angles at a 2° step size were used for the human experiment. Data were captured at each focus every 10mm, from 10mm to 40mm.

With the beam angle steering function, the current refresh rate in capturing a frame of RF data is 2Hz with the size of RF data stated above. Frames of RF data were saved to files for later offline processing in Matlab.

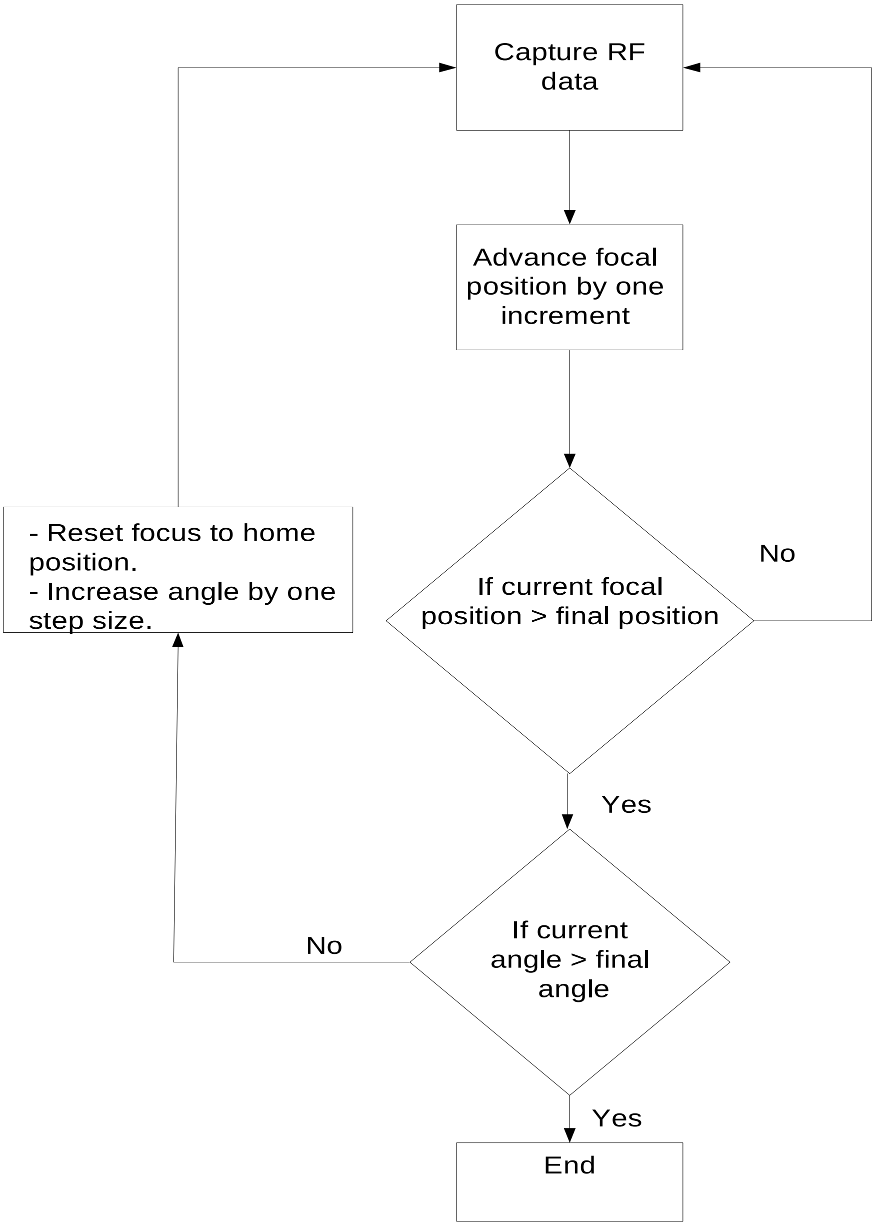

Figure 3.2: The sequence of capturing RF data.

3.1.2 Calculation of Spectrum Properties

The second step is to calculate spectrum properties from RF data captured at each steering angle (θ) and focus position (F). From the experiment mentioned in Section 2.1.2.2.2, we found that σ_s^2 and IBS were the most indicative factors in determining the fat boundary. Therefore, we only considered the calculation of σ_s^2 and IBS in our framework. The local power spectrum and their spectrum properties are computed as in Section 2.1.1. As a result, the parametric images of spectrum properties $\sigma_s^2(x, y, \theta, F)$ and $IBS(x, y, \theta, F)$ are computed at each θ and F.

3.1.3 Pre-processing of Spectrum Properties Map

The next step is the pre-processing which includes spatial compounding and combining data from multiple-focused parametric images. The values of $\sigma_s^2(x, y, \theta, F)$ and $IBS(x, y, \theta, F)$ at each focus position are first spatially compounded to the parametric images $\sigma_s^2(x, y, F)$ and $IBS(x, y, F)$. Spatial compounding converts the parametric images from their data coordinates to the spatial coordinates and the method was described in detail in Section 2.1.2. After that, the parametric images captured at different focal positions are combined with the method of Section 2.3.3. The resultant parametric images of $\hat{\sigma_s^2}(x, y)$ and $I\hat{B}S(x, y)$ are normalized. The normalization rescales the pixel intensity values of spectrum properties maps between 0 to 1, and increases the contrast between layers. The normalized $\hat{\sigma_s^2}(x, y)$ and $I\hat{B}S(x, y)$ are then smoothed by a 3x3 Gaussian filter to further remove noise. The compounded, normalized and smoothed parametric images of $\sigma_s^2(x, y)$ and $IBS(x, y)$ will be used for segmentation.

3.1.4 Segmentation

Lastly, the fat boundary was delineated from the parametric images by Rosin's thresholding and RANSAC. An intensity histogram of 128 bins was computed from each parametric image. Rosin's thresholding, which is described in Section 2.2, was used to find the threshold and obtain a binary map representing the subcutaneous fat layer. The threshold indicates the change from subcutaneous fat to the muscle layer.

Potential boundary candidates were obtained from the binary maps ($BM_{\sigma_s^2}(x, y)$ and $BM_{IBS}(x, y)$) using the differentiation method defined in Section 2.3.1. RANSAC is then applied to find the fat edges. As mentioned before in Section 2.3.2.2, the parameter n (i.e. smallest number of points required to fit the model) was set to 2, and the parameter t (i.e. the threshold required to determine if the data fit well) was set to 1 pixel. The detected edges of the fat boundary may be incomplete; therefore, cubic spline interpolation was used to link broken edges using Matlab toolbox to obtain the final fat boundary $b_{BM_{\sigma_s^2}}(x, y)$ and $b_{BM_{IBS}}(x, y)$. The reason for choosing the cubic spline interpolation over the linear interpolation is that the resulting boundary is smoother in the former case. Figure 3.3 illustrates an example of the segmentation.

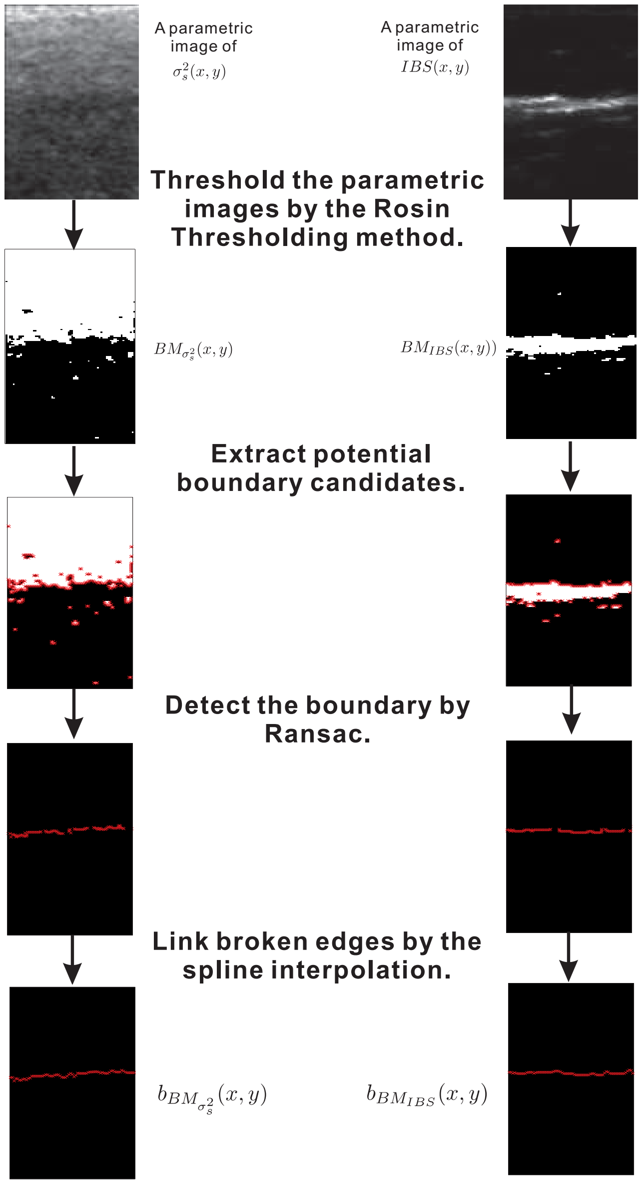

Figure 3.3: An example illustrates the segementation process on the parametric images of σ_s and IBS.

3.2 Procedures in User Study

Nine volunteers - five females and four males aged between 20 to 30 – were recruited for the user study[1]. The study consisted of two parts: skinfold caliper measurements and ultrasound data capture. The skinfold caliper test was carried out before the ultrasound test to avoid bias on skinfold measurements.

Measurements took place at three body sites: the suprailiac, triceps and thigh areas. For the skinfold caliper and ultrasound measurements, two sets of results were both collected on the left and right sides of the body as shown in Figure 3.4. The direction of the arrows indicates the grasp of the skinfold caliper. At the suprailiac site(Figure 3.4(a)), the measurement was taken at above the crest of the ilium in a diagonal fold of skin. Measurements were taken midway between the shoulder and elbow at the triceps (Figure 3.4(b)), and midway between the inguinal crease and proximal border of patella figure(3.4(c)). In addition, two sets of ultrasound data, one set from each side of the body, were taken at each site at random locations. As a result, there were 36 sets of ultrasound data for evaluating the results of segmentation and 18 sets of skinfold and ultrasound data for evaluating the results between skinfold and automatic ultrasound measurements. The procedures for the skinfold and ultrasound measurements are presented in the next section. Since our method is compared to manual segmentation, the procedure of manually locating the fat boundary is also presented.

3.2.1 Measurement of Skinfold Fat Thickness

Prior to the user study, the investigator[2] practiced the skinfold caliper technique until consistent measurements were obtained. A Lange caliper (Figure 3.5) was used throughout the experiment. The maximum thickness that can be measured by this caliper is 60mm. The reading was recorded to the nearest 0.5mm.

The investigator followed the skinfold measurement technique prescribed by the Canadian Society for Exercise Physiology [86] and was instructed by an experienced skinfold caliper operator[3]. During the procedures, the participants were asked to stand and relax. A cross, which indicated the

---

[1] This study was reviewed and approved by the Behavioral Research Ethics Board, Reference No.: B05-0820. The copy of the certificate is attached in the Appendix D.

[2] Jessie Ng, author of this thesis.

[3] Barry Legh, Senior Instructor, Human Kinetics Department, UBC.

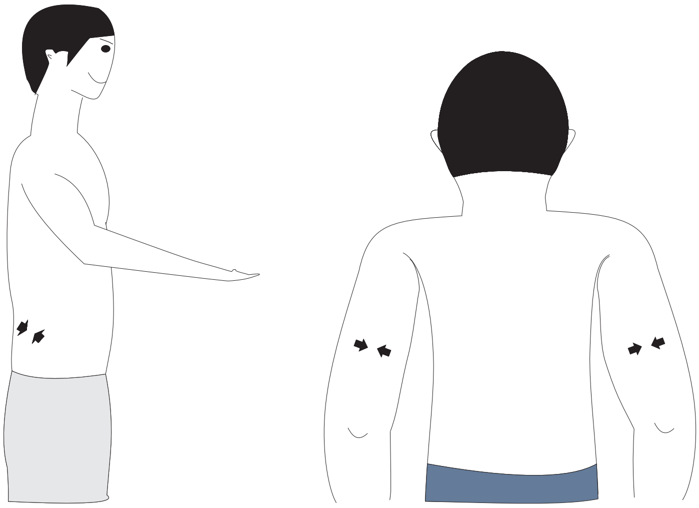

(a) suprailiac (b) triceps

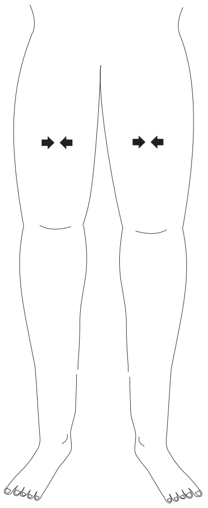

(c) thigh

Figure 3.4: Body sites selected for skinfold caliper and ultrasound measurements. The direction of the arrows indicates the grasp of the skinfold caliper.

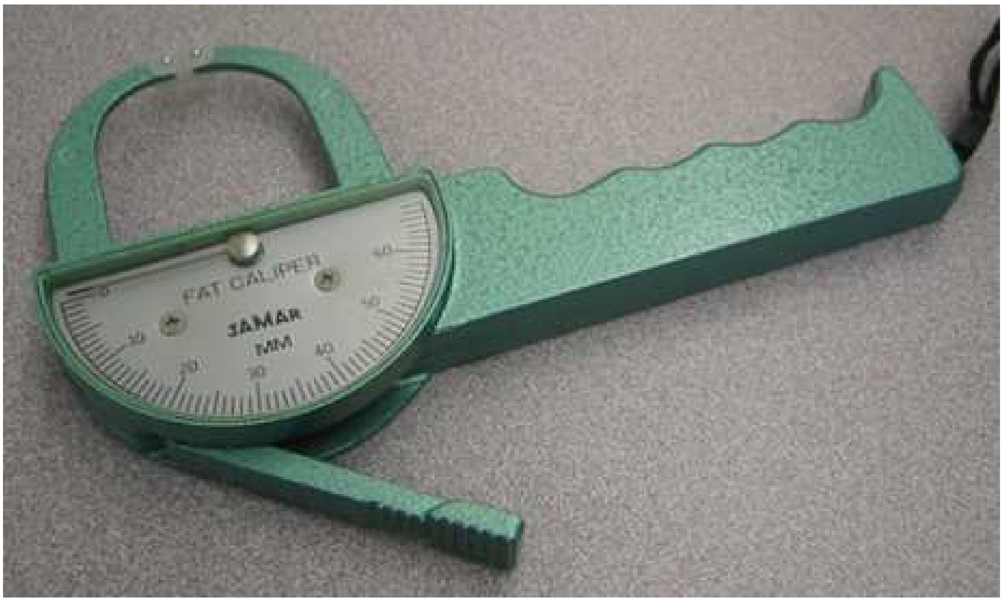

Figure 3.5: A Lange skinfold caliper.

location of the skinfold grip, was first pen-marked on the skin of the site. The skinfold of fat was grasped by the thumb and forefinger with one hand 1cm above the pen-mark. The grasped skinfold was shaken with both fingers to avoid including the muscle layer in the measurement. With the caliper in another hand, the caliper was positioned at the pen-mark and released. The pressure of fingers should be maintained during the release of the caliper. A reading was taken after the complete release of the caliper and the indicator on the caliper had become stable. Measurements were repeated three times and the final result was the mean of the three measurements. Furthermore, to ensure consistency in maintenance of the pressure by fingers on the skinfold, all measurements were made by the same investigator.

3.2.2 Collection of Ultrasound Data

Ultrasound data collection was performed after the collection of skinfold measurement data. The settings of the ultrasound machine and the type of the transducer used have been detailed in Section 3.1.1. To ensure proper contact of the transducer with the skin, and valid capture of data, the B-mode image was used to aid the capture process to obtain good image quality. If the investigator was unable to recognize the fat layer, adjustments were made to the position or orientation of the transducer. Since the fascia is specular in nature, the brightness of the fascia is affected on the incident angle of the ultrasound. The B-mode image can also help the investigator to adjust the orientation of the transducer for obtaining maximum reflection from the fascia. At the triceps and the thigh, the transducer was positioned in the sagittal plane. This is because the transducer is a linear array and it is not convenient for it to be placed on an arched surface. Also, tissue compression can be avoided.

Ultrasound gel was applied to the skin to act as a coupling medium between the skin and the transducer. For each body site, the center of the ultrasound transducer was positioned at the cross. Ultrasound measurements were taken in the sagittal plane for the triceps and thigh. At the suprailiac site, the transducer was aligned to match the direction of skinfold measurement. The thickness of the gel was just enough (∼0.1mm) to obtain a clear B-mode image. Excessive gel was removed by sweeping the transducer back and forth. Moreover, the transducer was kept upright to the skin. The investigator applied just enough pressure on the transducer to allow contact between its surface and the skin while avoiding the compression of the subcutaneous fat layer. From our experience, the compressibility of fat can be up to approximately 1/3 of the original fat thickness depending on the total fat thickness. This could be determined from the B-mode image by observing the change in the thickness of fat when it was alternatively compressed and relaxed.

3.2.3 Reference Fat Boundary from Manual Segmentation

The automatic segmentation result was compared to that for manual segmentation. The reference fat boundary, which is defined as the thickness between the skin surface and the fascia surface, was obtained by manual delineation on the B-mode image. For each column of the B-mode image, the investigator clicked on the pixel that could be recognized as the fat boundary. The selected boundary edges were linked together by cubic spline interpolation to obtain a complete boundary.

3.3 Evaluation Method

In our application, we are interested in finding the fascia, which is the subcutaneous fat boundary, and comparing it to our reference boundary obtained by manual segmentation. To evaluate the boundary error between manual segmentation and auto-detection, we used two parameters: the average thickness error (d_{ERR}) and the root mean square error (d_{RMS}).

Assume a boundary B consisting of a set of N boundary points, then B can be represented as:

$$B = \{(b_{1x}, b_{1y}), (b_{2x}, b_{2y}), ..., (b_{nx}, b_{ny})...(b_{Nx}, b_{Ny})\}$$

where b_{nx} is the x-coordinate and b_{ny} is the y-coordinate of a boundary candidate. We will define the coordinates of the reference boundary as $R = \{(r_{1x}, r_{1y}), (r_{2x}, r_{2y}), ..., (r_{nx}, r_{ny}), ...(r_{Nx}, r_{Ny})\}$ and the segmented boundary as $S = \{(s_{1x}, s_{1y}), (s_{2x}, s_{2y}), ..., (s_{nx}, s_{ny}), ...(s_{Nx}, s_{Ny})\}$ for calculating d_{ERR} and d_{RMS} in the following sections.

3.3.1 Average Thickness Error Metrics

Since the average thickness ($\overline{d}$) of S is

$$\overline{d} = \frac{\sum_{n=1}^{N} b_{ny}}{N} \tag{3.1}$$

where b_{ny} is the depth of an edge point b_n and N is the total number of edge points. Then, the average thickness error (d_{ERR}) between the reference boundary and the segmented boundary is the sum of the differences between their y-coordinates at the same column of pixels. We define d_{ERR} as:

$$d_{ERR} = \frac{\sum_{n=1}^{N} (s_{ny} - r_{ny})}{N} \tag{3.2}$$

where s_{ny} is the y-coordinate of an edge point in the segmented boundary S and r_{ny} is the y-coordinate of an edge point in the reference boundary R. A positive d_{ERR} indicates the detected average thickness is overestimated and a negative d_{ERR} indicates the detected average thickness is underestimated. In our evaluation, the reference boundary is the boundary obtained from manual segmentation.

Note that d and d_{ERR} are in pixels. To convert their unit to mm, we can multiple them by a conversion factor C. If a scan line of RF data consists of N_{rf} points, the window size of STFT is w and the image depth is D, C can be calculated as:

$$C = \frac{D}{N_{rf}} * \frac{w}{2} \tag{3.3}$$

$N_{rf} = 2560$, $w = 32$ and $D = 50mm$ in our experiment. Therefore, C equals 0.31 $mm/pixel$.

3.3.2 Root Mean Square Error Metric

Since the positive and negative errors can cancel in d_{ERR}, we also look into the root mean square error (d_{RMS}) that tells the deviation of a boundary measurement. To measure the root mean square difference between the reference and the segmented boundaries, d_{RMS} was used and it can be calculated as follows:

$$d_{RMS} = \sqrt{\frac{\sum_{n=1}^{N} \left(s_{ny} - r_{ny}\right)^2}{N}} \tag{3.4}$$

where s_{ny} is the y-coordinate of an edge point in the segmented boundary S, r_{ny} is the y-coordinate of an edge point in the reference boundary R and d_{ERR} is the average thickness error. The d_{RMS} is the average distance of a data point from the reference boundary, measured along a vertical distance. In our evaluation, the reference boundary is the boundary obtained from manual segmentation.

3.3.3 Difference against Mean

In addition to the evaluation of results between the manual and automatic ultrasound measurements, we also compare the average thickness of the ultrasound measurements with the $\frac{1}{2}$ skinfold caliper measurements. The $\frac{1}{2}$ skinfold thicknesses is used because the skinfold caliper measures a fold of skin that comprises two layers of subcutaneous fat. Since the ultrasound and skinfold are two independent measurements and we do not know the true value of fat thickness, the method of difference against mean helps us to investigate the possible relationship between the measurement error and the true value [87].

As shown in Figure 3.6, the mean difference $\overline{D}$ and the standard deviation of differences(s) are used to characterize the difference against mean between the skinfold and ultrasound measurements. The x-axis is the paired mean between the $\frac{1}{2}$ skinfold and ultrasound measurements, and the y-axis is the paired difference between the $\frac{1}{2}$ skinfold and ultrasound measurements. $\overline{D}$ is the systematic difference between methods and s is the standard deviation of differences. $\overline{D}\pm 2s$ indicates the 95% limits of agreement.

3.4 Summary

The overall subcutaneous fat detection framework was discussed. The subcutaneous fat detection involved four main steps: RF data capture, calculation of σ_s^2 and IBS from the local spectrum

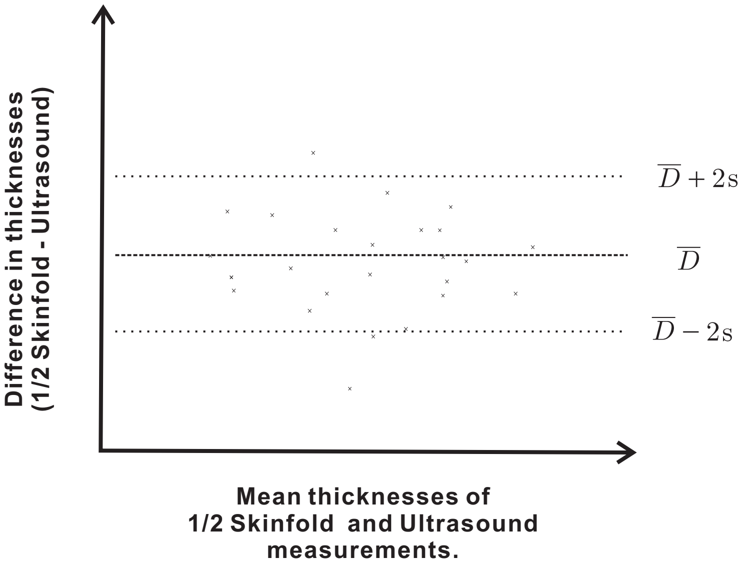

Figure 3.6: A figure showing the mean difference $\overline{D}$ and the standard deviation of differences(s) between two methods. Example data are provided for illustration.

of RF data, pre-processing of the parametric images of spectrum properties using spatial compounding and segmentation. Two detection results are obtained from σ_s^2 and IBS respectively. To evaluate our automatic segmentation results, the manually detected boundaries from ultrasound B-mode images were first used as reference boundaries to compare with the automatically detected boundaries. The average thickness error (d_{ERR}) and the root mean square error d_{RMS} were used to evaluate the manual and automatic results. The second part of the evaluation was to compare the ultrasound measurements with the skinfold caliper measurements. We finally presented the method of difference against mean for the comparison between the ultrasound measurements and the $frac12$ skinfold caliper values.

Chapter 4

Evaluation of Results

This chapter presents the results of subcutaneous fat boundary detection using the proposed imaging processing and detection framework. In Chapter 2, we showed that compound parametric images of σ_s^2 indicate the subcutaneous fat region while the compound parametric images of IBS indicates possible location of fascia and other strongly reflective tissue. Therefore, we first illustrate and discuss the qualitative results of segmentation using σ_s^2. Then the average thickness and the root mean square thickness errors between the manual and automatic ultrasound measurements are used to quantitatively evaluate our segmentation results. In the quantitative evaluation, the difference between using σ_s^2 and IBS as our segmentation factors is first assessed. Then, we compare the segmentation results obtained from a single focus (SF), stitching spectrum properties from multiple focuses (MF1) and averaging spectrum properties from multiple focuses(MF2). Lastly, the correlations between ultrasound (both manual and automatic methods) and the half skinfold caliper measurements are presented.

4.1 Qualitative Results: Segmentation Using Spectrum Variance σ_s^2

For human subcutaneous fat detection framework is applied to human in vivo, this section presents the qualitative result of segmentation with σ_s^2 obtained from a single focus. Figures 4.1(a) to 4.1(i) illustrate some results from the fat detection algorithm for subcutaneous fat with different body sites, thickness and structure. The cyan boundaries represent the result of the manual segmentation carried out by the investigator prior to the automatic segmentation, and the red boundaries represent the result of the automatic segmentation. The structure of fat tissue is human dependent and the fat tissue found at the suprailiac site is more homogeneous than that at the triceps and thigh. At the triceps and thigh, the structure is more complicated as more fibrous membranes are dispersed within the fat tissue. The length, density and thickness of fibrous tissue membranes vary in these examples; however, our fat detection algorithm is able to identify the location of the fat boundaries with varying degrees of accuracy.

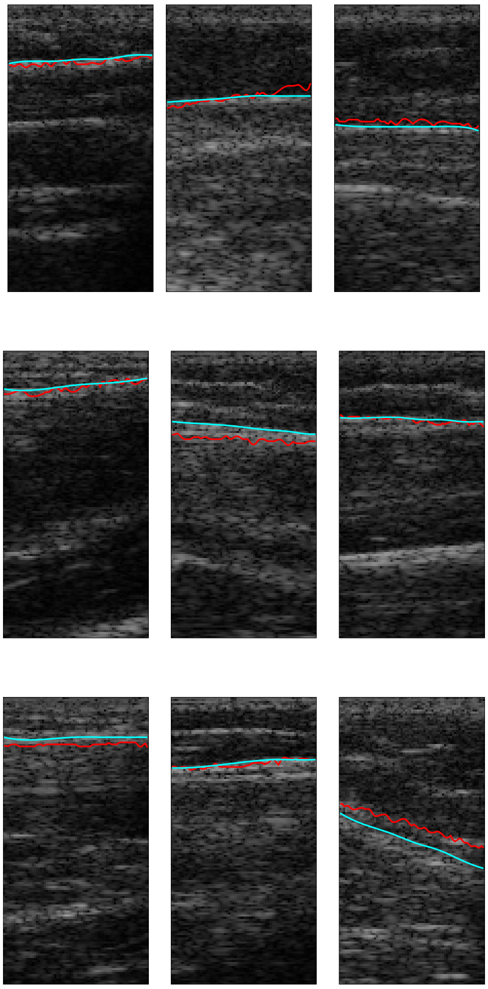

Figure 4.1: Examples (1^{st} row: suprailiac, 2^{nd} row: triceps and 3^{rd} row: thigh) demonstrate the segmentation results of σ_s^2 at a single focus obtained from different structures and thicknesses of subcutaneous fat tissue. The cyan boundary is the manual segmentation and the red boundary is the automatic segmentation.

It is harder to detect the fascia boundary when the layer of fat is thin. As shown in the B-mode images of Figures 4.2(a) and 4.2(b), the subcutaneous fat and the location of fascia are not obvious. The skin is close to the fascia and the subcutaneous fat layer consists of dense fibrous connective tissues. Since only a small amount of fat tissue is observed between the skin and the fat boundary, it is hard to detect the fat boundary. In the above figures, our algorithm falsely detects the fat boundary at the location near the skin. The binary images of σ_s^2 show that there are too many boundary candidates and this leads to errors in boundary detection using RANSAC.

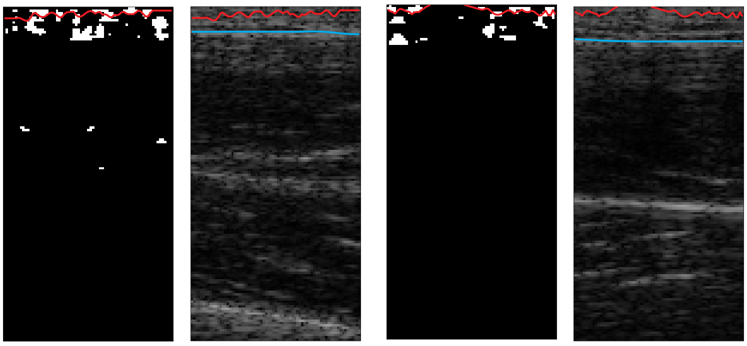
(a) (b)

Figure 4.2: Two examples demonstrate the segmentation results of σ_s^2 on participants with fat thickness ≤5mm. Ultrasound data is obtained using a single focus positioned at 25mm. In subfigures (a) and (b), the left image is the binary image of σ_s^2 and the right image is the B-mode image. The cyan boundary is the manual segmentation and the red boundary is the automatic segmentation.

4.2 Evaluation of Segmentation

Results between the manual and automatic segmentation are evaluated in this section. First, we show the mean thickness results of σ_s^2 and IBS obtained from using a single focus positioned at 25mm and investigate if IBS is an appropriate parameter for locating the fat boundary at various body sites. Secondly, we investigate if there is any improvement in the segmentation result on σ_s^2 using multiple focuses.

4.2.1 Results: Spectrum Variance σ_s^2 vs Integrated Backscattering Coefficient IBS

In this section, we investigate if IBS is an appropriate parameter for locating the fat boundary. The fat boundary, which is fascia, is characterized by strong reflection; however, the heterogeneous texture of fat appears at different anatomical structure and IBS may not be an accurate representation.

4.2.1.1 Correlation

This section shows the correlation of the average thickness between the manual segmentation and automatic segmentation. The Pearson's linear correlation coefficient (r) and the linear regression equation of the data points are shown. The correlation results are analyzed at each body site separately.

For the segmentation with σ_s^2, Figure 4.3 shows that the correlation coefficients r are 0.81, 0.71 and 0.82 at the suprailiac, triceps and thigh sites respectively. In the case of segmentation using IBS, Figure 4.4 shows that the correlation coefficients r are 0.77, 0.14 and -0.20 at the suprailiac, triceps and thigh sites respectively. The results show that there is no correlation between the manual and automatic measurements when using IBS as the spectrum property for segmentation at the triceps and thigh; however, high correlation is found at the suprailiac site.

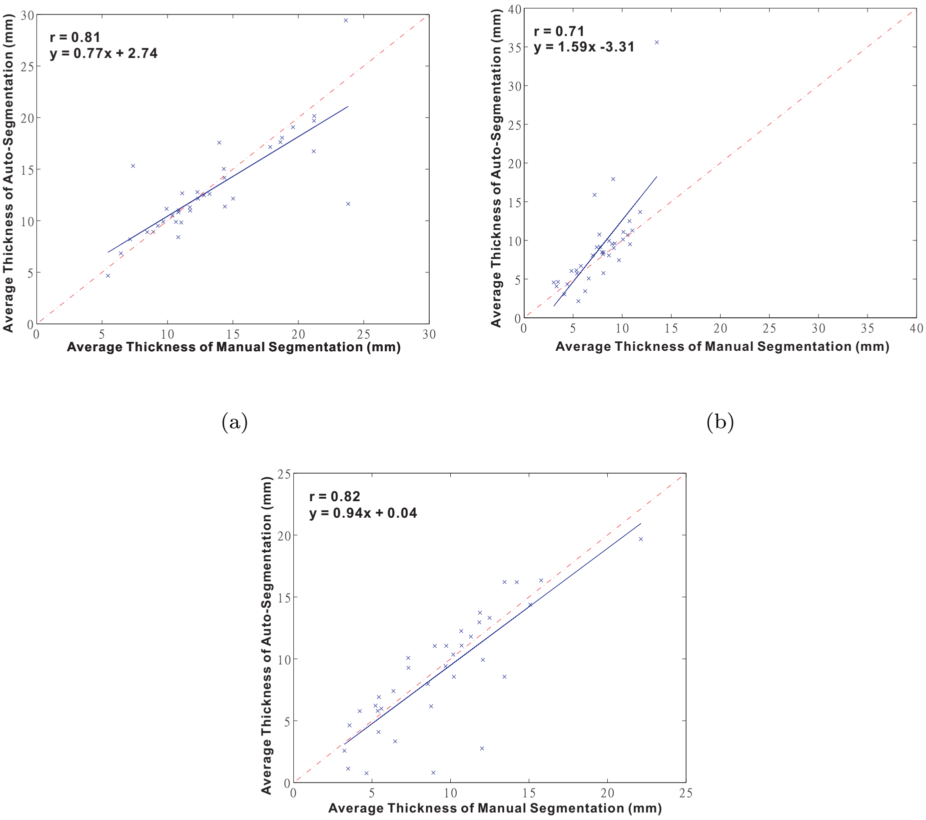

(a) (b)

(c)

Figure 4.3: Correlation between manual and automatic measurements using σ_s^2 at the (a) suprailiac (b) triceps and (c) thigh sites. The red dashed line represents the one-to-one relationship, the blue line is the linear regression line of the 36 samples (blue crosses).

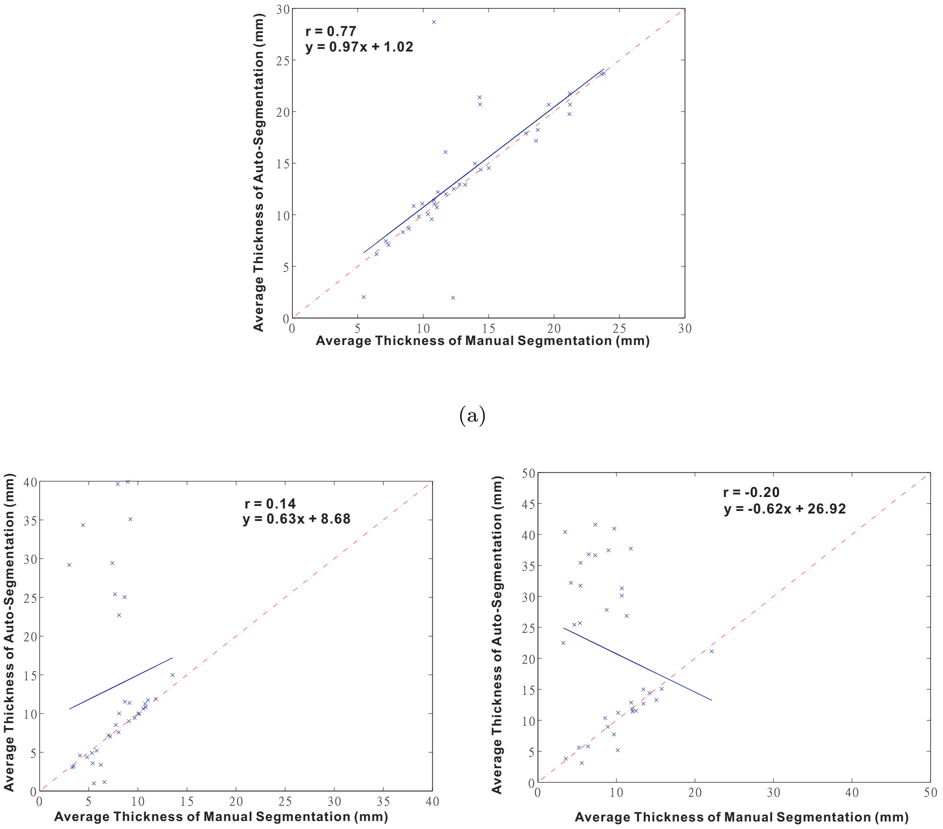

(a)

(b)

(c)

Figure 4.4: Correlation between manual and automatic measurements using IBS at the(a) suprailiac (b) triceps and (c) thigh sites. The red dashed line represents the one-to-one relationship, the blue line is the linear regression line of the 36 samples (blue crosses).

4.2.1.2 d_{ERR}

As discussed in Chapter 3, d_{ERR} represents the average thickness error between the boundaries for the manual and automatic segmentation. For each body site, the paired t-test was conducted to determine whether the mean of d_{ERR} obtained from σ_s^2 is different from that obtained from IBS with a significance level of 0.05.

		d_{ERR} (mm)	Paired t-test		
Body Site	Group	Mean ± SD	t(df=35)	p-value	CI
Suprailiac	σ_s^2	-0.32 ± 2.99	-1.18	0.24	(-2.59, 0.68)
	IBS	0.63 ± 3.95			
Triceps	σ_s^2	1.29 ± 4.30	-2.23	0.032	(-8.62, -0.40)
	IBS	5.80 ± 11.16			
Thigh	σ_s^2	-0.48 ± 2.76	-5.42	0.000005	(-16.92, -7.69)
	IBS	11.82 ± 13.93			

Table 4.1: Average d_{ERR} of 36 samples in 9 subjects (4 samples per participant) at the suprailiac, triceps and thigh sites respectively. The paired t-test is used to compare the mean difference between σ_s^2 and IBS. *t(df=35)*: t-value of the paired t-test with a degree of freedom (df) of 35. *CI*: 95% confidence interval (CI) of the statistical mean difference between σ_s^2 and IBS. If the CI does not include 0, there is a significant difference between groups. *p-value*: if a p-value < 0.05, it indicates there is significant difference between the the d_{ERR} of σ_s^2 and IBS.

Table 4.1 shows the mean and standard deviation of d_{ERR} from σ_s^2 and IBS among 36 samples at each site. The t-values, p-values and confidence intervals that were calculated by the paired t-test between σ_s^2 and IBS are presented. If the p-value < 0.05 and the 95% confidence interval does not include 0, there is a significant difference between groups. Significant differences in d_{ERR} were only found at the triceps and thigh ($p < 0.05$). The comparisons of the d_{ERR} differences between σ_s^2 and IBS are summarized as follows:

1. At all body site, the values of d_{ERR} obtained from σ_s^2 were smaller than that obtained from IBS.

2. Using σ_s^2 as the segmentation parameter, the smallest mean of d_{ERR} was noticed at the suprailiac site(-0.32mm±2.99mm). The thigh had a similar mean of d_{ERR} (-0.48mm±2.76mm) with the suprailiac site. The largest mean of d_{ERR} was noticed at the triceps (1.29mm±4.30mm).

3. Using IBS as the segmentation parameter, the smallest mean of d_{ERR} was also noticed at the suprailiac site (0.63mm±3.95mm). Compared with the result of the suprailiac site, the d_{ERR}

was much higher in the triceps (5.80mm±11.16mm) and thigh (11.82mm ±13.93mm). It indicates that IBS yields higher variance and average value when detecting fat from different participants at the triceps and thigh than the suprailiac site.

4. Significant differences in d_{ERR} between σ_s^2 and IBS were noticed at the triceps (t(df = 35) = -2.23, p = 0.032) and thigh (t(df = 35) = -5.42, p = 0.000005) but not at the suprailiac site(t(df = 35) = -1.18, p = 0.024). The boundaries detected from the IBS property have a significant larger average thickness error than that detected from σ_s^2 at the triceps and thigh, but not at the suprailiac site.

4.2.1.3 d_{RMS}

As discussed in Chapter 3, d_{RMS} represents the root mean square thickness error between the boundaries for the manual and automatic segmentation. For each body site, the paired t-test was conducted to determine whether the mean of d_{RMS} obtained from σ_s^2 is different from that obtained from IBS with a significance level of 0.05.

		d_{RMS} (mm)		Paired t-test	
Body Site	Group	Mean ± SD	t(df=35)	p-value	CI
Suprailiac	σ_s^2	2.00 ± 2.49	−0.03	0.98	(-1.60, 1.55)
	IBS	2.02 ± 3.49			
Triceps	σ_s^2	2.38 ± 3.88	−2.32	0.026	(-8.54, -0.57)
	IBS	6.94 ± 10.50			
Thigh	σ_s^2	2.10 ± 1.90	−4.78	0.000031	(-15.21,-6.14)
	IBS	12.78 ± 13.04			

Table 4.2: Average d_{RMS} of 36 samples in 9 subjects (4 samples per participant) at the suprailiac, triceps and thigh sites respectively. The paired t-test is used to compare the mean difference between σ_s^2 and IBS. *t(df=35)*: t-value of the paired t-test with a degree of freedom (df) of 35. *CI*: 95% confidence interval (CI) of the statistical mean difference between σ_s^2 and IBS. If the CI does not include 0, there is a significant difference between groups. *p-value*: if a p-value < 0.05, it indicates there is significant difference between the the d_{RMS} of σ_s^2 and IBS.

Table 4.2 shows the mean and standard deviation of d_{ERR} obtained from σ_s^2 and IBS among 36 samples at each body site. If the p-value < 0.05 and the 95% confidence interval does not include 0, there is a significant difference between groups. Significant differences in d_{RMS} were only found at the thigh and the triceps ($p < 0.05$) . The comparisons of the d_{RMS} difference between σ_s^2 and IBS are summarized as follows:

1. The d_{RMS} values of the triceps (2.38mm±3.88mm) and thigh (2.10mm±1.90mm) that were obtained from σ_s^2 were smaller than that their values (triceps: (6.94mm±10.50mm) and thigh (12.78mm±13.04mm) obtained from IBS . At the suprailiac site, d_{RMS} obtained from σ_s^2 (2.00mm±2.49mm) was similar than that obtained from IBS (2.02mm±3.49mm).
2. Using σ_s^2 as the segmentation parameter, the smallest mean of d_{RMS} was found at the suprailiac site (2.00mm±2.49mm). The thigh (2.10mm±1.90mm) had a similar mean of d_{RMS} with that of the suprailiac site. Triceps (2.38mm±3.88mm) had the largest d_{RMS} among all body sites.
3. Using IBS as the segmentation parameter, the smallest mean of d_{RMS} was also found at the suprailiac site(2.02mm±3.49mm). This value was similar to the error of σ_s^2 (2.00±2.49mm).
4. Significant differences in d_{RMS} between σ_s^2 and IBS were noticed at the triceps (t(df = 35) = -2.32, p = 0.026)and thigh (t(df = 35) = -4.78, p = 0.000031) only. The boundaries detected from the IBS property have a significant larger root mean square thickness error than that detected from σ_s^2 at the triceps and thigh, but not at the suprailiac site.

4.2.2 Results: Multiple-focuses vs Single Focuses

To investigate whether the application of multiple focuses would improve the segmentation result on σ_s^2, a one-way ANOVA was applied to d_{RMS} and d_{ERR} obtained from the single focus at 25mm(SF), stitching multiple focuses(MF1) and averaging multiple focuses(MF2) respectively. In order to identify difference between groups, Tukey's honestly significant difference (HSD) multi-comparison tests were conducted for the pairwise comparisons between SF and MF1, MF1 and MF2, and SF and MF2. Multiple comparisons were performed using Tukey's method with Matlab function *multcompare.*

4.2.2.1 d_{ERR}

As discussed in Chapter 3, d_{ERR} represents the average thickness error between the boundaries for the manual and automatic segmentation. For each body site, the one-way ANOVA test was first conducted to determine whether the mean differences of d_{ERR} among SF, MF1 and MF2 are significantly different with a significance level of 0.05. Table 4.3 summarizes the results of the one-way ANOVA tests.

		d_{ERR} (mm)	One-Way ANOVA	
Body Site	Group	Mean ± SD	F(2,105)	p-value
Suprailiac	SF	-0.32 ± 2.99	0.08	0.92
	MF1	-0.63 ± 5.76		
	MF2	-0.30 ± 2.30		
Triceps	SF	1.29 ± 4.30	5.21	0.0069
	MF1	-1.79 ± 5.58		
	MF2	0.80 ± 2.63		
Thigh	SF	-0.48 ± 2.76	0.02	0.82
	MF1	-0.75 ± 6.79		
	MF2	-0.09 ± 2.23		

Table 4.3: Average d_{ERR} of 36 samples in 9 subjects (4 samples per participant) at the suprailiac, triceps and thigh sites respectively. The one-way ANOVA test is used to compare the mean difference among results obtained from the SF, MF1 and MF2. *F(2,105)*: F-value of the one-way ANOVA test with a between-groups degree of freedom of 2 and a within-group degree of freedom of 105. *p-value*: if a p-value < 0.05, it indicates there is a significant difference among the groups.

Body Site	Group A	Group B	mean difference (mm)	95% CI (mm)
Suprailiac	SF	MF1	0.32	(-1.95, 2.59)
	SF	MF2	-0.01	(-2.28, 2.26)
	MF1	MF2	-0.33	(-2.60, 1.94)
Triceps	SF	MF1	3.08	(0.64, 5.52)†
	SF	MF2	0.49	(-1.94, 2.93)
	MF1	MF2	-2.58	(-5.02, -0.15)†
Thigh	SF	MF1	0.26	(-2.21, 2.74)
	SF	MF2	-0.39	(-2.87, 2.09)
	MF1	MF2	-0.65	(-3.13, 1.82)

† 95% confidence interval does not include 0; therefore, there is a significant difference between groups A and B.

Table 4.4: Tukey's HSD multiple comparisons for the difference in d_{ERR} within a group. SF: single focus at 25mm, MF1: stitching multiple focuses and MF2 averaging multiple focuses. *mean difference*: the estimated statistical mean difference from the Tukey's HSD test. *CI*: 95% confidence interval of the statistical mean difference between groups A and B.

Table 4.3 shows the mean and standard deviation value of d_{ERR} from SF, MF1 and MF2 among 36 samples at each body site. If the 95% confidence interval does not include 0, there is a significant difference between group A and B. Significant differences in d_{ERR} were only found at the triceps ($p < 0.05$). Multiple comparisons were then performed between SF and MF1, SF and MF2, and MF1 and MF2 at each body site. Table 4.4 presents the results of multiple comparions in terms of the statistical mean difference and the 95% confidence interval. If the confidence interval does not contain 0, the difference between two groups is significant. If the confidence interval contains 0.0, the difference between two groups is insignificant. Comparisons of d_{ERR} among SF, MF1 and MF2 are summarized as follows:

1. MF1 had the largest mean and standard deviation of d_{ERR} at all body sites. Its values of d_{ERR} were (-0.63±5.76)mm at the suprailiac site, (0.80±2.63)mm at the triceps and (-0.75±6.79)mm at the thigh.

2. MF2 had the smallest mean and standard deviation of d_{ERR} at all body sites. Its values of d_{ERR} were (-0.30±2.30)mm at the suprailiac site, (0.80±2.53)mm at the triceps, and (-0.09±2.23)mm at the thigh.

3. Significant differences were found between SF and MF1 (CI = (0.64,5.52)), and MF1 and MF2 (CI = (-5.02,-0.15)) at triceps (F(2,105) = 5.21, p = 0.0069) only. In both cases, MF1 had a worse d_{ERR} than SF and MF2.

4. Although the differences between SF and MF2 were insignificant at the suprailiac (CI = (-2.28,2.26)), triceps (CI = (-1.94,2.93)) and thigh (CI = (-5.02,0.15)) sites, there were improvements on d_{ERR} from using MF2 over SF at all body sites. The values of d_{ERR} were improved from (-0.32±2.99)mm to (-0.30± 2.30)mm at the suprailiac site; (1.29±4.30)mm to (0.80±2.63)mm at the triceps, and (-0.48±2.76)mm to (-0.09±2.23)mm at the thigh.

4.2.2.2 d_{RMS}

As discussed in Chapter 3, d_{RMS} represents the root mean square thickness error of between the boundaries between the manual and automatic segmentation. For each body site, the one-way ANOVA test was first conducted to determine whether the mean differences of d_{RMS} among SF, MF1 and MF2 are significantly different with a significance level of 0.05. Table 4.5 summarizes the results of the one-way ANOVA tests.

Table 4.5 shows the mean and standard deviation value of d_{RMS} obtained from SF, MF1 and MF2 among 36 samples at each body site. If the 95% confidence interval does not include 0, there is a significant difference between group A and B. A significant difference in d_{RMS} was only

		d_{RMS} (mm)	One-Way ANOVA	
Body Site	Group	Mean ± SD	F(2,105)	p-value
Suprailiac	SF	2.00 ± 2.49	1.74	0.18
	MF1	2.95 ± 5.04		
	MF2	1.42 ± 2.05		
Triceps	SF	2.38 ± 3.88	2.27	0.11
	MF1	3.71 ± 4.62		
	MF2	1.94 ± 2.07		
Thigh	SF	2.10 ± 1.90	3.68	0.029
	MF1	3.89 ± 5.68		
	MF2	1.78 ± 1.46		

Table 4.5: Average d_{RMS} of 36 samples in 9 subjects (4 samples per participant) at the suprailiac, triceps and thigh sites respectively. The one-way ANOVA test is used to compare the mean difference among results obtained from the SF, MF1 and MF2. *F(2,105)*: F-value of the one-way ANOVA test with a between-groups degree of freedom of 2 and a within-group degree of freedom of 105. *p-value*: if a p-value < 0.05, it indicates there is a significant difference among the groups.

found obtained at the thigh ($p < 0.05$). Multiple comparisons were then performed between SF and MF1, SF and MF2, and MF1 and MF2 at each body site. Table 4.6 presents the results of multiple comparions in terms of the statistical mean difference and the 95% confidence interval. If the confidence interval does not contain 0, the difference between two groups is significant. If the confidence interval contains 0.0, the difference between two groups is insignificant. We summarize the results when multiple comparing d_{RMS} among the methods of SF, MF1 and MF2:

1. Among all methods, MF1 resulted in the largest mean and standard deviation of d_{RMS} at all body sites. The values of d_{RMS} were (2.95±5.04)mm at the suprailiac sites, (3.71±4.62)mm at the triceps and (3.89±5.68)mm at the thigh.

2. Among all methods, MF2 had the smallest average and standard deviation of d_{RMS} at all body sites. The values of d_{RMS} were (1.42±2.05)mm at the suprailiac site, (1.94±2.07)mm at the triceps and (1.78±1.46)mm at the thigh. Compared with different body sites, the average value was lowest at the suprailiac area and the standard deviation was the lowest at the thigh.

3. A significant difference of d_{RMS} between MF1 and MF2 was only noticed at the thigh (CI = (0.12, 4.11)). The mean value of d_{RMS} obtained from MF2 (1.78±1.46)mm is significantly smaller than that of MF1 (2.10±1.90)mm. Although there was no significant difference of d_{RMS} between MF1 and MF2 at the triceps (F(2,105) = 2.27, p = 0.11, CI = (-0.29,3.84)),

Body Site	Group A	Group B	mean difference (mm)	95% CI (mm)
Suprailiac	SF	MF1	-0.92	(-2.88, 1.05)
	SF	MF2	0.62	(-1.35, 2.58)
	MF1	MF2	1.53	(-0.43, 3.50)
Triceps	SF	MF1	-1.33	(-3.40, 0.73)
	SF	MF2	0.44	(-1.62, 2.51)
	MF1	MF2	1.78	(-0.29, 3.84)
Thigh	SF	MF1	-1.79	(-3.79, 0.20)
	SF	MF2	0.32	(-1.68, 2.31)
	MF1	MF2	2.11	(0.12, 4.11)†

† 95% confidence interval does not include 0; therefore, there is a significant difference between groups A and B.

Table 4.6: Tukey's HSD multiple comparisons for the difference in d_{RMS} within a group. SF: single focus at 25mm, MF1: stitching multiple focuses and MF2 averaging multiple focuses. *mean difference*: the estimated statistical mean difference from the Tukey's HSD test. *CI*: 95% confidence interval of the statistical mean difference between groups A and B.

this showed a trend toward significance.

4. There was no significant difference of d_{RMS} between SF and MF2 at all body sites. Nevertheless, there are improvements on the mean and standard deviation of d_{RMS} over SF by using MF2 at all body sites. The values of d_{RMS} were improved from (2.00±2.49)mm to (1.42±2.05)mm at the suprailiac site; (2.38±3.88)mm to (1.94±2.07)mm at the triceps and (2.10±1.90mm) to (1.78±1.46)mm at the thigh.

5. No significant difference was noticed between SF and MF1 at all body sites(CI = (-2.88,1.05) at the suprailiac site, CI = (-3.40,0.73) at the triceps and CI = (-3.79, 0.20) at the thigh). However, the value of d_{RMS} obtained from SF is smaller than that of MF1 at all body sites. The values of d_{RMS} were decreased from (2.95±5.04)mm to (2.00±2.49)mm at the suprailiac site; (3.71±4.62)mm to (2.38±3.88)mm at the triceps and (3.89±5.68) to (2.10±1.90mm) at the thigh.

4.2.3 Discussions

We showed that the segmentation with σ_s^2 (obtained from a single focus at 25mm) was a feasible technique to detect the location of the fat boundary at the suprailiac, triceps and thigh sites. However, outliers were observed in the linear correlation plots (Figure 4.3) at all such sites. Although there was high correlation between the manual measurement and automatic measurement using σ_s^2, the presence of outliers indicated that σ_s^2 only provided a coarse estimation on the area of fat tissue and was affected by the variation in tissue structures of samples.

The evaluations on segmentation with σ_s^2 using a single focus at 25mm showed similar errors at the suprailiac and thigh sites. The d_{ERR} and d_{RMS} were (-0.32±2.99)mm and (2.00±2.49)mm at the suprailiac site, and (-0.48±2.76)mm and (2.10±1.90)mm at the thigh. The worst result was shown at the triceps where d_{ERR} was (1.29±4.30)mm and the d_{RMS} was (2.38±3.88)mm. We believe that the reason for the worst results at the triceps was the presence of denser and thicker fibrous of connective tissue there. Earlier, Bellisari *et al.* [33] also reported the worst technical error was found in the triceps site in females.

Moreover, the results of segmentation with σ_s^2 are degraded when the fat thickness is too thin. This is because a smaller amount of fat tissue is present between the fascia and the skin while dense connective tissue is present. Roche [13] also reported that it was harder to define the boundary between the subcutaneous fat and muscle in ultrasound B-mode images due to the presence of smaller amounts of intermuscular fat tissue. In our experiment, participants had the smallest mean and range of fat thickness at the triceps (Table 4.7), this is another reason for why the largest d_{ERR} and d_{RMS} errors are noticed at the triceps.

Reference Thickness (mm)	Suprailiac	Triceps	Thigh
mean±SD	13.34 ± 4.91	7.76 ± 2.56	9.05 ± 4.18
minimum	5.45	3.03	3.24
maximum	23.82	13.53	22.13

Table 4.7: Summary on reference average thickness of subcutaneous fat collected from 9 participants with 4 samples for each person at each body site. The reference thickness is obtained by manual segmentation on ultrasound data.

A subcutaneous fat boundary is characterized by strong reflection; however, we observed that it was not reliable to use IBS to locate the fat boundary at the thigh and triceps but it was feasible to detect the fat boundary at the suprailiac site. Referring to Figures 4.4(b) and 4.4(c) of the triceps and thigh, we noticed that outliers were mostly located in a deeper area. This is because strong echoes can be generated not only by the fibrous connective tissues within the fat layer, but also by structures like tendons and bones. Our results show that there was no correlation between the manual and automatic measurements when using the IBS property at the triceps and thigh. Further, we discovered that IBS could be used as a segmentation factor at the suprailiac site because fat is more homogeneous there than at the triceps and thigh. There are no structures with strong echoes like tendon and bone around this anatomical site, and fewer and thinner fibrous connective tissue are found there (as shown in Figure 4.5). No significant differences in d_{ERR} and d_{RMS} were noticed between segmentation with σ_s^2 and IBS among the 36 samples at the suprailiac site.

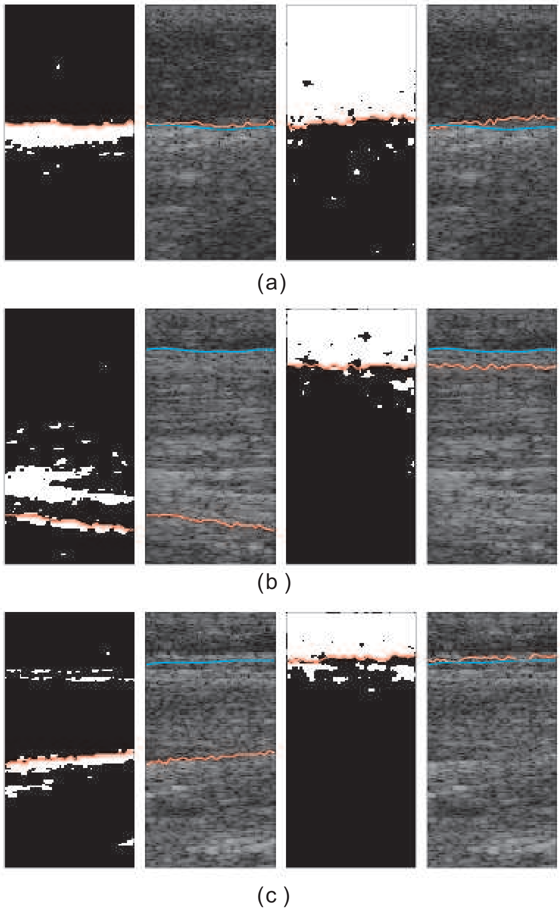
(a)

(b)

(c)

Figure 4.5: Show the results of IBS and σ_s^2 at the (a) suprailiac, (b) thigh and (c) triceps sites. IBS is not reliable in locating the fat boundary at the thigh and triceps because of the presence of other soft tissues with strong reflection. In subfigures (a),(b) and (c), from left to right: binary map from IBS, segmentation result from IBS, binary map from σ_s^2 and segmentation result from σ_s^2. The cyan boundary is the manual segmentation and the red boundary is the automatic segmentation.

The effect of using multiple focuses to improve results was investigated because we assumed that thicknesses could be different among people and a focus at a fixed position might not be appropriate for all thicknesses. Our statistical analysis showed that there was no significant benefit in using multiple focuses over a single focus, although we found that averaging σ_s^2 with multiple focuses smoothed the value of σ_s^2 and tended to report smaller values of d_{ERR} (-0.32mm±2.99)mm vs (-0.30±2.30)mm at suprailiac sites, (1.29±4.30)mm vs (0.80±2.63)mm at the triceps and (-0.48±2.76)mm vs (-0.09±2.23)mm at the thigh and d_{RMS} (2.00±2.49)mm vs (1.42±2.05)mm at the suprailiac,(2.38±3.88)mm vs (1.94±2.07)mm at the triceps and (2.10±1.90)mm vs (1.78±1.46)mm at the thigh, whereas stitching σ_s^2 with multiple focuses degraded the segmentation quality especially in the presence of fibrous tissues.

Moveover, Bellisari *et al.* [33] evaluated the inter-observer technical errors of manual ultrasound measurements and found that the absolute technical errors were 0.15mm at the suprailiac site, 0.62mm at the triceps site and 0.13mm at the mid-thigh site. Our absolute mean values of d_{ERR} obtained at multiple focuses are close to their technical error. The mean values of d_{ERR} were –0.30mm at the suprailiac , 0.80mm at the triceps and -0.09 at the thigh sites. Similarly, both of our results showed that the worst error was found at the triceps site.

From our visual investigation, we noticed that the thresholding result of σ_s^2 captured with a single focus occasionally underestimated the area of fat tissue. It happened when the surface of the fascia was not well-defined and fibrous tissues appeared near the fascia (as shown in Figures 4.6 to 4.8). As a result, a fat layer with significant holes and boundary gaps appeared in the binary map of σ_s^2 obtained with a single focus (Figure 4.6(a)). However, the gap was annihilated in the binary map at Figure 4.6(c) after averaging σ_s^2 captured from multiple focuses. Figure 4.7 shows a case where a thin layer of fibrous tissue appeared near the top right of the fascia. Averaging the binary map of σ_s^2 with multiple focuses reduced the gap near the fat boundary and corrected the location of the boundary detected. Figure 4.8 shows another case that benefited from averaging σ_s^2 with multiple focuses. As shown in the B-mode image, an obvious layer of fibrous tissue is found within the layer of fat and the resulting binary map (Figure 4.8(a)) obtained with a single focus was incorrect. The averaging technique was less sensitive to noise and thick fibrous connective tissue, and the detection of the fat boundary from the binary map was therefore improved.

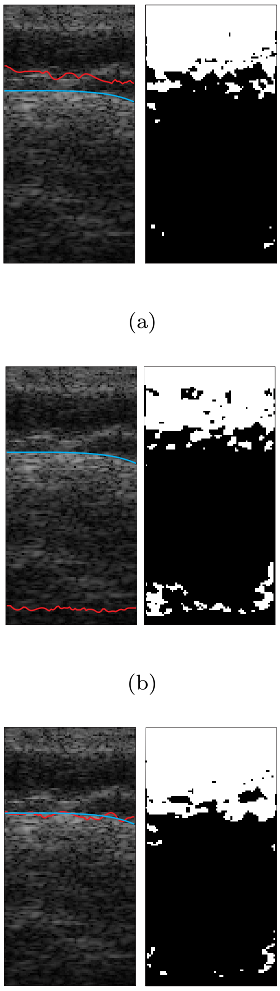

(a)

(b)

(c)

Figure 4.6: An example showing the improvement of using MF2 over SF and MF1. In subfigures (a) SF,(b) MF1 and (c) MF2, from left to right: binary map of σ_s^2 and, segmentation result of σ_s^2. The cyan boundary is the manual segmentation and the red boundary is the automatic segmentation.

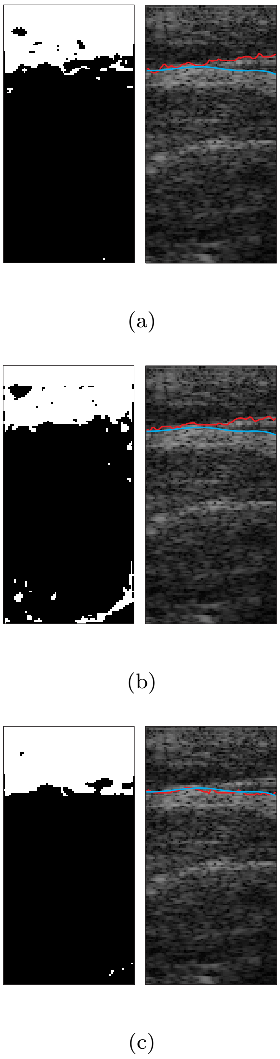

(a)

(b)

(c)

Figure 4.7: An example showing the improvement of using MF2 over SF and MF1. In subfigures (a) SF,(b) MF1 and (c) MF2, from left to right: binary map of σ_s^2 and, segmentation result of σ_s^2. The cyan boundary is the manual segmentation and the red boundary is the automatic segmentation.

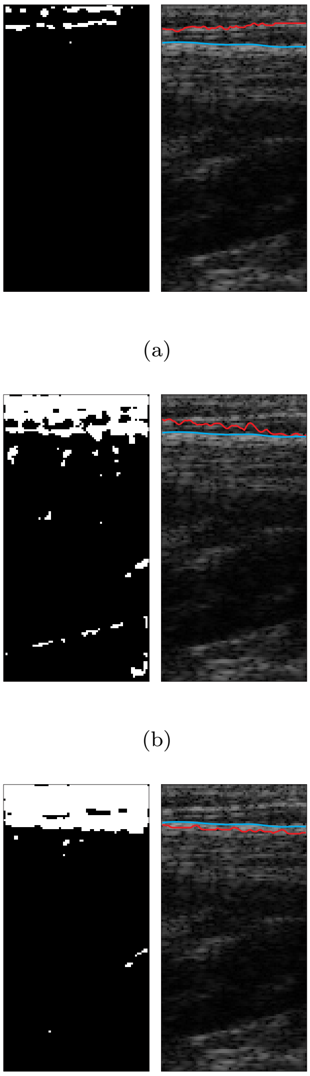

(a)

(b)

(c)

Figure 4.8: An example showing the improvement of using MF2 over SF and MF1. In subfigures (a) SF,(b) MF1 and (c) MF2, from left to right: binary map of σ_s^2 and segmentation result of σ_s^2 at a triceps. The cyan boundary is the manual segmentation and the red boundary is the automatic segmentation.

In addition, we found that the method of stitching spectrum properties with multiple focuses (MF1) resulted in statistically higher values of d_{RMS} (at the thigh) and d_{ERR} (at the triceps) than using single focus (SF) and averaging multiple focuses (MF2). The idea of stitching the values of a spectrum property at each focus was to improve the detail representation of the spectrum property. However, the presence of extraneous membranes within the fat tissue interfered with the value of σ_s^2 randomly. Stitching values from multiple focuses exaggerated unwanted details and caused errors in thresholding. On the other hand, averaging the spectrum values obtained from multiple focuses could smooth out the irregularities and improve the ability to find the global change in thresholding. Although its result did not appear statistically worse at the suprailiac site than the other two methods, we suggest that this may be due to the fact that the structure of subcutaneous fat is different in various body sites. From visual observation, it was noticed that fewer fibrous tissues were seen at the suprailiac site than at the triceps and thigh sites. The idea of stitching the values of a spectrum property at each focus was to improve the detail representation of the spectrum property. However, the presence of extraneous membranes within the fat tissue interfered with the value of σ_s^2 randomly. Stitching values from multiple focuses exaggerated unwanted details and caused errors in thresholding. On the other hand, averaging the spectrum values obtained from multiple focuses could smooth out the irregularities and improve the ability of finding the global change in thresholding.

In the evaluation, we used both the mean thickness error d_{ERR} and the root mean square error d_{RMS} as the indicator for the segmentation errors because positive and negative y-coordinate values can cancel in d_{ERR} but not in d_{RMS}. The average thickness errors d_{ERR} at the suprailiac, triceps and thigh sites were close to 0mm ($<$ 1mm at all body sites when using the MF2 method). However, the d_{RMS} were all larger than the d_{ERR} at all body sites. This implies that averaging the boundary points over the lateral direction reduces the uncertainty of the boundary measurement when we are only interested in the average thickness measurement of the fat layer. If we want to represent the boundary in both axial and lateral direction, the uncertainty of the boundary is higher than the averaged boundary thickness.

Overall, we found that it was more difficult to detect the threshold when the fat layer was thin or in the presence of thicker, extraneous fibrous membranes. If a fat layer was homogeneous with less and thinner fibrous membranes, our method would be more robust as σ_s^2 was less noisy;

however, if fibrous membranes appear in the middle of a homogeneous layer, σ_s^2 was interfered with and changed randomly. The structure of the fat tissue is the main factor of the efficiency of the segmentation.

4.3 Comparison of Auto-detected Fat Thickness with Skinfold Caliper Measurements

In section 4.2, we evaluated the segmentation result in terms of d_{ERR} and d_{RMS} and concluded that the combination of MF2 and σ_s^2 yielded the best result. Therefore, we will use 18 samples in nine participants (two sets per participant) of automatic ultrasound measurements from this combination for nine human participants to compare with the measurements using skinfold calipers in this section. Since the investigator was new to the use of the skinfold caliper, an evaluation of her skinfold caliper technique is first presented. Furthermore, the manual and automatic ultrasound measurements are compared with the half of the skinfold thicknesses ($\frac{1}{2}$ skinfold thicknesses). The $\frac{1}{2}$ skinfold thicknesses is used because the skinfold caliper measures a fold of skin that comprises two layers of subcutaneous fat. The relationship between the ultrasound and $\frac{1}{2}$ skinfold caliper measurements is investigated using linear correlation. After that, the mean difference values between the two techniques are presented.

4.3.1 Evaluation on Skinfold Caliper Technique

A skinfold caliper operator is considered proficient if consistent measurements are made at the same spot. Therefore, we evaluated the skinfold caliper technique of the student investigator by checking the discrepancy of measurements that were repeated at a body site. After training and practice, a test was performed on three participants at the suprailiac, triceps and thigh sites. A mark was first placed at a body site. In the first trial, three skinfold measurements were taken and averaged to obtain an average thickness of the trial. At an interval of 15 minutes, another three measurements were recorded and averaged. A total if 5 trials were executed. Water content of subcutaneous fat changes in time and this may affect the magnitude of the skinfold caliper measurements; therefore, the measurements were taken at the same time of the day at relatively short 15 minute intervals.

Table 4.8 presents the justification results in terms of the discrepancy within a trial and the

Site	Participant	Average Thickness (mm)	Average Discrepancy within a trial (mm)	Average Discrepancy from 5 trials (mm)
Suprailiac	1	6.4	0.2	0.4
	2	23.0	0.4	0.7
	3	24.1	0.5	1.8
Triceps	1	6.2	0.2	1.2
	2	18.7	0.5	0.6
	3	11.8	0.2	1.1
Thigh	1	6.6	0.3	1.1
	2	29.1	0.8	1.0
	3	6.9	0.2	0.6
Overall Median in discrepancy			0.3	1.0

Table 4.8: Discrepancies in skin-fold caliper measurement taken at the same spot of a body site.

discrepancy of average thickness from five trials. The discrepancy within a trial is the standard deviation value for the three thickness measurements in the trial. The discrepancy from 5 trials is the standard deviation value for the averaged thickness from 5 trials. The average discrepancy within a trial is from 0.2mm to 0.8mm with a median at 0.3mm. Average discrepancy from five trials ranged from 0.4mm to 1.8mm with a mean of 1.0mm.

The above results are acceptable because the median in discrepancy within a single trial was 0.3mm that was within the instrument error of the caliper (i.e. ±0.5mm). Furthermore, the median in discrepancy from five trials was 1.0mm that was higher than the error of a single trial. This result was reasonable because there were more variations between independent trials and the resulting error still fell at the limit of the caliper resolution (i.e. 1.0mm).

4.3.2 Result of Correlation

The average thickness of the ultrasound boundary is compared to that established by the $\frac{1}{2}$ skinfold measurements. Correlation between $\frac{1}{2}$ skinfold caliper and ultrasound measurements is computed by Pearson's linear coefficient. $\frac{1}{2}$ skinfold caliper measurements are compared with ultrasound measurements obtained from manual segmentation and automatic detection respectively. The linear relationship is presented by both the linear coefficient (r) and the equation of a regression line. Figures 4.9 to 4.11 shows the linear relationship at the suprailiac, triceps and thigh sites respectively. The solid blue line shows the linear relationship between caliper measurement and ultrasound measurement, and the dotted blue line represents an one-to-one relationship. The mean values, linear coefficient and equation of regression line for the three subcutaneous fat measurements obtained by skinfold caliper and ultrasound techniques are summarized in Tables 4.9 to 4.10.

As observed in the case of manual segmentation vs $\frac{1}{2}$ skinfold caliper measurement, high correlations are found at the suprailiac ($r = 0.93$), triceps ($r = 0.86$) and thigh ($r = 0.87$) sites. The correlation coefficients r are smaller in the case of automatic detection vs $\frac{1}{2}$ skinfold caliper measurement and the values are 0.90, 0.72 and 0.89 at the suprailiac, triceps and thigh sites respectively. Automatic detection gives a smaller value of r at the suprailiac site and triceps but a larger value at the thigh.

Site	Caliper (mm)	Ultrasound (mm)	r	Linear Relationship
Suprailiac	12.08 ± 5.17	13.39 ± 5.03	0.93∗	y = 0.90x + 2.47
Triceps	5.78 ± 1.92	7.81 ± 2.34	0.86∗	y = 1.05x + 1.74
Thigh	10.14 ± 4.56	9.73 ± 4.63	0.87∗	y = 0.88x + 0.83

*p < 0.0001

Table 4.9: The correlation coefficient r of average thickness between the manual ultrasound segmentation vs $\frac{1}{2}$ skinfold caliper measurements for 18 samples in nine participants (two samples per participant).

Site	Caliper (mm)	Ultrasound (mm)	r	Linear Relationship
Suprailiac	12.08 ± 5.17	12.81 ± 3.85	0.90∗	y = 0.78x + 4.00
Triceps	5.78 ± 1.92	8.59 ± 2.62	0.72†	y = 0.99x + 2.84
Thigh	10.14 ± 4.56	9.38 ± 5.12	0.89∗	y = 1.00x - 0.74

*p < 0.0001,
†p < 0.001

Table 4.10: The correlation coefficient r of average thickness between the automatic ultrasound segmentation vs $\frac{1}{2}$ skinfold caliper measurements for 18 samples in nine participants (two samples per participant).

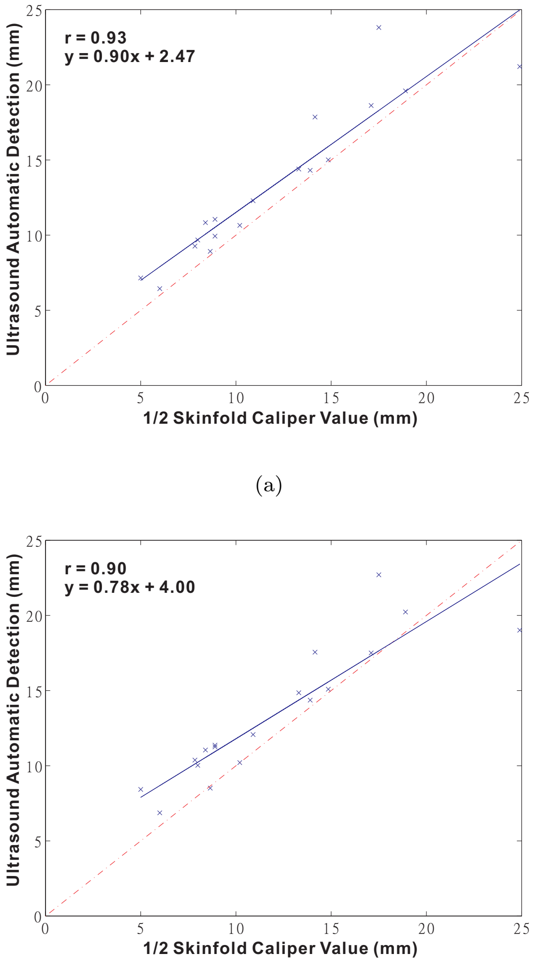

(a)

(b)

Figure 4.9: The relationship of the average thickness between the ultrasound and the skinfold measurements at the suprailiac site: (a) manual ultrasound detection vs $\frac{1}{2}$ skinfold (b) automatic ultrasound detection vs $\frac{1}{2}$ skinfold.

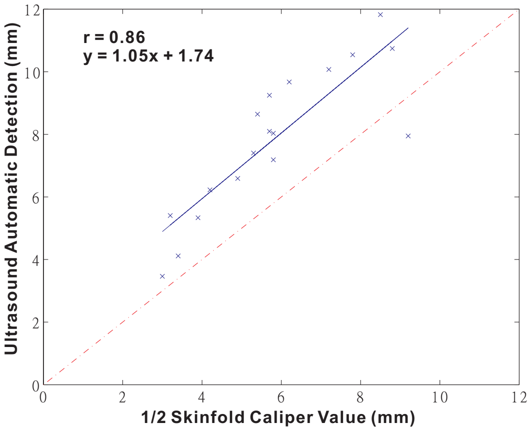

(a) Manual Ultrasound Detection vs $\frac{1}{2}$ skinfold

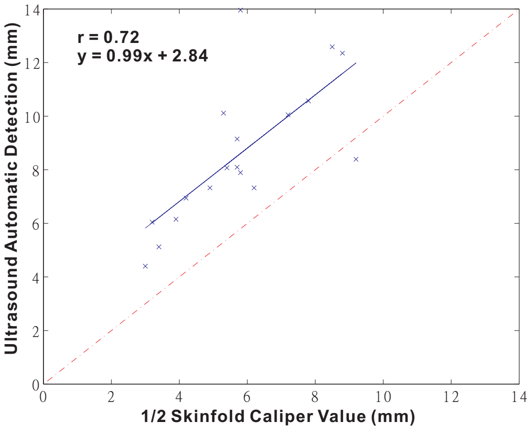

(b) $\frac{1}{2}$ skinfold vs Automatic Detection

Figure 4.10: The relationship of the average thickness between the ultrasound and the skinfold measurements at the triceps : (a) manual ultrasound detection vs $\frac{1}{2}$ skinfold (b) automatic ultrasound detection vs $\frac{1}{2}$ skinfold.

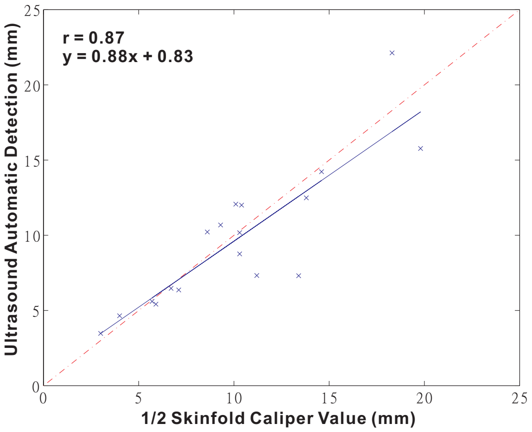

(a) Manual Ultrasound Detection vs $\frac{1}{2}$ skinfold

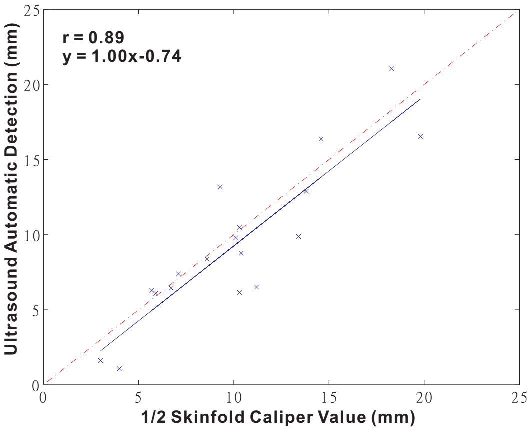

(b) $\frac{1}{2}$ skinfold vs Automatic Detection

Figure 4.11: The relationship of the average thickness between the ultrasound and the skinfold measurements at the thigh: (a) manual ultrasound detection vs $\frac{1}{2}$ skinfold (b) automatic ultrasound detection vs $\frac{1}{2}$.

4.3.3 Result of Difference Against Mean

To assess the inter-method differences (i.e. skinfold caliper and ultrasound measurements), the mean differences between the methods are calculated. Since we do not know the true value of fat thickness, difference against mean helps us to investigate the possible relationship between the measurement error and the true value [87] as discussed in Section 3.3.3. For each data set, the difference is computed between the skinfold thickness and ultrasound thickness. The mean difference ($\overline{D}$) and standard deviation of differences (s) are computed.

For both manual and automatic methods, the largest mean difference is noticed at the triceps.

The magnitude of mean difference for the automatic method is slightly higher (<1mm) than that for the manual method at all sites. The automatic measurements give a higher standard deviation of difference (s) than the manual measurements.

Body site	Manual Measurement		Automatic Measurement	
	$\overline{D}(mm)$	s	$\overline{D}$	s(mm)
Suprailiac	−1.31	1.94	−0.73	2.62
Triceps	−2.03	1.21	−2.81	1.81
Thigh	0.41	2.39	0.76	2.33

Table 4.11: Mean difference and standard deviation values between the ultrasound measurements and the $\frac{1}{2}$ skinfold thicknesses. $\overline{D}$ is the mean difference and s is the standard deviation.

4.3.4 Discussions

Our results showed that similar correlation values between the manual ultrasound segmentation vs $\frac{1}{2}$ skinfold caliper measurement, and automatic ultrasound segmentation vs $\frac{1}{2}$ skinfold caliper measurements are noticed at both suprailiac and thigh sites. At the triceps, a lower r was obtained from the automatic detection than from manual detection ($r = 0.86$ vs $r = 0.73$). This is understandable because our segmentation algorithm yields a large error in d_{ERR}. Several researchers [2, 32, 35, 36, 37] have compared the correlation between the manual ultrasound and skinfold measurements at different body sites. Their results are summarized in Table 4.12. Manual ultrasound and skinfold measurements are highly correlated ($r > 0.7$) in past studies except for the study carried out at the suprailiac site by Stevens-Simon *et al.* [37]. This discrepancy may be due to the difficulty in obtaining skinfold caliper measurements at the suprailiac sites of pregnant women. Although we cannot directly compare our correlation value r with that of other researchers because of differences in sample size, age and gender of participants, our results show a high correlation between automatic ultrasound and skinfold caliper measurements. Other researchers using manual ultrasound methods have found that there is also a good correlation between the ultrasound and skinfold methods.

As we could not establish the true value of fat thickness, we investigated the mean difference of average thickness between the skinfold caliper and ultrasound measurements. The manual and automatic ultrasound measurements were compared to skinfold measurements respectively. Improvement of $\overline{D}$ by using automatic segmentation occurs at the suprailiac site. However, the mag-

	Correlation Coefficient r					
		Reference Results				
Body site	Our automatic measurements	Volz and Ostrove [32]	Bullen *et al.* [35]	Fanelli and Kuczmarski [36]	Stevens -Simon [37]	Ramirez [2]
Suprailiac	0.90	0.86	0.85	0.73	0.52	0.84
Triceps	0.72	0.79	0.92	0.81	0.89	0.85
Thigh	0.89	0.73	–	0.87	0.73	–

Table 4.12: A comparison of correlations between ultrasound measurements and skinfold measurements at the suprailiac, thigh and triceps sites in this and past studies. The ultrasound measurements are obtained by automatic segmentation in this study, and by manual segmentation in the above past studies.

nitudes of mean difference are similar (<1mm) between the manual and automatic segmentation at suprailiac, triceps and thigh sites.

It is of interest to note that Ramirez [2] reported differences ($\overline{D} \pm s$) of (1.2±2.75)mm at the suprailiac and (4.1±2.85)mm at the triceps sites. With our automatic method, the difference of (-0.73±2.62)mm at the suprailiac site is similar to Ramirez's results; however, our difference of (-2.81±1.81)mm at the triceps which was different from them. This again indicates that the segmentation results at the triceps is worse than the results at the suprailiac site. There are no reported values at the thigh by Ramirez.

We compared the values established through the manual and automatic ultrasound measurements to the $\frac{1}{2}$ skinfold caliper values. Although we cannot quantify the true thickness of subcutaneous fat, the high degree of correlation show that the automatic measurement is at least as good as the manual method studied by other researchers.

4.4 Summary

We evaluated the automatic ultrasound measurement technique by comparing its results with those from the manual measurements and $\frac{1}{2}$ skinfold caliper measurements. This showed that segmentation with σ_s^2 was a feasible technique to detect the location of the fat boundary at the suprailiac, triceps and thigh sites. However, the robustness of segmentation with σ_s^2 was affected when the thickness of fat was small and when there were fibrous membranes of connective tissues near the fascia. On the other hand, IBS could be used at the suprailiac sites to detect the fat boundary, but not at the triceps and thigh. Although using multiple focuses to average spectrum properties reduced the value of d_{ERR} and d_{RMS} at all three body sites, there was no significant improvement in the results . With the presence of fibrous connective tissue, stitching values from multiple focuses exaggerates unwanted details and causes errors in thresholding. This method did not improve the detection and its result was much worse than simply averaging values from multiple focuses. Since we could not establish the true thickness of fat, we tested the efficiency of automatic ultrasound measurement by comparing its results to those of manual ultrasound and skinfold measurements. We found that the mean difference at the suprailiac site was similar to that established in a previous research; however, our value obtained at the triceps was not similar. This was understandable because the automatic segmentation result obtained from the triceps was the worst among all sites.

Chapter 5

Conclusions and Future Directions

5.1 Summary and Conclusion

This thesis explored the use of ultrasound to automatically detect the boundary of subcutaneous fat in vivo. We discovered that the variance of the spectrum (σ_s^2) and the integrated backscatter coefficient (IBS) carried information related to the properties of subcutaneous fat. We encoded the values of σ_s^2 and IBS into separate gray-intensity parametric images, and show that σ_s^2 represents a coarse area of the subcutaneous fat tissue and IBS represents possible locations of the fascia. Then, we presented a framework to detect human subcutaneous fat in vivo by using the information of σ_s^2 and IBS. A user study of nine participants was carried out to evaluate our segmentation method at the suprailiac, triceps and thigh sites.

Our subcutaneous fat detection framework consists of four main steps: data capture, calculation of σ_s^2 and IBS from the local spectrum of RF data using STFT and moment analysis, pre-processing of parametric images using spatial compounding and segmentation. Spatial compounding plays a very important role in our framework by reducing noise of the spectrum properties. The non-compounded parametric images of the spectrum properties appear to be noisy because of the speckle texture of ultrasound. In addition, the non-compounded parametric images of σ_s^2 also appear to be erratic in the presence of fibrous connective tissues in the fat tissue. We showed that spatial compounding reduced speckle noise of the parametric images and differentiated the properties of subcutaneous fat. We determined the suitable step size and number of steering angles from the experiment with a homogeneous phantom. In the experiment, we noticed that the signal-to-noise ratio increased when the number of angles increased and the step size increased. This is because more independent data are available. Although increasing the range of angles can improve the overall compounding effect, the area covered by the full compounding effect is reduced as depth increased. In our current approach, spectrum properties obtained from in vivo data were interpolated and averaged with 11 compounding angles at 0°,±2°,±4°,±6° ±8° and ±10°.

After spatial compounding, the visualization of fat using the parametric images of σ_s^2 was improved and the specular boundaries shown in the parametric images of IBS were more continuous. The improvement in σ_s^2 was particularly noticed at the triceps and thigh sites where connective tissues were present in the fat layer and they interfere with the value of σ_s^2. The histogram of the parametric images of σ_s^2 was characterized by a long tail at higher gray levels. The long tail shows that fat pixels change more rapidly than non-fat tissues. The fat pixels also have relatively higher values than the non-fat pixels. We suggested that the relative rapid change in the gray-intensity values of fat pixels was due to the high variation in the tissue structure of subcutaneous fat. This caused high fluctuations in the received spectrum, and this resulted in a more rapid change in the spectrum variance. Moreover, the histogram of the parametric images can be bimodal or unimodal. Using Rosin's thresholding method, we were able to separate the fat and non-fat tissue from σ_s^2 and extracted the possible location of the fascia from IBS. Nevertheless, the IBS also represents other structures with strong echoes such as tendon or bone.

Our user study showed that the segmentation with the parametric images of σ_s^2 was a feasible technique to detect the location of the fat boundary at the suprailiac, triceps and thigh sites. There are two factors affecting the robustness of segmentation using σ_s^2. First, it is harder to detect the fascia boundary when the layer of fat is too thin because the connective tissues and the small amount of fat tissue add uncertainties to the value of σ_s^2. Second, the robustness of the thresholding algorithm decreases in the presence of connective tissues appearing near the fascia. The thresholding algorithm is more robust in homogeneous fat as σ_s^2 appears to be less erratic. In our user study, similar levels of d_{ERR} and d_{RMS} errors were noticed at the suprailiac and thigh sites. The worst result was found at the triceps.

On the other hand, IBS can be used at the suprailiac site to detect the fat boundary, but it is not possible at the triceps and thigh. It is because tendon and bone, which are strong reflectors, can be imaged at the triceps and thigh areas. Our segmentation method could not distinguish them from the IBS.

Our statistical analysis showed no significant improvement in the segmentation results on σ_s^2 when using multiple focuses to average spectrum properties. However, we showed that it reduces the mean thickness errors and root mean square errors when compared to the results obtained from a single focus and it can improve the thresholding results obtained from a single focus when fibrous connective tissue is present close to the surface of the fascia. Testing on 36 samples for each body site, the mean thickness errors d_{ERR} are (-0.30±2.30)mm at the suprailiac site, (0.80±2.63)mm at the triceps and (-0.09±2.23)mm at the thigh, and the root mean square thickness errors d_{RMS} are (1.42±2.05)mm at the suprailiac site, (1.94±2.07)mm at the triceps and (1.78±1.46)mm at the thigh. We also found that our mean values of d_{ERR} were close to the inter-observer technical errors of manual ultrasound measurements performed by Bellisari *et al.* [33]. They found that the absolute technical errors were 0.15mm at the suprailiac site, 0.62mm at the triceps site and 0.13mm at the mid-thigh site. Similarly, both of our results showed that the worst error was found at the triceps site.

The segmentation results on σ_s^2 obtained by averaging multiple focuses were compared to those using skinfold caliper measurements. As we did not know the absolute true value of fat thickness, comparisons were based on the correlation and the mean difference values. High correlation was noticed between the skinfold caliper values and those obtained via the manual and automatic ultrasound. When our automatic detection results were compared with the results using skinfold caliper measurements, we found that there was a high correlation between the two methods and the correlation values were 0.90, 0.72 and 0.89 at the suprailiac, triceps and thigh sites respectively. The correlation appeared lowest at the triceps; however, higher and similar correlations were found at the suprailiac and thigh sites. Our results showed a high correlation between ultrasound and skinfold caliper measurements, which were similar to other researchers' results. Moreover, the magnitudes of mean difference were similar (< 1mm) when comparing the manual and automatic segmentation. The results indicates that there is a high correlation between our ultrasound measurements and our the skinfold measurements.

Although the structure of human subcutaneous fat varies in different body sites and human, our work showed that spatial compounded parametric images of ultrasound RF spectrum properties can be used to segment the subcutaneous fat layer at the suprailiac, triceps and thigh sites of nine human participants. From the histograms of the parametric images of the spectrum variance, we noticed that the gray-intensity value of fat pixels is higher than that of the non-fat tissues and it changes more rapidly than those of other tissue layers. We also suggested that this relative rapid change is due to the fat tissue being composed of two structures with very different acoustic properties: the fat cells and fibrous connective tissue. Based on our visual observation on the parametric images of the spectrum variance, the segmentation algorithm using the thresholding and RANSAC boundary detection was designed to extract the subcutaneous fat and to calculate the average fat thickness. The main contribution of this work is that an automated technique for determining the human subcutaneous fat layer using clinical ultrasound has been developed and applied to the human suprailiac, thigh and triceps *in vivo*. Our evaluations with the skinfold caliper measurements gave comparable results with the manual ultrasound measurements previously studied.

5.2 Future directions

The current subcutaneous fat segmentation technique depends in part on the transducer positioning skills of the operator. For instance, the operator has to position the transducer upright to the skin for maximum reflection from the fascia, and must avoid compression of the fat through observation of the B-mode images. Moreover, the operator must avoid arched surfaces by experimenting with different body locations that allow easy placement of the transducer. A transducer with a smaller footprint may be a better way to solve the above problems as it covers a smaller skin area. However, the tradeoff is the decrease in field of view of the transducer.

The spectrum variance σ_s^2 is more sensitive to the thick, long fibrous connective tissues located in particular near the fascia and when the fat layer is too thin. Therefore, further investigation should be made to reduce the impact of analysis errors by averaging the error effect with a large number of analyzed images. Fibrous connective tissues dispersed within the fat tissues appear shorter in length, smaller in volume and less continuous than the fascia which is a continuous sheet of tissue. Viewing shorter and less continuous tissue at different angles or positions will generate different appearances. In our current spatial compounding technique, the direction of beam steering is parallel to the image plane and the average spectrum properties are only averaged in one plane. However, if we translate the transducer in the direction parallel to the skin (Figure 5.1), we can average spectrum properties from adjacent plans and smooth out the effect of fibrous connective tissues. This idea is similar to the 3D freehand ultrasound. Moreover, this idea can be extended to volumetric measurement of subcutaneous fat.

Further, the experiment is conducted with the ultrasound frequency at 6.6MHz and the thickest

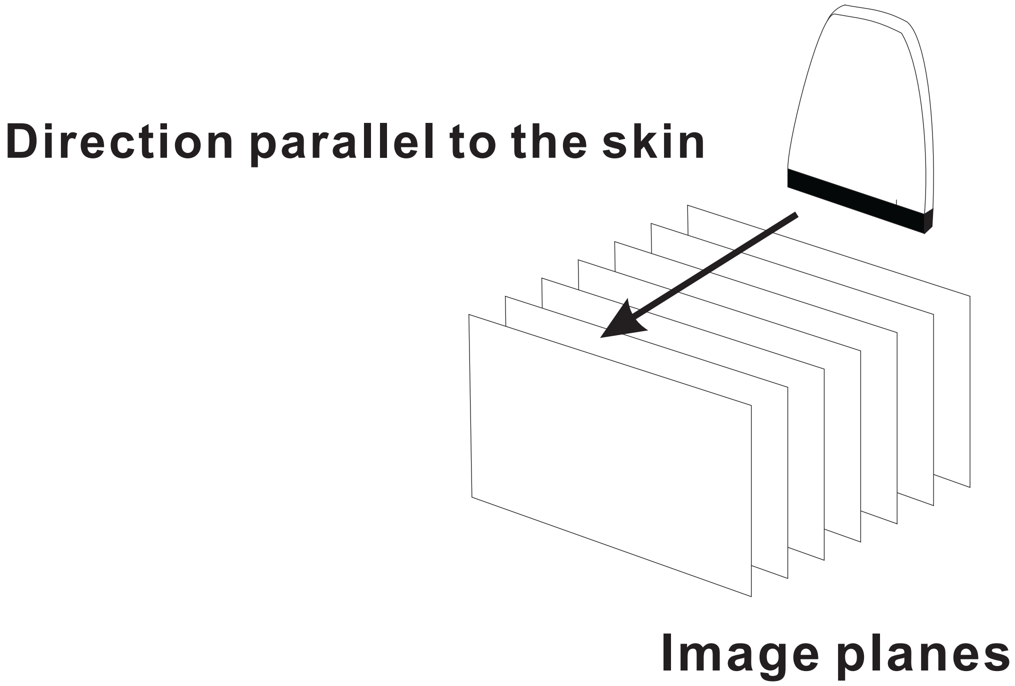

Figure 5.1: Moving the transducer parallel to the skin to generate cross sectional images in a volume.

sampled fat thickness is smaller than 30mm. Since the frequency of ultrasound affects the penetration ability, the efficiency of the thresholding algorithm with growing fat thickness is uncertain. More investigations can be conducted to assess the range of fat thickness that can be measured using our algorithm.

Ultrasound machines assume that the speed of sound in soft tissues ($1540ms^{-1}$) is constant; however, the speed of sound is variable in different tissues and fat tissue has a relatively low speed of sound ($\sim 1480ms^{-1}$)[52, 53]. The variation in speed casts doubt on the accuracy of spatial thickness measurements and the boundary can be displaced by around 4%(i.e.(1540-1480)/1540). The absolute thickness error increases when the fat thickness increases.

Other drawbacks of the system are the slow RF data capture rate. The current frame rate for capturing RF data is about 2Hz but we need 44 RF frames (11 steering angles with 4 focuses each) for the spectrum calculations; therefore, the total data capture time excluding processing of RF data is about 22 seconds. To reduce capturing time, fewer steering angles with larger angle step sizes can be used. The potential problem can be the lower probability of receiving echoes and the limitation of the depth coverage when the angle step size is too large.

Our current evaluation method relies on the manual segmentation of B-mode ultrasound image and its correlation with skinfold measurements. We do not have a gold standard that has a better accuracy to evaluate the true value of fat thickness and the effect of the speed displacement described in the previous paragraph. It may be worthwhile to consider using other imaging techniques, such as CT and MRI, as additional tools for further comparison. It may be possible that CT and MRI could provide a better gold standard. Further investigation with a gold standard will help to validate and improve the segmentation algorithm.

Bibliography

[1] J. Matiegka. The testing of physical efficiency. *American Journal of Physical Anthropology*, 4:223–230, 1921.

[2] Maria E. Ramirez. Measurement of subcutaneous adipose tissue using ultrasound images. *American Journal of Clinical Nutrition*, 89:347–357, 1992.

[3] R.J. Kuczmarski, M.T. Fanelli, and G.G. Koch. Ultrasonic assessment of body composition in obese adults: overcoming the limitations of the skinfold caliper. *American Journal of Clinical Nutrition*, 45:717–724, 1987.

[4] C. Nordander, J. Willner, G.A. Hansson, B. Larsson, J. Unge, L.Granquist, and S. Skerfving. Influence of the subcutaneous fat layer, as measured by ultrasound, skinfold calipers and bmi, on the emg amplitude. *European Journal of Applied Physiology*, 89:514–519, 2003.

[5] F. Perin, J.C Pittet, S. Schneert, P. Perrier, F. Tranquart, and P. Beau. Ultrasonic assessment of variations in thickness of subcutaneous fat during the normal menstrual cycle. *European Journal of Ultrasound*, 11:7–14, 2000.

[6] DW Newcom, TJ Baas, and JF Lampe. Prediction of intramuscular fat percentage in live swine using real-time ultrasound. *Journal of Animal Science*, 80(12):3046–3052, 2002.

[7] T. Abe, F. Tanaka, Y. Kawakami, K. Yoshikawa, and T. Fukunaga. Total and segmental subcutaneous adipose tissue volume measured by ultrasound. *Medicine and Science in Sports and Excercise*, 28:908–912, July 1996.

[8] Saito K, Nakaji S, Umeda T, Shimoyama T, Sugawara K, and Yamamoto Y. Development of predictive equations for body density of sumo wrestlers using b-mode ultrasound for the determination of subcutaneous fat thickness. *British Journal of Sports Medicine*, 37:144–148, 2003.

[9] Kenneth J. Ellis. Human body composition: In vivo methods. *Physiological Reviews*, 80(2):649–680, 2000.

[10] Scott B. Going. Densitometry. In T.G. Lohman A.F. Roche, S.T. Heymsfield, editor, *Human Body Composition*. Human Kinetics, Champaign, IL, 1st edition, 1996.

[11] M.A. McCrory, T.D. Gomex, and E.M. Bernauer. Evaluation of a new air displacement plethysmograph for measuring human body composition. *Medicine and Science in Sports and Exercise*, 27:1686–1691, 1995.

[12] L.Z. Coppini, D.L. Waitzberg, and A.C.L. Campos. Limitations and validation of bioelectrical impedance analysis in morbidly obese patients. *Current opinion in Clinical Nutrition and Metabolic care*, 8(3):329–332, 2005.

[13] A.F. Roche. Anthropometry and ultrasound. In A.F. Roche, S.T. Heymsfield, and T.G. Lohman, editors, *Human Body Composition*. Human Kinetics, Champaign, IL, 1st edition, 1996.

[14] AS Jackson and ML Pollock. Generalized equations for predicting body denisty of men. *British Journal of Nutrition*, 3:497–504, 1978.

[15] AS Jackson and ML Pollock. Generalized equations for predicting body denisty of women. *Medicine and Science in Sports and Excercise*, 12(3):175–182, 1980.

[16] MS Yuhasz. *Physical fitness and sports appraisal laboratory manual*. University of Western Ontario:London, 1974.

[17] C.Orphanidou, L.McCargar, C.L. Birmingham, J.Mathieson, and E.Goldner. Accuracy of subcutaneous fat measurement: Comparison of skinfold calipers, ultrasound, and computed tomography. *Journal of the American Dietetic Association*, 94(8):855–858, April 1994.

[18] Timothy G. Lohman. Dual energy x-ray absorptiometry. In T.G. Lohman A.F. Roche, S.T. Heymsfield, editor, *Human Body Composition*. Human Kinetics, Champaign, IL, 1st edition, 1996.

[19] P. Tothill, A.Avenell, and D.M. Reid. Precision and accuracy of measurements of whole-body bone mineral: comparisons between hologic, lunar and norland dual-energy x-ray absorptiometers. *The British Journal of Radiology*, 67(804):120–1217, 1994.

[20] J.P. Despres, R.Ross, and S.Lemieux. Imaging techniques applied to the measurement of human body composition. In T.G. Lohman A.F. Roche, S.T. Heymsfield, editor, *Human Body Composition*. Human Kinetics, Champaign, IL, 1st edition, 1996.

[21] J.C. Seidell, A. Oostelee, MAO. Thijssen, and et al. Assessment of intraabdominal and subcutaneous adbominal fat: relation between anthropometry and computed tomography. *American Journal of Clinical Nutrition*, 45:7–13, 1987.

[22] K. Tokunage, Y. Matsuzawa, K. Ishikawa, and S. Tarui. A novel technique for the determination of body fat by computed tomography. *International Journal of Obesity*, 7:437–445, 1983.

[23] H Kvist. Adipose tissue volume determinations in women by computed tomography: technical considerations. *International Journal of Obesity*, 10:53–67, 1986.

[24] J Kobayashi, N Tadokoro N, Watanbe M, and Shinomiya M. A novel method of measuring intra-abdominal fat volume using helical computed tomography. *International Journal of Obesity*, 26:398–492, 2002.

[25] G. Tornaghi, R. Raiteri, C. Pozzato, A. Rispoli, M. Bramani, M. Cipolate, and A. Craveri. Anthropometric or ultrasonic measurements in assessment of visceral fat? a comparative study. *International Journal of Obesity*, 18:771–775, 1994.

[26] G.C. Dooms, H. Hricak, and G. De Geer A.R. Margulis. MR imaging of fat. *Radiology*, 158:51–54, 1986.

[27] M.A. Foster, J.M.S. Hutchison, J.R. Mallar, and M. Fuller. Nuclear magnetic resonance pulse sequence and discrimination of high-and low-fat tissues. *Magnetic Resonance Imaging*, 2:187–192, 1984.

[28] P.A. Hayes, P.J. Sowood, A. Belyavin, J.B. Cohen, and F.W. Smith. Subcutaneous fat thickness measured by magnetic resonance imaging, ultrasound and calipers. *Medicine and Science in Sports and Excercise*, 20:303–309, 1988.

[29] Robert Ross. Magnetic resonance imaging provides new insights into the characterization of adipose and lean tissue distribution. *Canadian Journal of Physiology and Pharmacology*, 74(6):778–785, June 1996.

[30] V Positano, A Gastaidelli, AM Sironi, MF Santarelli, M Lombardi, and L Landini. An accurate and robust method for unsupervised assessment of abdominal fat by MRI. *Journal of Magnetic Resonance Imaging*, 20(4):684–689, 2004.

[31] RAD Booth, BA Goddard, and A Paton. Measurement of fat thickness in man - a comparison of ultrasound harpenden calipers and electrial conductivity. *British Journal of Nutrition*, 4(20):719–1966, 1966.

[32] P.A. Volz and S.M. Ostrove. Evaluation of a portable ultrasonoscope in assessing the body composition of college-age women. *Medicine and Science in Sports and Excercise*, 16:97–102, 1984.

[33] A. Bellisari, A.F. Roche, and R.M. Siervogel. Reliability of b-mode ultrasonic measurements of subcutaneous and intra-abdominal adipose tissue. *International Journal of Obesity*, 17:475–480, 1993.

[34] A. Flygare, L. Valentin, P. Karlsland Akeson, C.E. Flodmark, S.A. Ivarsson, and I. Axelsson. Ultrasound measurements of subcutaneous adipose tissue in infants are reproducible. *Journal of Pediatric Gastroenterology and Nutrition*, 28:492–494, 1999.

[35] B.A. Bullen, F. Quaade, E. Olesen, and S.A Lund. Ultrasonic reflection used for measuring subcutaneous fat in humans. *Human Biology*, 37:374–384, 1965.

[36] M.T. Fanelli and R.J. Kuczmarski. Accuracy of subcutaneous fat measurement: Comparison of skinfold calipers, ultrasound, and computed tomography. *American Journal of Clinical Nutrition*, 39(5):703–709, 1984.

[37] C. Stevens-Simon, P. Thureen, J.Barrett, and E.Stamm. Skinfold caliper and ultrasound assessments of change in the distribution of subcutaneous fat during adolescent pregnancy. *International Journal of Obesity*, 25:1340–1345, 2001.

[38] S. Kolesnik J. Wang, JC Thornton and PN. Pierson. Anthropometry in body composition - an overview. *In vivo body composition studies annals of the New York Academy of Sciences*, 904:317–326, 2000.

[39] Physical status: The use and interpretation of anthropometry. Technical Report 854, Geneva, 1995.

[40] Canadian population health initiative identifies obesity as research priority. Technical Report 3, Ocober/November 2002.

[41] Position of the american dietetic association and the canadian dietetic association: Nutrition for physical fitness and athletic performance for adults. *Journal of the American Dietetic Association*, 93(6):691–696, June 1993.

[42] Sinning WE. Body composition in athletes. In A.F. Roche, S.T. Heymsfield, and T.G. Lohman, editors, *Human Body Composition.* Human Kinetics, Champaign, IL, 1st edition, 1996.

[43] KA. Beals KA and MM. Manore MM. Nutritional status of female athletes with subclinical eating disorders. *Journal of the American Dietetic Association*, 98:419–425, 1998.

[44] A. DeLorenzo, P. Deurenberg, M. Pietrantuono, N. Di Daniele, V. Cervelli, and A. Andreoli. How fat is obese? *ACTA Diabetologica, Suppl. 1*, 40:S254–S257, October 2003.

[45] T. Abe, M. Kondo, Y. Kawakami, and T. Fukunaga. Prediction equations for body composition of japanese adults by b-mode ultrasound. *American Journal of Human Biology*, 6:161–170, 1994.

[46] C.A. Glasbey, I. Abdalla, and G. Simm. Towards automatic interpretation of sheep ultrasound scans. *Animal Science*, 62:309–315, 1996.

[47] Frederick W. Kremkau. *Diagnostic Ultrasound: Principles and Instruments.* W.B. Saunders Company, Philadephia, PA, 6th edition, 2002.

[48] Stephen.W. Flax, Norbert J. Pelc, Gary H. Glover, Frank D. Gutmann, and Maurice McLchlan. Spectral characterization and attenuation measurements in ultrasound. *Ultrasonic Imaging*, 5:95–116, 1983.

[49] D. Nicholas, C.R. Hill, and D.K. Nassiri. Evaluation of backscattering coefficients for excised human tissues: results, interpretation and associated measurements. *UMB*, 7:17–28, 1982.

[50] Johan M. Thijssen. Ultrasonic speckle formation, analysis and preciessing applied to tissue characterization. *Pattern Recognition Letters*, 24:659–675, 2003.

[51] Douglas A. Christensen. *Ultrasonic bioinstrumentation.* John Wiley & Sons, New York, 1st edition, 1988.

[52] S.A. Goss, R.L. Johnston, and F.Dunn. Comprehensive compliation of empirical ultrasonic properties of mammalian tissues. *Journal of the Acoustical Society of America*, 64(2):423–457, 1978.

[53] S.A. Goss, R.L. Johnston, and F.Dunn. Comprehensive compliation of empirical ultrasonic properties of mammalian tissues part 2. *Journal of the Acoustical Society of America*, 68(1):93–108, 1980.

[54] G. Treece, R. Prager, and A. Gee. Ultrasound attenuation measurement in the presence of scatterer variation for reduction of shadowing and enhancement. *IEEE Transactions on Ultrasonics, Ferroelectrics and Frequency Control*, 52:2346–2360, 2005.

[55] Frederic L. Lizzi, Ernest J. Feleppa, S. Kaisar Alam, and Cheri X. Deng. Ultrasonic spectrum analysis for tissue evaluation. *Pattern Recognition Letters*, 24:637–658, 2003.

[56] M. Fink, F. Hotteir, and J.F. Cardosa. Ultrasonic signal processing for in vivo attenuation measurement: Short Time Fourier Analysis. *Ultrasonic Imaging*, 5:117–135, 1983.

[57] Y.S. Akgul, C Kambhamettu, and M Stone. Automatic extraction and tracking of the tongue contours. *IEEE Transactions on Medical Imaging*, 18(10):1035–1045, 1999.

[58] SK Setarehdan and JJ Soraghan. Automatic cardiac LV boundary detection and tracking using hybrid fuzzy temporal and fuzzy multiscale edge detection. *IEEE Transactions on Biomedical Engineering*, 46(11):1364–1378, 1999.

[59] Anant Madabhushi and Dimitris N. Metaxax. Combining low-, high-level and empirical domain knowledge for automated segmentation of ultrasonic breast lesions. *IEEE Transactions on Medical Imaging*, 22(2):155–169, February 2003.

[60] A. Hammoude. Edge detection in ultrasound images based on differential tissue attenuation rates. *Ultrasonic Imaging*, 21(1):31–42, 1999.

[61] D Boukerroui, O Basset O, A Baskurt, and Gimenez G. A multiparametric and multiresolution segmentation algorithm of 3-d ultrasonic data. *IEEE Transactions on Ultrasonics, Ferroelectrics and Frequency Control*, 1(48):64–77, 2001.

[62] Igor Dydenko, Denis Friboulet, Jean-Marie Gorce, Jan D'hooge, Bart Bijnens, and Isabelle E. Magnin. Towards ultrasound cardiac image segmentation based on the radiofequency signal. *Medical Image Analysis*, 7:353–367, 2003.

[63] F. Dvignon, F.-F. Deprez, and O. Basset. A parametric imaging apporach for the segmentation of ultrasound data. *Ultrasonics*, 43:789–801, 2005.

[64] William Bloom and Don W. Fawcett. *A textbook of histology.* Chapman & Hall, New Yok, 12th edition, 1994.

[65] Michael H. Ross, Gordon I. Kaye, and Wojciech Pawlina. *Histology: a text and atlas.* Lippincott Williams & Wilkins, Philadelphia, Pa, 4th edition, 2003.

[66] L.M. Hinkelman, T.D. Mast, L.A. Metlay, and R.C. Waag. The effect of abdominal wall morphology on ultrasonic pulse distortion. part i. measurements. *Journal of the Acoustical Society of America*, 104(6):3635–3649, December 1998.

[67] James F. Greenleaf and Robert C. Bahin. Clinical imaging with transmissive ultrasonic computerized tomography. *IEEE Transactions on Biomedical Engineering*, 28(2):177–185, 1981.

[68] L.Landini and R. Sarnelli. Evaluation of attenuation coefficients in normal and pathological breast tissue. *Medical* & *Biological Engienering* & *Computing*, 24(3):243–247, 1986.

[69] Uwe Haberkorn, Günter Layer, Volker Rudat, Ivan Zuna, Adolf Lorenz, and Gerhard van Kaick. Ultrasound image properties influenced by abdominal wall thickness and composition. *Journal of Clinical Ultrasound*, 21:423–429, 1993.

[70] A. Pomaroli, B. Norer, R. Schellenast, and G. Klima. The sonographic pattern of fatty tissue in the floor of the mouth. *Quaderni Di Anatomica Pratica 1*, suppl XLIII:49–57, 1998.

[71] S. Bridal, P. Fornes, P. Bruneval, and G. Berger. Parametric (intergrated backscatter and attenuation) images constructed using backscattered radio frequency signal (25-56MHz) from human aortae in vitro. *Ultrasound Medicine and Biology*, 19:215–229, 1997.

[72] Gosta H. Granlund and Hans Knutsson. *Signal Processing for Computer Vision.* Kluwer Academic Pulbilishers, Netherlands, 1st edition, 1995.

[73] Nina Eriksoon Bylund, Marcus Ressner, and Hans Knutsson. 3D wiener filtering to reduce reverberations in ultrasound image sequences. In *Image analysis, Proceedings lecture notes in computer science*, volume 2749, pages 579–586, 2003.

[74] Nina Eriksoon Bylund, M. Andersson, and Hans Knutsson. Wide range frequency estimation in ultrasound images. In *Proceedings of SSAB Symposium on Image Analysis*, march 2001.

[75] M. Berson, A. Roncin, and L. Pourcelot. Compound scanning with an electrically steered beam. *Ultrasonic Imaging*, 3:303–308, 1981.

[76] S. Jespersen, J. Wilhjelm, and H. Sillesen. Multi-angle compound imaging. *Ultrasonic Imaging*, 20:81–102, 1998.

[77] S. Jespersen J. Wilhjelm and H. Sillesen. In vitro spatial compound scanning for improved visulization of atherosclerosis. *Ultrasonic Imaging*, 26(1357–1362), 2000.

[78] M. Tanter, J. Bercoff, L. Sandrin, and M. Fink. Ultrafast compound imaging for 2-D motion vector estimation: application to transient elastography. *IEEE Transactions on Ultrasonics, Ferroelectrics and Frequency Control*, 49:1363–1374, 2002.

[79] M. Pernot, M. Tanter, J. Bercoff, K.R. Waters, and M. Fink. Temperature estimaton using ultrasonic spatial compound imaging. *IEEE Transactions on Ultrasonics, Ferroelectrics and Frequency Control*, 51:606–615, 2004.

[80] Haifeng Tu, Tomy Varghese, Ernest L. Madsen, Quan Chen, and James A. Zagzebski. Ultrasound attenuation imaging using compound acquisition and processing. *Ultrasonic Imaging*, 25:245–261, 2003.

[81] N Otsu. Threshold selection method from gray-level histograms. *IEEE Transactions on Systems man and cybernetics*, 9(1):62–66, 1979.

[82] Paul L. Rosin. Unimodal thresholding. *Pattern Recognition*, 34:2083–2096, 2001.

[83] Paul L. Rosin and J. Hervas. Remote sensing image thresholding methods for determining landslide activity. *International Journal of Remote Sensing*, 26(6):1075–1092, 2005.

[84] Martin A. Fischler and Robert C. Bolles. Random sample consensus: A paradigm for model fitting with applications to image analysis and automated cartography. *Communications of the ACM*, 24(6):381–395, 1981.

[85] David A. Forsyth and Jean Ponce. *Computer Vision A Modern Approach*. Pearson Education, Upper Saddle River, New Jersey, 1st edition, 2003.

[86] Canadian Society for Exercise Physiology (CSEP). *Canadian Physical Activity, Fitness and Lifestyle Approach: CSEP-Health and Fitness Program's Health-Related Appraisal and Counselling Strategy*. Canadian Society for Exercise Physiology, 3rd edition, 2003.

[87] J. Martin Bland and Douglas G. Altman. Statistical methods for assessing agreement between two methods of clinical measurement. *The LANCET*, 8:307–310, February 1986.

Appendix A

Calculation of the Spectrum Central Frequency and Variance

Fink et al. [56] proved that the the spectrum moments of the short time Fourier transform are correlated to the attenuation rate, the spectrum central frequency and variance.

For a linear attenuation with frequency and neglecting diffraction effects, Fink et al. [56] showed that the relationship between the central frequency $f_c(t)$ and the spectrum variance $\sigma_s^2(t)$ that vary with time t is

$$\frac{df_c}{dt} = -\beta c \sigma_s^2(t) \tag{A.1}$$

where $\frac{df_c}{dt}$ is the attenuation rate, β is the attenuation coefficient and c is the speed of sound.

The spectrum due to attenuation is:

$$\epsilon(f,t) = \epsilon_o(t) e^{-(\alpha(f)ct)}. \tag{A.2}$$

And if the attenuation is linear with respect to frequency, then Equation A.2 becomes

$$\epsilon(f,t) = \epsilon_o(t) e^{-(\beta|f|ct)}. \tag{A.3}$$

The n^{th} moment of the spectrum $\epsilon(f,t)$ is

$$m_n(t) = \int_{f_2}^{f_1} \epsilon_o(t) e^{-(\beta|f|ct)} f^n df. \tag{A.4}$$

The differentiation of Equation A.4 becomes

$$\frac{dm_n(t)}{dt} = -\beta c m_{n+1}(t). \tag{A.5}$$

f_c of the spectrum is the spectrum centroid; therefore,

$$f_c = \frac{m_1(t)}{m_0(t)}. \tag{A.6}$$

$\frac{df_c}{dt}$ can be obtained by differentiating the Equation A.6 by the quotient rule and Equation A.4:

$$\frac{df_c}{dt} = \frac{d}{dt}\frac{m_1(t)}{m_0(t)} \tag{A.7}$$

$$= -\beta c\left(\frac{1}{m_0(t)}\left(\frac{dm_1(t)}{dt}\right) - \frac{m_1(t)}{m_0^2(t)}\left(\frac{dm_0(t)}{dt}\right)\right) \tag{A.8}$$

$$= -\beta c\left(\frac{m_2(t)}{m_0(t)}\right) - \left(\frac{m_1(t)}{m_0(t)}\right)^2) \tag{A.9}$$

$$= -\beta c\left(\frac{m_2(t)}{m_0(t)}\right) - f_c^2) \tag{A.10}$$

$$= -\beta c \sigma_s^2(t). \tag{A.11}$$

Therefore, the spectrum variance σ_s^2 is $\frac{m_2(t)}{m_0(t)} - f_c^2$.

Appendix B

Normalization of a Spectrum Property Image

A parametric image M_{ij} is normalized between 0 to 1 before carrying out the thresholding step. M_{ij} is normalized as follows:

$$\hat{M_{ij}} = g * \frac{(M_{ij} - min(M_{ij}))}{(max(M_{ij}) - min(M_{ij})} \tag{B.1}$$

where $\hat{M_{ij}}$ is the normalized M_{ij}

g is the maximum value of the normalized parametric image and its value is 1 for normalizing the parametric image between 0 to 1,

i is the column index,

j is the row index,

max is the function to find the maximum value in M_{ij}, and

min is the function to find the minimum value in M_{ij}.

Appendix C

Solution to Rosin's Thresholding Method

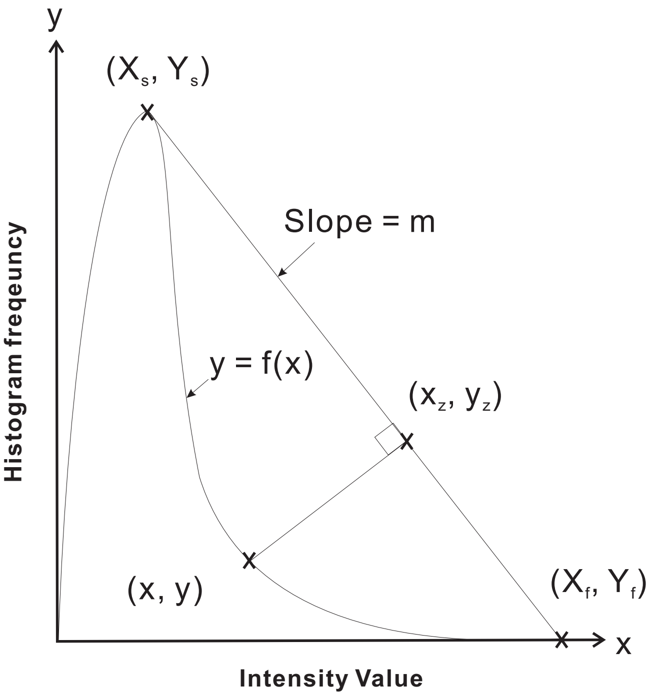

Figure C.1: Finding the threshold by Rosin's thresholding method.

Let the histogram be a function $y = \mathrm{f}(x)$ and the threshold located at the point (x,y) which has the maximum perpendicular distance from the straight line in the histogram.

Let (X_s, Y_s) be the histogram main peak, (X_f, Y_f) the first empty bin of the histogram following the last filled bin, m the slope of the straight line joining the (X_s, Y_s) and (X_f, Y_f) and $(x_z, y_z)$is a point on the straight line that achieves the maximum perpendicular distance to the straight line. To find (x_p, y_p), the first step is to find equations representing x_z and y_z.

The slope of the straight line is

$$m = \frac{(Y_s - Y_f)}{(X_s - Y_f)}. \tag{C.1}$$

Assume (x,y) is a point on the histogram, its perpendicular distance to the straight line can be calculated by the dot product as follows:

$$\begin{bmatrix} x - x_z \\ y - y_z \end{bmatrix} \cdot \begin{bmatrix} X_s - x_z \\ Y_s - y_z \end{bmatrix} = 0. \tag{C.2}$$

Rearranging the terms in Equation C.2, we have

$$ax_z^2 + bx_z + c = 0 \tag{C.3}$$

where

$$a = 1 + m^2$$

$$b = -(X_s + x) - m(y - Y_s) - 2m^2 X_s$$

$$c = xX_s + m(X_sY_s + X_sy - 2X_sY_s) + m^2 X_s^2.$$

x_z is solved from the roots of the quadratic Equation C.3 for each point (x,y) that lies between main peak (X_s, Y_s) and the last bin (X_f, Y_f).

Then, y_z can be found as

$$y_z = m(x_z - X_s) + Y_s. \tag{C.4}$$

The perpendicular distance from the straight line to (x,y) is then

$$distance = (\sqrt{(x - x_z)^2 + (y - y_z)^2}). \tag{C.5}$$

The threshold point is the point (x,y) that has the maximum distance in Equation C.5.

Appendix D

UBC Research Ethics Board Certificate of Approval

The University of British Columbia
Office of Research Services and Administration
Behavioural Research Ethics Board

Certificate of Approval

PRINCIPAL INVESTIGATOR Rohling, R.N.	DEPARTMENT Electrical and Computer Eng	NUMBER **B05-0820**
INSTITUTION(S) WHERE RESEARCH WILL BE CARRIED OUT UBC Campus ,		
CO-INVESTIGATORS: Lawrence, Peter, Electrical and Computer Eng; Ng, Jessie, Electrical and Computer Eng		
SPONSORING AGENCIES		
TITLE : Measuring Subcutaneous Fat in Ultrasound Images		
APPROVAL DATE OCT 13 2005	TERM (YEARS) 1	DOCUMENTS INCLUDED IN THIS APPROVAL: Sept. 8, 2005, Advertisement / Consent form

CERTIFICATION:

The protocol describing the above-named project has been reviewed by the Committee and the experimental procedures were found to be acceptable on ethical grounds for research involving human subjects.

Approval of the Behavioural Research Ethics Board by one of the following:
Dr. Peter Suedfeld, Chair,
Dr. Susan Rowley, Associate Chair

This Certificate of Approval is valid for the above term provided there is no change in the experimental procedures